ESTIMATION OF VECTOR SURFACE CURRENTS BEYOND THE REGION OF OVERLAP OF DUAL-SITE HF RADAR: AN IMPLEMENTATION OF THE CONTINUITY EQUATION

PRADEEP BOBBY

Your file Votre référence
ISBN: 0-612-89612-9
Our file Notre référence
ISBN: 0-612-89612-9

Estimation of Vector Surface Currents beyond the Region of Overlap of Dual-Site HF Radar: An Implementation of the Continuity Equation

by

©Pradeep Bobby, B.Eng.

A thesis submitted to the School of Graduate Studies

in partial fulfillment of the requirements for the

degree of Master of Engineering.

Faculty of Engineering and Applied Science

Memorial University of Newfoundland

May 2003

St. John's Newfoundland Canada

Abstract

Knowledge of ocean surface currents is important for commercial and research reasons. High-frequency (HF) radar is a useful tool for measuring oceanographic phenomena because the frequencies involved can propagate for long distances across salt water, the radar wavelength is of similar magnitude to ocean wavelengths of significant energy, and a large expanse of water can be interrogated.

Oceanographic information can be found from the Doppler plot of the electromagnetic energy reflecting from the ocean surface. The ocean, like any target, will have a radar cross section and it will depend on electromagnetic and hydrodynamic factors. Although the mechanism of interaction between radar and ocean waves is complex, it can be modelled and it has been found that there are many different portions of the cross section that depend on the order and location of the scatter or scatters. Several examples of simulated cross sections are presented at a variety of wind speeds; dominant wave directions and radar frequencies. The radar senses the component of the current projected along the radar look direction and the manifestation of this is a displacement of the first order spectral energy.

When two or more radars illuminate the same area of ocean it is possible to construct a two-dimensional vector current. The geometrical method used to find the vector current will affect the accuracy of the values. The Cartesian method involves locating the range cell in Cartesian coordinates with respect to the centre of the baseline joining the radars. The Cylindrical method uses one of the radar sites as the coordinate system origin; the radial current is found automatically and the tangential component is proportional to the radial term of the other radar. HF radar systems are located at Cape Race and Bonavista and a series of simulations based on

their geometry indicate that the Cartesian method is preferrable for the calculation of vector currents.

Due to the limited dimensions of the dual-site coverage, it is desirable to find a way to increase the effective size of the overlap. An approach incorporating the continuity equation uses knowledge of vector currents within the overlap and radial currents outside of it to estimate tangential currents where only single-site data exists. Simulations indicate that the method should work for uniform currents and variable currents. The current magnitude and direction affect the utility of the technique.

The continuity technique is used within the overlap with real radar data so that dual-site currents, calculated with the Cartesian method, can be used to verify the extrapolations. Regardless of whether the Cape Race or Cape Bonavista facilities is used as the reference for the calculations, the continuity technique yielded good approximations of vector current magnitude and direction for the first extension cell.

Acknowledgements

The author wishes to thank the Faculty of Engineering and Applied Science for providing the opportunity and the facilities necessary to complete this project. Special gratitude is expressed for the supervision of Dr. Eric Gill for his ongoing support, encouragement, and availability. Dr. Gill's leadership involved an appropriate mixture of allowing independent effort and supplying needed insights.

Northern Radar Inc. is acknowledged for making the author aware of the issue of extrapolation of vector surface currents beyond dual-site coverage and thus, motivating the work contained herein. The company also supplied the experimental radar data presented in Chapter 4 of this thesis. President Barry Dawe frequently answered questions regarding radar operation and employee Ken Hickey was often consulted on programming matters and on standard processes for dealing with surface currents.

The assistance from C-CORE was invaluable. Employee Desmond Power was consulted regarding the groundtruthing of radar data and was instrumental in permitting access to radial current information from the Cape Race and Cape Bonavista sites. Drifter data was furnished as well as a description of the company's procedure for comparison of radar and drifter data.

Examiners Dr. John Walsh and Desmond Power are esteemed for critically evaluating the thesis and providing valuable suggestions. Their commemts are responsible for improving this thesis from its original form.

This effort was funded by (1) the Career Development fund managed by the provincial Department of Career Development and Advanced Studies, (2) a grant from the National Science and Engineering Research Council (NSERC) to the author, (3) a grant from the Maritime Awards Society of Canada, and (4) payment from the Faculty of Engineering and Applied Science for teaching and teaching assistanceships.

Contents

List of Figures

List of Tables

List of Symbols

The page numbers indicate the first significant reference to the symbol. Variations of the parameters, for example initial values, are not indicated as well and sometimes common symbols may have an alternate interpretation for a brief period.

λ_0 : Wavelength of radar energy (pg. 7).

λ : Wavelength of ocean wave (pg. 7).

K : Wavenumber of ocean scattering wave (pg. 7).

k_0 : Wavenumber of radar energy (pg. 7).

$\vec{K}_1$: Wavevector for first scattering event (pg. 9).

$\vec{K}_2$: Wavevector for second scattering event (pg. 9).

$\vec{k}_0$: Wavevector for radar energy (pg. 9).

v_r : Surface current radial velocity (pg. 11).

Δf : Surface current induced shift in frequency of the Bragg peaks (pg. 11).

Δv_r : Error in the surface current measurement (pg. 11).

$\Delta \rho_s$: Radial length of a radar range cell (pg. 11).

τ_0 : "On" length of the transmit pulse for a pulsed radar (pg. 11).

$\Delta \phi$: Nominal radar beamwidth (pg. 11).

σ : Total radar cross section of the ocean surface (pg. 21).

σ_1 : First order radar cross section of the ocean surface (pg. 21).

ω_D : Radian Doppler frequency (pg. 21).

$S_1(\cdot)$: Directional ocean wave spectral model (pg. 21).

m : Indicator for Doppler frequency region for first order cross section (pg. 21).

ω_B : Radian resonant Bragg frequency (pg. 22).

Sa[$\cdot$] : Sampling function (pg. 22).

$\delta(\cdot)$: Dirac delta function (pg. 23).

σ_2 : Second order radar cross section of the ocean surface (pg. 23).

m_1, m_2 : Indicators for Doppler frequency region for second order cross section (pg. 23).

$\theta_{\vec{K}_1}$: Angle for scattering wavevector $\vec{K}_1$ (pg. 24).

Γ_s : Symmetricized coupling coefficient (pg. 24).

U : Wind speed (pg. 26).

$\overline{\theta}$: Dominant direction of the ocean waves (pg. 26).

$P_c(\omega_D)$: Average power spectral density of the clutter signal returned from the ocean to the receive array (pg. 27).

d_c : Duty cycle of the radar (pg. 27).

k : Boltzman's constant (pg. 28).

T_0 Reference temperature taken as 290 K (pg. 28).

F_{am} Median noise figure (pg. 28).

$P_N(\omega_D)$: Power spectral density for the noise signal (pg. 29).

$\epsilon\cdot$: Random phase term (pg. 29).

V_x, V_y : Surface current velocity in Cartesian coordinates (pg. 42).

r_1, r_2 : Distances from radars 1 and 2, respectively, to the remote patch (pg. 42).

x, y : Cartesian distance from the centre of the radar baseline to the remote patch (pg. 42).

V_1, V_2 : Radial currents measured with respect to radar 1 and 2 respectively (pg. 42).

θ_1, θ_2 : Angle measure from the radar baseline to the remote patch for radar 1 and 2, respectively (pg. 43).

V_r, V_t : Radial and tangential components, respectively, of the surface current (pg. 43).

γ : Angle between the look direction of the secondary radar and the direction of the tangential current determined with respect to the reference radar (pg. 43).

ΔF_s : Frequency resolution due to a N-point FFT (pg. 45).

ρ_w : Water density (pg. 54).

$\vec{v}$: Water velocity (pg. 54).

v_ρ, v_ϕ v_z : Radial, tangential, and vertical velocity components of the surface current (pg. 54).

ϕ_0 : Angle measured from the radar baseline at which vector currents are known for at least one range cell (pg. 55).

f : Coriolis parameter (pg. 57).

Ω : Angular rate of rotation of the earth in radian/s (pg. 57).

φ : Location in degrees latitude (pg. 57).

$\left(\frac{\partial \tau^y}{\partial x} - \frac{\partial \tau^x}{\partial y}\right)$: Wind stress curl (pg. 58).

Δz : Depth of the surface Ekman layer (pg. 58).

ν : Kinematic viscosity (pg. 58).

Δv_{vert} : Simulated error in the tangential current due to ignoring the vertical velocity gradient when using the continuity technique (pg. 63).

Δv_{RMS} : RMS error in current magnitude (pg. 76).

$\Delta \phi_{RMS}$: RMS error in current direction (pg. 76).

Chapter 1

Introduction

1.1 Importance of Surface Currents

Despite the fact that the coupling between water parcels and suspended or floating material is not well established [1], the motion of water at the surface will indeed have an effect on the transport of matter at the top of the water column. Depending on the type of material being shifted, a different depth dependent surface current will be important. Listed below are several practical applications of such information [1], [2], [3].

- Surface currents are the most important parameter in the design of offshore drilling structures.
- Search and rescue teams can more easily track and find drifting vessels.
- Coastal pollution from sewage plants can be traced.
- The movement of harmful algae blooms can be monitored.
- Future locations of oil and other surface borne pollutants after a spill can be determined.

- Knowledge of fish larvae transport, which affects the health of fish stocks, is improved.
- Beach erosion and renourishment can be predicted.
- Air-sea interaction studies are enhanced.
- Mooring of floating structures can be better planned.
- Prediction of transport of water masses of abnormal temperature, which gives information on weather patterns for entire continents, is enabled.

It may be noted in passing that there are four factors that contribute to surface currents: tides, geostrophy, winds, and waves [4]. Although the tidal component often comprises 50% of the total current, wind and wave generated water flow can also be significant [1].

1.2 Conventional Surface Current Measurement

Currents can be measured via Eulerian and Lagrangian methods. With an Eulerian approach a point measurement of the current is obtained. Several models of moored current meters are employed in this manner. Lagrangian currents are found by tracking the position of a drifting particle and noting the time taken between measurements. The examination of dye packages, drogued and undrogued drifters and suspended sediment [3] qualify as Lagrangian techniques.

Unfortunately, there are many problems when using conventional approaches. Current meters must be moored at depths greater than 10 meters. This is done to prevent interference with ships, damage by ice, and surfacing in the troughs of large waves [1]. As well, currents vary with depth and surface values will be different from those obtained at moored locations. The closer current meters are placed to the

surface the more they are exposed to high frequency velocity vacillations resulting from waves and mooring motion.

Determining the locations of floating particles is time consuming; typically only one vector current value is reaped per drifter for every half-hour of measurement. There is also a considerable cost associated with data collection since aircraft, ships or satellites must record the progress of the buoyant devices. The final results are not even truly Lagrangian since the coupling between the current and drifters is unknown [5]. With GPS tracking of drifters, positional accuracy can be within 10 m. Based on the location accuracy of the drifters, the resulting current values will be similarly credible.

1.3 Utility of HF Radar for Surface Current Measurements

It has been long known that there exists an interaction between electromagnetic waves and the ocean surface. When first discovered, the result was dubbed clutter since it interfered with the radar detection of targets such as aircraft and ships. However, subsequent research showed that the returned radar signal contained information about the ocean surface. Surface currents are one of the ocean characteristics that can be ascertained via radar.

1.3.1 Advantages of Using HF Radar to measure Surface Currents

Despite the high initial installation cost, the use of HF radar for measuring currents has many advantages over conventional methods. Some of them are listed below [6].

- Frequencies in the HF band are not affected by precipitation or wind so the

radar can operate in any weather condition.

- Data can be acquired in real time.
- Current maps with a high resolution (within a few cm/s) covering large spatial extents (greater than 10000 km^2) can be produced.
- Current patterns can be determined in almost real time which enables quick reaction to oil spills and search and rescue operations.
- There is a minimum of overhead; monitoring is done from shore without any need for aircraft, ships or satellites.
- If operation is continuous, then the currents can be correlated with short term driving forces such as winds, waves and tides and these forces can be measured. These forces will affect ice and iceberg motion so the relationship between currents and their effects can be better understood.
- Icebergs, bergy bits and growlers may achieve appreciable velocities due to surface currents and may be hazardous to moored and semi-fixed structures. Appropriate measures can be taken if ice and strong currents are in the same area.
- Gathering of long term time series, which is useful in prediction of extreme currents, is facilitated.

1.3.2 Dual Radar System

It will be expained in Section 1.4 that a single radar facility is capable of sensing waves travelling directly towards or away from itself. Similarly, a single site is only capable of detecting the radial current or the component of current along the radar look direction. Figure 1.1 shows how this can be misleading. Depending on the

direction in which the radar beam is pointing, the same ocean current can have a negative, positive or zero radial component.

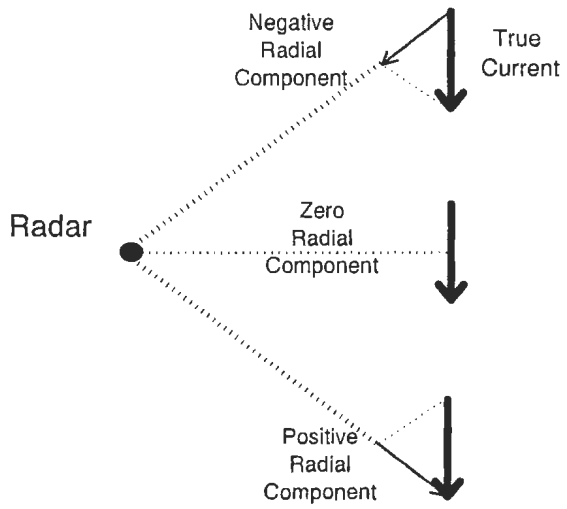

Figure 1.1: Single radar only detects radial velocity component.

When there are two spatially separated radars that share a common coverage area, vector currents can be calculated in the region of overlap through geometric manipulations. This topic will be discussed more thoroughly in Section 3.1.

Unfortunately, the overlap region will have a limited size (see Figure 3.3) and the computation of the vector currents will be subject to various instabilities. Further constraints are imposed by the limited range and azimuth of a radar, and the distant placement of facilities to maximize single-site coverage. Hence there is considerable interest in developing algorithms that would increase the effective size of the overlap to enable the accurate calculation of vector currents over larger areas.

1.3.3 Single Radar System

Single-site monostatic facilities are able to avoid many of the problems and limitations associated with dual-site systems. The drawback, however, is that there is no direct

method of determining vector velocity values.

Various techniques have been employed to determine vector current velocities with a monostatic radar. One method involves making the assumption that the spatial variability of the currents is lower than the resolution provided by the radar. Thus, it is possible to combine several range cells that are adjacent in range and/or azimuth and state that the current is uniform there as illustrated in Figure 1.2. Since each new range cell will be composed of several smaller range cells there will be multiple radial velocity measurements. The total current can be determined via a least-squares analysis [6], [7]. Obtaining full current information from a single site is very limited due to the assumptions and simplifications necessary.

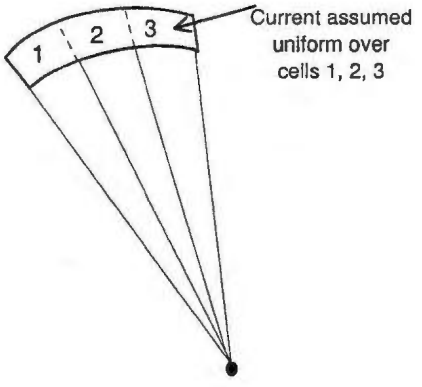

Figure 1.2: Calculation of vector currents using a single radar.

By expressing the radial and tangential components of the current as a Fourier series over angle and employing the hydrodynamic continuity equation, Lipa and Barrick [7] were able to determine vector currents using a short range, broad-beam system.

1.4 Application of HF Radar to Current Measurement

There are a number of issues regarding the use of radar for measuring surface currents that have not yet been addressed. Some, dealt with below, relate to the nature of the interaction between electromagnetic energy and the ocean surface, the process by which a single radar facility can measure radial currents, and the parameters pertinent to the physical constraints of the radar measurements.

1.4.1 Mechanism of Interaction

Radio oceanography as a valid field of study began in 1955 when Crombie [8] analyzed the backscatter of 13.56 MHz radio waves from the ocean surface. It was noticed that, regardless of the wind and sea state, the bandwidth of the spectra was quite small and had most of the energy concentrated about a specific frequency. From this he deduced that the sea behaves like a diffraction grating and the Bragg mechanism is responsible for the scatter [8]. The Bragg condition states that primary resonant scattering will occur when $\lambda_0 = 2\,\lambda \sin\theta$ [9] where λ_0 is the radio wavelength, λ is the ocean wavelength and θ is the incident angle as measured from the surface normal. Due to the large distance of the ocean patch from the radar, grazing incidence can be assumed and the relation simplifies to $\lambda_0 = 2\lambda$. In terms of wavenumber the Bragg relationship can be written as

$$K = 2k_0 \tag{1.1}$$

for first order backscatter where K is the wavenumber of the ocean scattering wave and k_0 is the radar wavenumber.

Surface waves can be classified as capillary or gravity waves. The dominant restor-

ing force for short-wavelength capillary waves is surface tension and for gravity waves, gravity. Both surface tension and gravity will affect affect capillary waves, but the surface tension will have the stronger effect. For longer wavelength waves, the opposite is true. Gravity waves have wavelengths above 7 cm [10]. HF radar will only sense waves of the order of meters; only the longer gravity waves will be visible to the radar. The hydrodynamic dispersion relationship for gravity waves in deep water relates the spatial and temporal wavenumbers and can be expressed as

$$\omega = \sqrt{gk}. \tag{1.2}$$

where g is the acceleration due to gravity. Ocean waves of wavenumber k and frequency ω will travel with phase velocity (see, for example, [11])

$$v = \omega/k = \sqrt{g/k} \tag{1.3}$$

Waves of all wavelengths travelling in all directions will be present on the ocean for an arbitrary wind condition [12]. However, waveheights will vary depending on the wind direction up to a maximum height, h, of $h \approx 0.14\lambda$. Further input energy results in wave breaking. Equations (1.2) and (1.3) show that the velocity of a water wave is a function of its wavelength. The HF radar is a Doppler device; targets of different speeds will be modulated to different frequencies in the returned signal. Since the radar strongly senses those waves traveling directly towards or away from it, a radar of a particular frequency will produce very strong peaks in predictable locations in the resulting Doppler spectrum.

The conjecture that first order Bragg scatter is responsible for the most significant features of the ocean clutter was verified quantitatively by modelling backscatter of radio waves from a gently rippled surface [13]. Barrick and Peake [14] arrived at the same result by examining scatter from a slightly rough surface.

Higher order scatter also contributes to the Doppler spectrum, but the effects are not as strong. Second order scatter may occur from a single reflection from second order waves or from two scatters from first order waves [15]. A first order wave is generated by wind forcing. When two first order waves interact non-linearly, a second order wave is produced. The relationship that must be satisfied for backscatter is

$$\vec{K_1} + \vec{K_2} = -2\vec{k_0} \tag{1.4}$$

where $\vec{k_0}$ is the radar wavevector and $\vec{K_1}$ and $\vec{K_2}$ are the wavevectors for the two scattering events [16]. Figure 1.3 shows the geometry of the second order backscatter condition. As second and higher order phenomena will not affect surface current measurement, further discussion will be omitted.

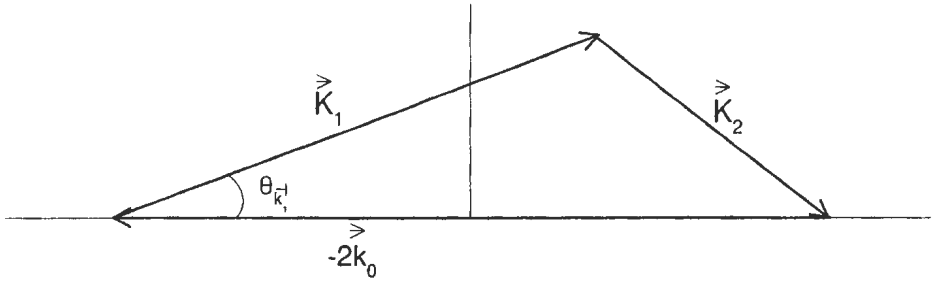

Figure 1.3: Geometry of second order scatter.

It should be noted at this time that waves on the ocean surface are not perfectly sinusoidal. Rather, they are characterized by long, shallow troughs with sharp, pointed peaks, i.e. they are trochoidal in nature. A wave can be decomposed into its Fourier series. Thus, an ocean wave with the same wavenumber as the radar will have a first harmonic with a wavenumber twice that of the radar. This satisfies the Bragg condition and results in resonant returns at frequencies other than at the Bragg frequencies. Thus, the scattering relationships provided in (1.1) and (1.4) apply to the spectral components of the ocean wave and not the wave as a whole. Such effects will be explored more fully when we discuss the cross section of the ocean surface in

1.4.2 Current Determination

Crombie [17] noticed during his experiments in the Gulf Stream that the resonant Bragg peaks in the returned Doppler spectrum were not in the positions predicted by the hydrodynamic dispersion relationship. Rather, the peaks were subject to a small frequency shift. He correctly surmised that the frequency shift was indicative of motion of the entire water surface. Historical current data in the area supported his hypothesis and several investigators since have validated the use of HF radar as a surface current sensor [3], [4], [18], [19], [20], [21]. Figure 1.4 below shows a typical simulated cross section of the ocean surface [22] subject to the spherical earth attenuation functions [23]. The first order peaks (F), the second order content (S) and the nulls separating the first and second order phenomena (N) have been indicated. The factors that affect the shape of the plot are discussed in Chapter 2.

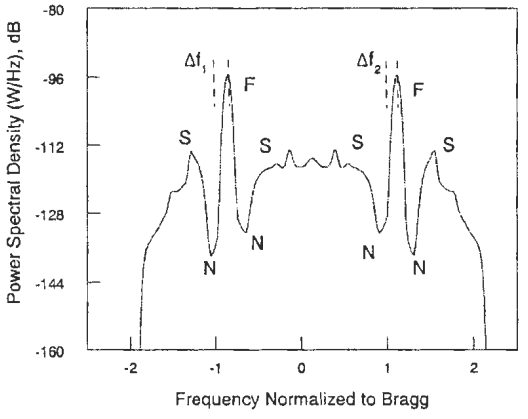

Figure 1.4: Simulated cross section of the ocean surface when the radar frequency is 10 MHz, windspeed is 10 m/s and directed perpendicular to the radar look direction.

Since the distance between the dominant peaks is constant for a given radar frequency and the locations of the peaks themselves are highly predictable, the extra shift, Δf, is easy to find. In Figure 1.4 there are two frequency shifts given. Theoret-

ically they should be the same, but noise may cause them to be slightly different. As well, in some cases the wind direction will completely obscure one side of the Doppler spectrum. There are two approaches to dealing with different values of Δf. It is valid to take the average of the frequency shifts but if one first order peak is much weaker than the other or is non-existent then the shift of the stronger peak will be used. The radial component, Δv_r, of the current velocity with respect to the radar look direction is easily shown to be

$$v_r = 0.5 \Delta f \lambda_0. \tag{1.5}$$

The radar is not a perfect measuring device and the radial current will be correct within a certain tolerance with the error, Δv_r, being dependent on the parameters used in the spectral analysis (see Section 3.2).

1.4.3 Physical Constraints

In addition to the radar's ability to measure surface currents [17], the radar is also useful for determining winds [24] and ocean wave directional spectra including estimates of significant wave height [25].

The precision and distance to which oceanographic information can be determined depends largely on the operation properties of the radar. Due to the high conductivity of sea water at HF frequencies (3-30 MHz), surface wave propagation is enhanced [12] and evaluation of the ocean surface can occur beyond the line of sight.

The pulsed radar sees the ocean surface as a set of annular sections known as range cells. The radial length of a range cell, or the range resolution $\Delta \rho_s$, is simply determined by the length of the transmit pulse τ_0 as $\Delta \rho_s = \frac{c\tau_0}{2}$ where c is the vacuum speed of light. The width of a range cell is determined by the distance ρ from the radar and the beamwidth $\Delta \phi$ of the radar. The overall spatial resolution of radar-

measured currents, winds and directional wave height spectra is the size of a range cell which is usually several square kilometers. Since the interaction for first order effects is resonant, a range cell must have an adequate length so that the radar wave can interact with a sufficient number of ocean wavelengths. Reducing the pulse length improves the range resolution, but reduces the likelihood of a resonant interaction taking place. The long wavelengths involved at HF make it difficult to produce a narrow beam. For a uniform, linear, phased array system operating in broadside the beamwidth is given as $\Delta\phi \approx \frac{2.65\lambda_0}{\pi M d}$ where $\Delta\phi$ is the radar beamwidth, M is the number of elements in the array and d is the spacing between the antennas [26].

Figure 1.5 illustrates some of the parameters that are important for locating a range cell. As the radar beam sweeps across the ocean surface the range resolution will remain fixed. However, due to beam steering issues, the beamwidth will be significantly higher at large scan angles as compared to broadside.

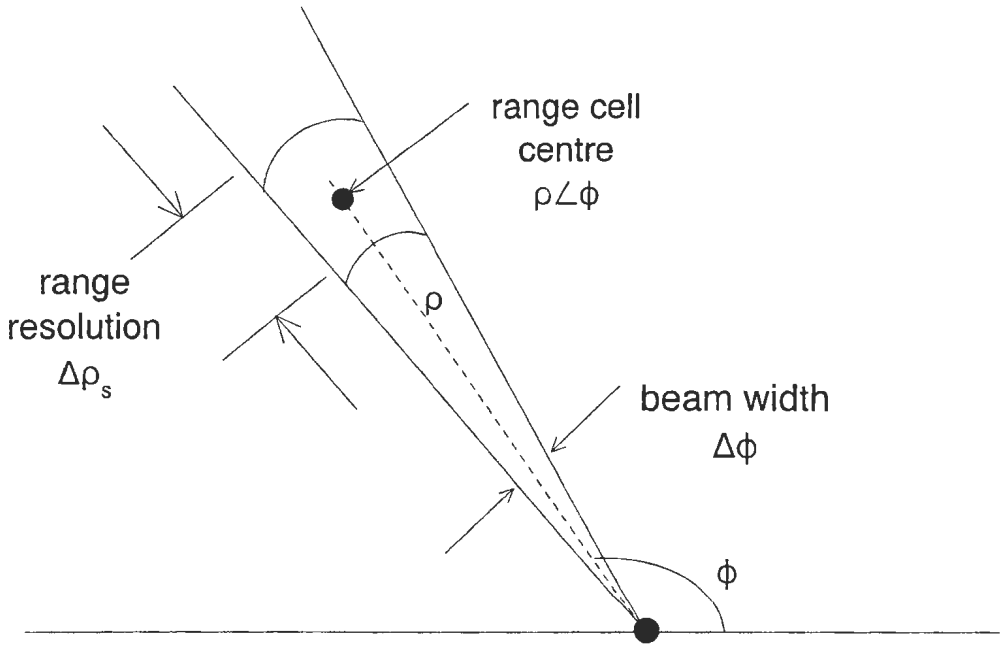

Figure 1.5: Range cell located at discrete range and azimuth.

1.5 Literature Review

Long before the field of radio-oceanography developed it was known that electromagnetic waves will react with the ocean surface. As noted, Crombie [8] was the first to correctly suggest the nature of the interaction to be that of Bragg scattering. The periodic radio wave undergoes resonant reflection from the periodic ocean surface when the radio wavelength is twice that of the ocean wavelength. Furthermore, to first order, the radar is only able to sense those waves traveling directly towards and away from the radar beam. This first order relationship results in two distinct peaks in the returned spectrum symmetrically displaced from zero Doppler. Wait [13] analytically verified Crombie's observation by examining the reflection of electromagnetic waves from a gently rippled surface. Barrick and Peake [14] confirmed the effect of the resonant phenomena by examining the scatter from slightly rough surfaces and noting the most significant scatter occurs when the radar wavenumber is half that of the wavenumber of the surface roughness.

Surrounding the first order peaks is a continuum of seemingly arbitrary return. Ward [27] suggested that the signal outside the Bragg peaks was due to higher order interactions. Hasselmann [16] proposed that the continuum contained the information necessary to construct the nondirectional waveheight spectrum. He also deduced the correct form for the second order Bragg conditions.

The boundary perturbation conditions proposed by Rice [28] involved using a perturbation approach to examine the problem of radio wave scattering from rough surfaces. The restrictions on his boundary perturbation approach are satisfied by the ocean surface. Based on Rice's theory, Barrick [29] derived a model for the first order cross section of the ocean surface that was consistent with Crombie's observations.

Motivation for developing the ocean cross section to second order arose from a need to explain the continuum surrounding the first order peaks. The Doppler spectrum

contains signal levels that are above the noise floor and includes minor, but non-negligible peaks. Barrick [15] found two sources of second order return to be due to second order scatter as based on Rice's boundary perturbation theory and second order hydrodynamic terms, and was able to produce a second order cross section of the ocean surface.

The first and second order models developed by Barrick make the assumptions of plane wave incidence and infinite surface conductivity. A more realistic model for the first order cross section was set forth by Gill and Walsh [30]. Their derivations were based on examining the fields of a dipole source scattering from a finite patch that had good, but finite, conductivity. The first order cross section as proposed by Barrick [29] portrays the scatter as a delta function and specifies that only waves of a single wavenumber are visible to the radar. However, the radar beam must have a finite beamwidth and the scattering patch must have a finite length which results in a smeared, or widened delta function. Examination of cross sections from real data confirms that the sampling function form derived by Gill and Walsh better describes the nature of the interaction.

The theory developed until the early 1970s explained the locations of the dominant peaks in the spectrum as well as higher order return. However, it was noticed that at times the two Bragg peaks were not exactly symmetrically displaced from zero Doppler as noted in Section 1.3. To explain the extra frequency shift, which could not be justified via wave motion, Crombie proposed [17] that the motion of the entire water surface was responsible. Comparison of the extra shift with historical records of surface currents showed good agreement. Hence, a current has the effect of shifting the whole Doppler spectrum. Just as the first order interaction of radar waves with the ocean surface results in the radar sensing only those waves moving directly parallel or antiparallel to the radar beam, only radial surface currents can be measured. When

there are two radars that irradiate the same patch of ocean, geometric relations can be used to construct a full vector current. Numerous experiments have since verified the utility of HF radar for surface current determination [3], [4], [18], [19], [20], [31], [32].

Early HF radars were designed as narrow-beam systems for the purposes of military target detection. One of the advantages of such systems is that electronic scanning facilitates the retrieval of directional information and the high resolution surface features can be mapped. One of the disadvantages with narrow-beam radar is the length of the antenna needed to produce such a narrow beam [33]. In the mid-1970s a small, short range, broad-beam radar named CODAR (Coastal Ocean Dynamics Applications Radar) was developed. CODAR used a simple azimuthally isotropic monopole for transmitting and a crossed loops pair and a monopole for receive [34]. Due to the low cost, small size, and ease of operation, CODAR has been utilized in numerous experiments and has resulted in many significant contributions to the field of radio-oceanography.

Using the CODAR system, Stewart and Joy [21] extended the understanding of radio measured surface currents. By assuming a specific form of the depth dependence of the current field it was derived that the radar essentially averages surface currents over a depth of $\lambda_0/8\pi$. An experiment using multiple radar frequencies to probe the same region of ocean yielded different values for the surface current which supported the theoretical prediction and allows for the calculation of current shear.

Analysis of the spectral characteristics of the ocean surface has revealed that waves of all wavelengths traveling in all directions will be present [12]. However, it is obvious that, over time, waves parallel with the wind will have greater amplitude than those that are anti-parallel. By comparing the ratios of the Bragg peaks researchers Long and Trizna [24] estimated surface winds during an experiment conducted in

Chesapeake Bay, Maryland.

Various methods have also been proposed to extract vector surface current information from single-site data. Lipa and Barrick [7] introduced the technique of model fitting to estimate vector curents from single-site radial values alone. When using a single radar site, several consecutive range cells were combined, thus allowing for multiple radial estimates while assuming that the current is uniform over the larger area. Least squares analysis was used to determine the total current. Since fewer data points were available at higher ranges due to decreased power, the number of range cells joined together was increased with range and resulted in lower errors for the estimates. The release of dye samples verified the general direction of the current, but no precise ground truthing was conducted.

Hickey [6] approached the model fitting problem slightly differently. A sector consisting of several range cells is chosen and the current was assumed to be uniform within. Each radial estimate is a projection of the total current with an error component included. By examining all the cells from a given sector and stating that the error term has zero mean and constant variance the problem can be solved using standard regression techniques.

Frisch and Leise [35] proposed that the hydrodynamic continuity equation could be solved to determine the tangential component of the current provided that vector currents are known at some radar scan angle and radial currents are known in the region that estimates will take place. The edge of this overlapping area can be considered as the angle at which vector currents are known and single-site information will surround this region allowing the criteria for using continuity to be satisfied. If vector current information is known at an additional radar scan angle, comparisons can be made between the true values and those obtained from extrapolation. Alternately, if the angular separation between the two sets of known vector currents is great, the

extrapolation process can be conducted from both sides of the overlap. Since the radar only measures horizontal currents, the vertical velocity gradient in the continuity equation is ignored. The use of the continuity equation in this fashion is a hybrid approach to the solution of vector currents. Its performance can be expected to fall short of that of two-site data, but be better than single-site estimations.

Lipa and Barrick [7] used the continuity equation and were able to eliminate the requirement of knowing vector currents at an arbitrary angle by expressing the radial and tangential velocity components each as a Fourier series over angle and solving for the coefficients. The zeroth order coefficient is an integration constant and follows from the boundary condition that the normal velocity must be zero at the shore. This constraint forces the normal velocity to be zero all along the shoreline surrounding the radar. In addition, the technique proposed by Lipa and Barrick degraded strongly as ranges exceeded 20 km and required that integrations be carried out over the full 360° surrounding the radar. When integrations were conducted over the half plane over the ocean alone, results were even less accurate. The papers by Frisch and Leise, and Lipa and Barrick were based on short range CODAR systems and exact ground truthing was not conducted to validate the theory.

1.6 Scope of Research

The motivation for the work undertaken by this thesis was a need to measure vector surface currents off the coast of Newfoundland. Currently, there are radar systems in operation at Cape Race and at Cape Bonavista. At each site is a narrow-beam, long-range radar that functions in the HF range. The area over which they operate, the Grand Banks, has long been known as an abundant fishing ground and has more recently been developed for its oil reserves.

The two radars have some area of common coverage. One of the purposes of this

thesis is to present and evaluate different methods of measuring vector surface currents using two-site data. It is also desired to extend the knowledge of vector currents beyond the overlap. The key questions to be resolved are: "what is the best method for calculating the vector current from two-site data?" and "how far and with what degree of accuracy can estimates of vector currents be made outside the overlap?" Simulations based on the actual dual-site geometry will be used to consider the first question; the equation of continuity will be applied in addressing the second. To the author's best knowledge, the work in this thesis is the first time that different vector current construction techniques have been compared, that the continuity equation has been applied to a long range, narrow-beam system, and that real radar data has been available to verify the utility of the continuity technique. As well, the error introduced by ignoring the vertical velocity gradient has been approximated for the first time and included as an error term for the tangential current estimates during simulations.

Chapter 1 serves as an introduction to the theory that explains the use of HF radar as a remote sensor for the ocean and establishes the importance of the knowledge provided by the radar. Chapter 2 discusses the models used for the first and second cross sections of the ocean surface. Simulations of the cross sections are shown for a variety of sea states, wind directions and radar frequencies. A noise model has been included to reproduce the effect of external noise on the cross sections and a brief outline on how to find the radial currents from the cross sections is provided. Chapter 3 begins with an explanation of two of the possible ways to convert two radial current estimates from different sites into a vector current. Simulations based on the geometry of the Cape Race and Cape Bonavista systems are conducted using a variety of current directions and one of the two-site methods is chosen for application to real data. Next, the theory regarding the use of the continuity equation for the prediction

of vector currents is covered. A description of the error involved in the analysis is provided for the first time. Simulations testing the continuity approach using uniform and variable currents are conducted. In Chapter 4 the continuity equation is solved within the overlap region and tested against the two-site data there. Chapter 5 quantitatively comments on the usefulness of the continuity equation for current estimates from a long range, narrow-beam system and suggests some areas for future development.

Chapter 2

Review of Ocean Radar Cross Sections

Derivation of the cross sections of the ocean surface requires a development of the electric field equations applied to scattering from the ocean surface. There are many ways to address the scattering problem; however, the approach that accounts for polarization dependence and very large wavelength radiation is the boundary perturbation method. This procedure requires that the following limitations be satisfied: waveheight must be small in terms of the radio wavelength, the surface slopes must be small compared to unity, and the impedence of the sea water must be small in relation to the impedence of free space [28]. The process of derivation of the cross sections is quite tedious. Using various approximation techniques, researchers have found different expressions for the cross sections to first order [29], [30] and second order [15], [30]. For the ensuing discussion the first and second order models developed by Gill and Walsh [30] will be used. The cross sections proposed by Barrick assume plane wave incidence and infinite surface patch size. The first order cross section is represented by a delta function which suggests infinite energy spectral density at the Bragg frequency and that the radar is only interacting with a very specific wave

train with a very precise wavenumber. In reality, it is known that the Bragg waves will have a finite spectral width and finite energy. The models developed by Gill and Walsh assuming a dipole source result in sampling functions for the first order peaks. This is more comparable to real radar returns as is confirmed by numerous experiments ([32], [36], [37]) and is more rigorous since the simplifications of infinite patch size, infinite conductivity and plane wave incidence are not made. The total cross section, σ, will be the sum of the cross sections to whatever order is required. That is, $\sigma = \sigma_1 + \sigma_2 + \ldots$ where the subscripts indicate the order of scatter.

As with all radar-derived oceanographic information, the desired data is contained within the cross section of the ocean surface. Although the entire spectrum is shifted in the presence of a current [17], the net water motion can be measured by finding the displacement of the first order peaks. Here the cross section of the ocean surface is written to second order and examples of the cross sections in the presence of noise will be displayed. The essentials of the monostatic cross sections of this chapter are either found explicitly in or are based on the bistatic case in [22]. They are included here as background to the surface current algorithms which follow in Chapters 3 and 4. Finally, an algorithm to extract the radial currents from the cross section is presented.

2.1 First Order Cross Section

The first order monostatic cross section of the ocean surface [30] normalized to scattering patch area and having units of $(\text{rad/s})^{-1}$ is given by

$$\sigma_1(\omega_D) = 2^4 \pi k_0^2 \sum_{m=\pm 1} S_1(m\vec{K}) \frac{K^{-5/2}}{\sqrt{g}} \Delta\rho_s \, \text{Sa}^2 \left[\frac{\Delta\rho_s}{2} (K - 2k_0) \right] \tag{2.1}$$

where $S_1(m\vec{K})$ is a directional ocean wave spectral model, K is the wavenumber of the scattering wave, $\Delta\rho_s$ is the length of the surface patch, k_0 is the radar wavenumber and the value of m indicates the Doppler region; $m = \pm 1$ for negative and positive

Doppler frequencies, respectively. The term $\mathrm{Sa}(\cdot)$ is the sampling function defined as $\mathrm{Sa}(x) = \dfrac{\sin x}{x}$. The argument of the sampling function, $\dfrac{\Delta\rho_s}{2}(K - 2k_0)$, indicates that the peak will occur when $K = 2k_0$ as per the Bragg condition in (1.1). In terms of the Doppler frequency, resonance occurs when

$$\omega_D = \sqrt{2gk_0} = \omega_B \tag{2.2}$$

where ω_D is the general Doppler frequency and ω_B is the Bragg frequency as it appears in the Doppler spectrum. The radar frequency, ω_0, specifies the radar wavenumber through $k_0 = \omega_0/c$ where c is the speed of light in a vacuum. The radial extent of the scattering patch, $\Delta\rho_s$, is defined in Section 1.4.3.

2.2 Second Order Cross Section

There are at least three components to the second order HF Doppler cross section of the ocean surface [30]. Patch scatter occurs when both scattering wavevectors are from the same surface patch of ocean and can occur when there is a single scatter from a single second order ocean wave or a double scatter from two first order waves. Another contribution to the second order energy occurs when one scatter occurs near the transmitter and the second at some remote patch. A third piece of second order scatter occurs when the first scatter occurs on a remote patch and the second near the receiver. Since patch scatter is the most significant element of the second order cross section, it is the only part that will be considered here and will be referred to as the second order cross section. It is important in a preliminary way to discuss here the second order cross section since a necessary part of the current extraction algorithm involves the determination of spectral nulls between the first and second order regions of the Doppler spectra. The second order cross section of the ocean surface can be expressed as

$$\sigma_2(\omega_D) = 2^6\pi^2 k_0^4 \sum_{m_1=\pm 1} \sum_{m_2=\pm 1} \int_{-\pi}^{\pi} \int_0^{\infty} \Big\{ S_1(m_1\vec{K}_1) S_1(m_2\vec{K}_2) \cdot |_s\Gamma|^2 \delta\Big(\omega_D + m_1\sqrt{gK_1} + m_2\sqrt{gK_2}\Big) K_1 \Big\} dK_1 d\theta_{\vec{K}_1}. \tag{2.3}$$

1. Separation of Doppler Regions via m_1 and m_2

To ensure non-zero results in equation (2.3) the delta function must be satisfied as follows

$$\omega_D = -m_1\sqrt{gK_1} - m_2\sqrt{gK_2} \tag{2.4}$$

where m_1 and m_2 can each independently take on the values of ± 1. The four combinations of m_1 and m_2 will refer to different regions of the Doppler spectrum.

Case 1: $m_1 = m_2$

Using equations (2.2) and (2.4) it is found that $\omega_D < -\omega_B, m_1 = m_2 = 1$ and $\omega_D > \omega_B, m_1 = m_2 = -1$.

Case 2: $m_1 \neq m_2$

Once again using (2.2) and (2.4) the constraint on the Doppler frequency is $\omega_D^2 < 2gk_0$.

For $K_1 < K_2$, it is possible to write

$$\begin{aligned} 0 < \omega_D < \omega_B &\Rightarrow m_1 = 1, m_2 = -1 \\ -\omega_B < \omega_D < 0 &\Rightarrow m_1 = -1, m_2 = 1 \end{aligned} \tag{2.5}$$

2. K_1 and K_2

The K_1 and K_2 shown in (2.3) are the magnitudes of the two scattering vectors necessary for second order backscatter. Combining equations (1.1) and (1.2) we can write $\vec{K} = \vec{K}_1 + \vec{K}_2 = -2\vec{k}_0$.

Wavevector $\vec{K}_1$ can be written as $\vec{K}_1 = K_{1x}\hat{x} + K_{1y}\hat{y}$ such that $K_1 = \sqrt{K_{1x}^2 + K_{1y}^2}$ and $\theta_{\vec{K}_1} = \tan^{-1}\left(\frac{K_{1x}}{K_{1y}}\right)$. Re-examining the delta function constraint of (2.4) it can be noted that the contours for constant ω_D will be symmetric about the lines $K_{1x} = 0$ and $K_{1y} = 0$. Due to the symmetries in K_{1x} and K_{1y}, it is not necessary to solve the delta function constraint for all values of K_1. When the solution is found in the half plane $K_1 < K_2$ it is also found when $K_2 < K_1$ by interchanging the vector magnitudes [33].

Using the law of cosines and the geometry of Figure 1.3, the relationship between $\vec{K}_1$ and $\vec{K}_2$ can be found to be $K_2 = \sqrt{K_1^2 + 4k_0^2 - 4K_1 k_0 \cos(\theta_{\vec{K}_1})}$.

3. Solution of the Delta Function Constraint

Due to the presence of the delta function in (2.3) the double integral can be simplified to a single integral. Utilizing a technique used by Lipa and Barrick [33] we first define

$$Y = \sqrt{K_1}. \tag{2.6}$$

The delta function can be written as $\delta(\cdot) = \delta(w_d - D_P(Y, \theta_{\vec{K}_1}))$ where $D_P(Y, \theta_{\vec{K}_1}) = -(m_1\sqrt{gK_1} + m_2\sqrt{gK_2})$. Now it will be possible to solve the delta function constraint shown in (2.4). That is, for every value of ω_D and $\theta_{\vec{K}_1}$ the equation

$$G(Y) = w_d - D_P(Y, \theta_{\vec{K}_1}) \tag{2.7}$$

must be solved by finding a $Y = Y^*$ such that $G(Y^*) = 0$. Equation (2.7) can be solved numerically or analytically by transformation into a cubic equation.

4. Singularities in the Integrand

There are two sources of singularities in the second order cross section. The first arises in the Jacobian used in the transformation to convert the double integral to a single integral via the delta function constraint. The second is the coupling coefficient, ${}_s\Gamma$.

The singularities due to the Jacobian will occur at Doppler shifts of

$$\omega_D = \mp\sqrt{2}\omega_B \tag{2.8}$$

where the $-$ sign applies when m_1 and m_2 are both positive and corresponds to scatter from ocean waves that have the same wavelength as the radar. The $\sqrt{2}$ singularity from the Jacobian can also occur when there is a first order scatter from a second order wave.

The coupling coefficient is made up of a dominant hydrodynamic term and a smaller electromagnetic term. The hydrodynamic portion is smooth; the electromagnetic term contains the singularities and is symmetricized in order to allow integration over the half plane $K_1 < K_2$ alone as discussed earlier.

The singularities from the coupling shift occur at Doppler shifts of

$$\omega_D = \pm 2^{3/4}\omega_B \tag{2.9}$$

and is known as "corner reflector" scatter.

2.3 Ocean Spectral Model

Present in the formulations for the first and second order cross sections is the factor $S_1(\vec{K})$, which is the ocean spectrum . It is known that this waveheight directional spectrum is dependent on four parameters: wind velocity and direction, duration over which the wind is present, and fetch, or open distance across which the wind blows [11]. Several different ocean spectral models have been developed and are being used [38]. They all consist of a product of two terms: an omnidirectional spectrum, $S(K)$, and a normalized directional distribution, $G(\theta_{\vec{K}})$ and are expressed as

$$S(\vec{K}) = S(K, \theta_{\vec{K}}) = S(K)G(\theta_{\vec{K}})$$

with

$$\int_{-\pi}^{\pi} G(\theta_{\vec{K}}) d\theta_{\vec{K}} = 1. \tag{2.10}$$

The Pierson-Moskowitz (PM) spectrum, $S_{PM}(K)$, is a commonly used omnidirectional model [39]. The relationship between the PM spectrum, $S_{PM}(K)$, and the ocean spectrum being used here for the development of the cross sections, $S_1(K)$, is

$$S_1(K) = \frac{1}{2} S_{PM}(K). \tag{2.11}$$

The PM spectrum is not dependent on fetch or duration. This implies that it is not valid for all sea states. Rather, a sufficiently long fetch and duration have been assumed in order to yield values for a fully developed sea. A fully developed sea is characterized by no further wave growth or decay; input energy from the wind is balanced by energy loss due to wave breaking. At this state an increase in fetch or duration will, theoretically, have no impact on wave growth [11].

The total form of $S_1(K)$, including a commonly used directional spectrum, $G(\theta_{\vec{K}})$, found in [38] is

$$S_1(m_* \vec{K}) = \left[\frac{\alpha_{PM}}{4K^4} e^{\left(\frac{0.74 g^2}{K^2 U^4} \right)} \right] \cdot \left[\frac{4}{3\pi} \cos^4 \left(\frac{\theta_{\vec{K}} + \frac{(1-m_*)\pi}{2} - \overline{\theta}}{2} \right) \right] \tag{2.12}$$

where α_{PM} is a dimensionless constant valued at 0.0081, g is the gravitational constant, U is the mean wind speed measured at 19.5 m above the mean sea surface, and m_* represents the possible values of m, m_1, and m_2.

2.4 Addition of a Noise Model

The cross sections examined thus far are constructed as ideal cross sections; the values are the average of an infinite number of oceans examined for an infinite amount of time and there is no noise present to contaminate the results. In reality there is only one ocean to probe, the duration of the measurement may be long but finite, and at HF the radar will usually be externally noise limited.

Noise will play an important role in the calculation of currents. Figure 1.4 shows a different frequency shift for the approaching and receding Bragg lines. Equation (1.5) indicates that the frequency shifts should be the same and noise is responsible for the discrepancy.

The transformation from the ideal to the realistic cross sections requires that the radar range equation be applied to the cross section so the effect of the appropriate gains and attenuations that are present in a system can be included. The radar range equation (see, for example, [40]) is

$$P_c(\omega_D) = \frac{\lambda_0^2\left(\frac{\tau_0}{T_L}\right)P_t G_t G_r |F(\rho,\omega_0)|^4 A\sigma(\omega_D)}{(4\pi)^3\rho^4} \tag{2.13}$$

where $P_c(\omega_D)$ is the average power spectral density of the clutter signal returned from the ocean to the receive array, τ_0 is the "on" length of a transmit pulse, T_L is the total length of a transmit pulse, P_t is the transmitter power, G_t is the transmitter gain, G_r is the receiver gain, $F(\rho,\omega_0)$ is the spherical earth attentuation function as calculated by Dawe [23] when distance to the patch is ρ and the radar frequency is ω_0, and A is the effective cross sectional area of the receive array. The ratio τ_0/T_L is known as the duty cycle, d_c, of the radar and is included to express the radar range equation in terms of average, rather than peak, power spectral density.

Next, the power spectral density of the noise must be found. Since at HF fre-

quencies the radar will be usually externally noise limited, all internal noise will be ignored. External noise can be classified as being atmospheric, galactic, and man-made [40]. Atmospheric noise can be generated by lightning discharges and emissions from radioactive gases. Galactic noise arises from the sun, quasars, and other celestial radio sources and man-made noise stems from sources such as electric machinery [41]. The relative importance of each of these noise sources will vary with operating frequency, location, time of day, and time of year. Even though the overall value of the external noise will vary with the above parameters, consideration of an average value of the noise will be adequate for illustration purposes.

It is possible to determine the external noise factor using the noise power and bandwidth, and various constants; the noise figure is proportional to the logarithm of the noise factor. For the purposes of the simulations discussed in this chapter there is no antenna from which to measure the noise power. Hence, a median noise figure, F_{am}, will be used as provided from tables. Two sets of values are supplied by the ITU [41]. They are the noise figure exceeded 0.5 % and 99.5% of the time; the average of these numbers is what is taken as the median noise figure. While this method does not give the true median value, except for certain types of noise power distributions, it is sufficient.

Assuming that the noise is a stationary, white gaussian process the power spectral density, $S_N(\omega')$ [22], is

$$S_N(\omega') = \frac{kT_0}{2\pi} 10^{\frac{F_{am}}{10}} \tag{2.14}$$

where $k = 1.38 \times 10^{-23}$ J/K is Boltzman's constant, T_0 is the reference temperature which is taken as 290K and ω' is radian frequency. It may be noted that ω' is valid over the entire real axis but $S_N(\omega')$ will be non-zero only over the noise bandwidth of the receiving system.

In the case of greater than a few pulses, the external Doppler noise spectral density, $P_N(\omega_D)$ [22], is

$$P_N(\omega_D) = d_c S_N(\omega') \sum_{p=L(\frac{-1}{2d_c})}^{G(\frac{1}{2d_c})} \mathrm{Sa}[p\pi d_c]. \tag{2.15}$$

At this stage we have spectral forms individually for the clutter and the noise that are based on infinite ensemble averages. A more realistic representation would be based on a finite time series. The conversion of the ideal cross sections into realistic simulations can be accomplished by employing Pierson's model for a stationary Gaussian process in one variable [42]. Taking $f(t)$ to represent either the noise, $n(t)$, or clutter, $c(t)$, time signals and $F_s(\omega)$ as the spectral densities for the noise or clutter respectively we can write

$$f(t) = \int_B e^{j\omega t} e^{j\epsilon(\omega)} \sqrt{F_s(\omega) d\omega}. \tag{2.16}$$

The integral is calculated over the bandwidth of the Doppler spectrum, and $\epsilon(\omega)$ is a random phase term uniformly distributed in the interval $[0, 2\pi)$. The differential under the square root can be explained by expressing (2.16) as a summation. Now, if we let $\Delta\omega$ go to zero we have

$$f(t) = \lim_{\substack{\omega_{2P}\to\infty \\ (\omega_{2q+2}-\omega_{2q})\to 0}} \sum_{q=0}^{p} e^{j(\omega_{2q+1}t)} e^{j\epsilon(\omega_{2q+1})} \sqrt{F_s(\omega_{2q+1}) \cdot (\omega_{2q+2} - \omega_{2q})}. \tag{2.17}$$

Values of q are in the range $0 \leq q \leq (r-2)/2$ where r is the number of discrete frequency points chosen. The frequency net which examines alternate values of frequency is more than adequate. Figure 2.1 shows the noise spectra after conversion to a finite time series and then back to frequency via Fourier transformation. The spectrum is flat over the Doppler range of interest.

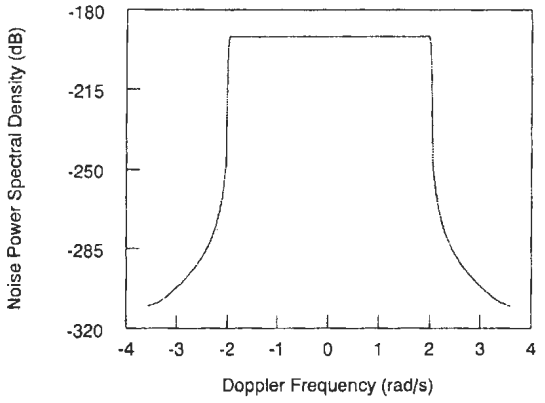

Figure 2.1: Noise signal.

After the finite time signals are found for the noise and clutter they are added together to produce the total time signal. Conversion back into the frequency domain is done by calculating the Fourier transform of the time series.

2.5 Examples of the Cross Sections

The cross section equations presented in (2.1) and (2.3) have been programmed using C++. The code has been included in Appendix A. The noise model as described in the previous section has also been added. The rest of this chapter will be devoted to displaying examples of the cross sections under different wind speed magnitudes and directions, and radar frequencies. The cross sections depicted vary in shape and magnitude; an effective current determining algorithm, outlined in Section 2.6, is needed to extract the currents from the Doppler spectrum over a broad range of cases.

For all plots the distance to the scattering patch is 100 km, duty cycle is 0.04, transmitted power is 16 kW, transmitter gain is 1.585, receiver gain is 65.76, range resolution is 1500 m, and the radar beamwidth is 4°. A Blackman window has been used to smooth the values from the Fourier analysis.

Effect of Wind Speed Magnitude

It has been noted by Barrick [43] that for frequencies above 6 MHz the first order cross section remains fairly constant with changing sea state since at those frequencies the Bragg waves will be fully developed already. However, it is predicted that higher order effects will vary more significantly with wind speed. Figure 2.2 shows four cases when wind speed varies between 5 and 20 m/s at a radar frequency of 10 MHz. As indicated by Barrick, the first order phenomena can be observed to be relatively invariant while the second order effects change in magnitude.

Ignoring the effect of the spherical earth attenuation function it can be seen that, while the first order cross section is not affected greatly by wind speed, the second order cross section is. Changes in the wind speed and direction cannot contribute any further energy to those waves. However, according to equation (1.4), a continuous range of ocean wavelengths contribute to second order scatter. Increasing the wind speed will tend to increase the energy of the lower wavelength gravity waves which results in higher second order scatter levels.

Effect of Wind Direction

In a strict sense the wind direction will be different from the wave direction. In the Northern Hemisphere, due to the Coriolis acceleration, fluid transport will be directed to the right of the direction of the forcing wind. For the purposes of this thesis, no distinction will be made between the wind and wave directions.

According to the Pierson-Moskowitz ocean spectral model adopted in Section 2.3 for the fully developed sea, there will be waves of all wavelengths travelling in in all directions. However, stronger first order returns can be expected when the radar look direction is aligned with, or directly opposed to, the dominant wave motion. Figure 2.3 shows the simulated cross section of the ocean for several wave directions measured relative to the radar look direction. Some special cases to note are at angles

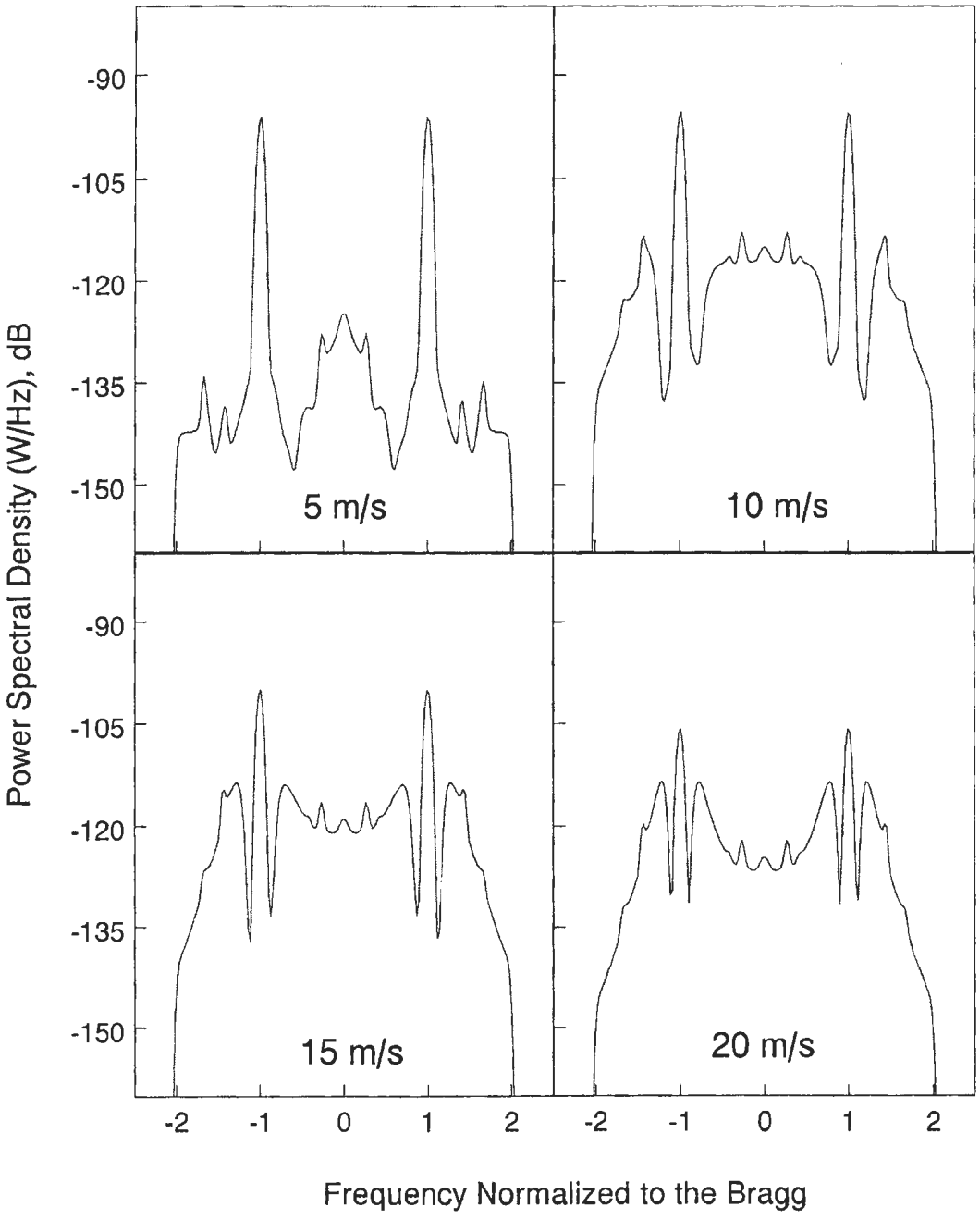

Figure 2.2: Simulated cross sections at various wind speeds at 10 MHz when the wind is perpendicular to the radar look direction.

of 90°, 0° and 180°. At 90°, the Bragg lines and surrounding second order scatter are symmetrical about zero Doppler. At 0° there is virtually no signal return from the approaching waves and at 180° there is no return from the receding waves.

It would be expected, then, that as the dominant wave direction becomes more aligned with the radar look, the received power of the related Bragg peak would increase. However, the spherical earth attenuation factor, $|F(\rho, \omega_0)|$ from equation (2.13), also plays a role. Consider Figure 2.4 where the dominant wave direction is directed 30° with respect to the radar look direction. As in Figure 2.2, though the first and second order spectra become more clearly defined with increasing wind speed, the overall power in the spectrum decreases. The decrease in power is caused by the attenuation term. When the wind direction is perpendicular to the radar look direction the value of $|F(\rho, \omega_0)|$ is approximately halved over the wind speed range of 5 to 20 m/s which causes a reduction in the power spectral density of 1/16. When the wind is directed at 30° to the radar look direction the value of $|F(\rho, \omega_0)|$ decreases by about a factor of 5 over the same wind speed range.

Figure 2.5 shows a plot of values of the attenuation at various wind speeds and angles [23]. It can be seen that as the wind speed increases and as the wind becomes more aligned with the radar look direction, the attenuation factor decreases in magnitude which accounts for the counter-intuitive decrease in cross section power under these conditions.

Effect of Radar Frequency

The radar frequency used plays a major role in the shape of the cross sections. Lower frequencies propagate more efficiently across the ocean surface and result in higher returns. Values of the attenuation function vary from about 0.79 at 3.2 MHz to 0.05 at 30 MHz. The Cape Race and Cape Bonavista sites were operated at frequencies of 3.2 MHz and 3.45 MHz, respectively, during testing in the summer and

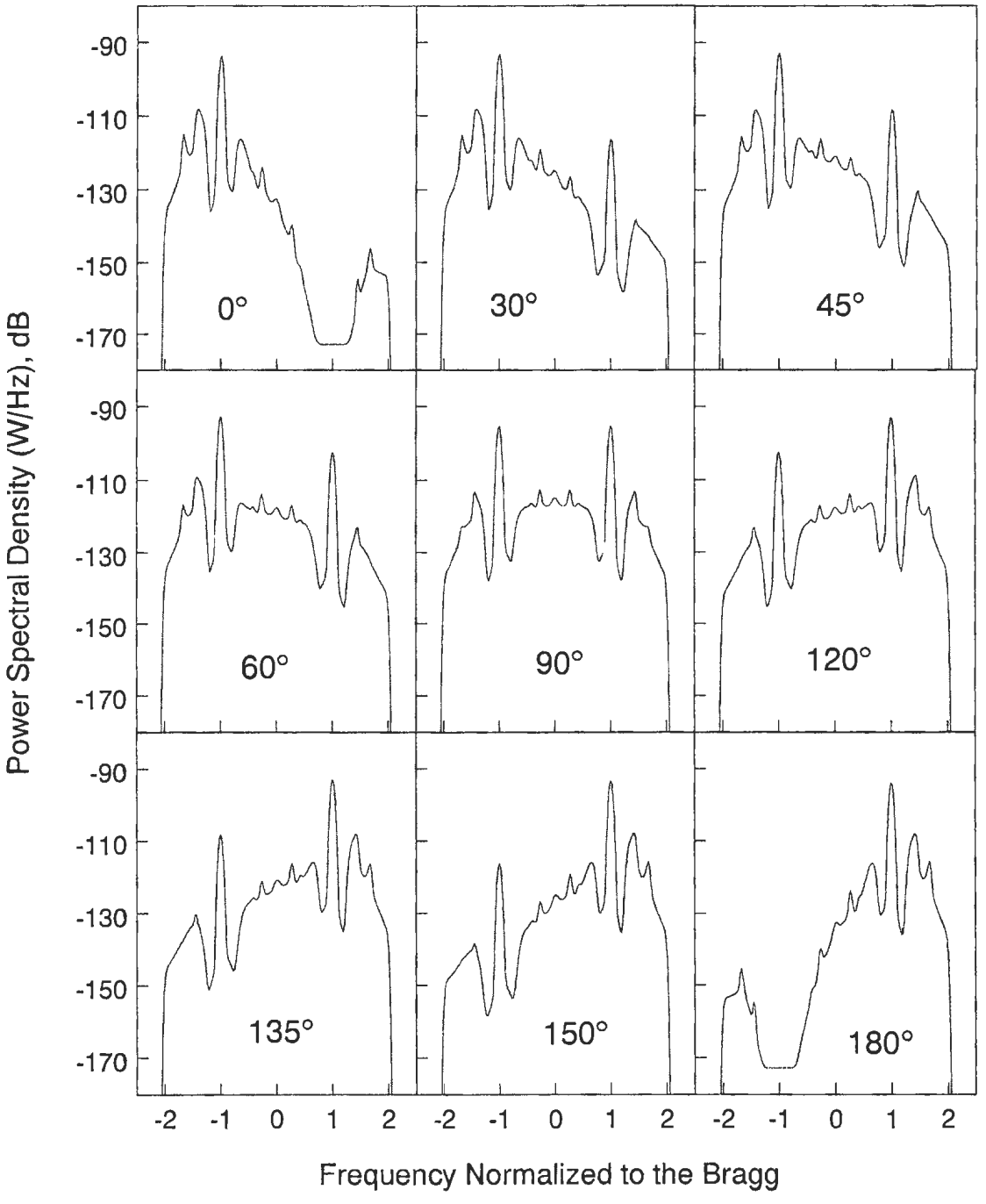

Figure 2.3: Simulated cross sections at various wave directions at 10 MHz with a wind speed of 10 m/s.

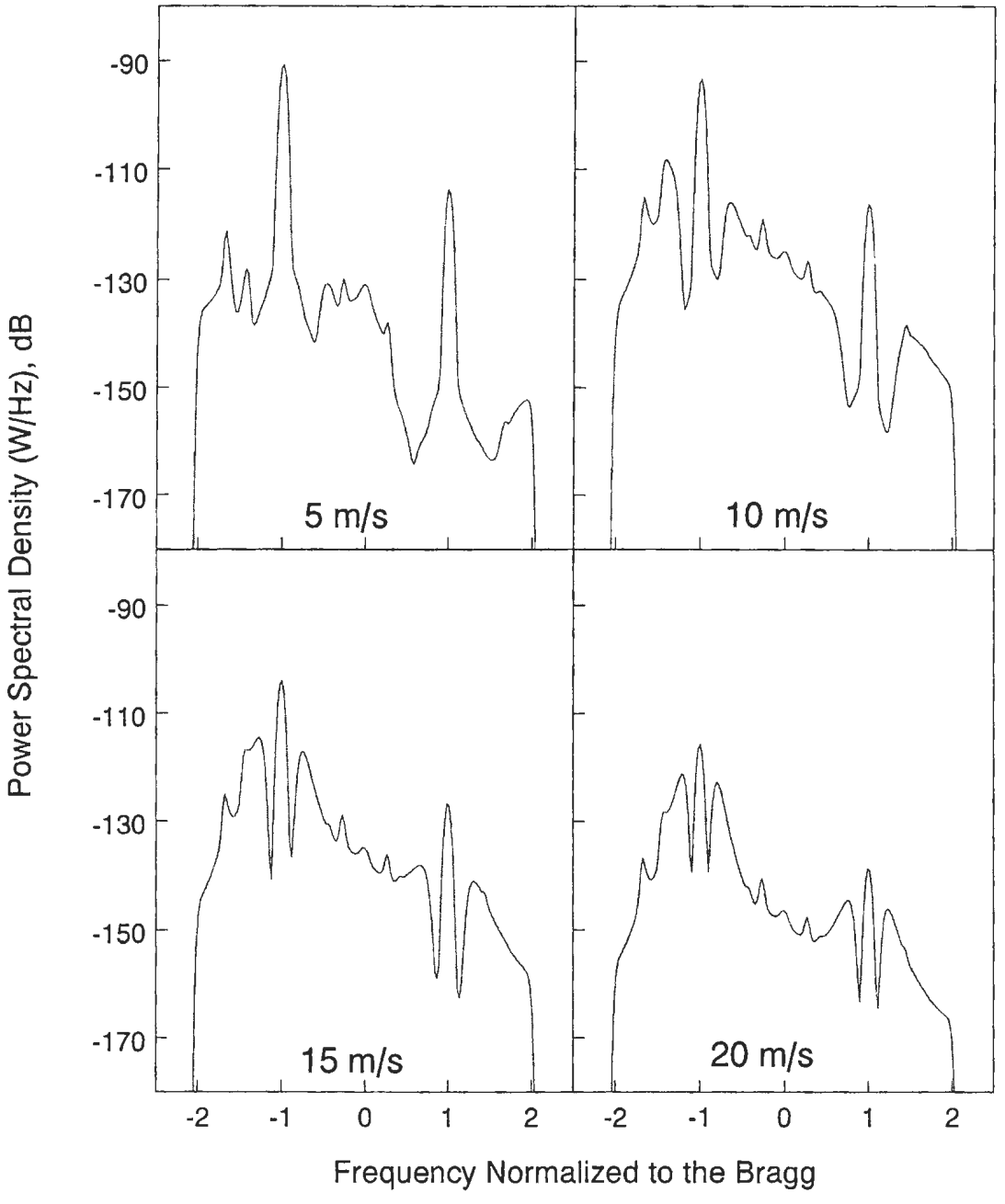

Figure 2.4: Simulated cross sections at various wind speeds at 10 MHz when the wind is 30° to the radar look direction.

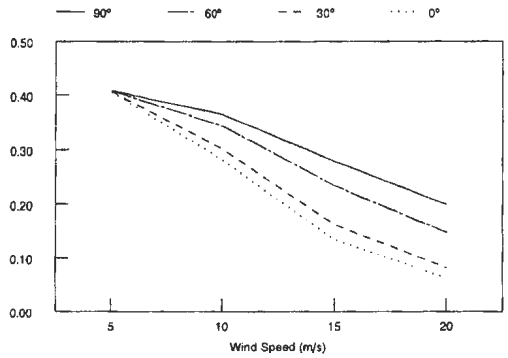

Figure 2.5: Values of the magnitude of the spherical earth attenuation at different wind speeds and directions.

fall of 2002 and real data is available at those frequencies.

Oceanographic parameters estimated from radar spectra are average values. The average is conducted over the horizontal extent of a range cell and also to a depth as defined by $\lambda_0/8\pi$ [21]. With regards to currents, it is possible to measure different depth-averaged values of the current by changing the radar frequency and, hence, generate the current profile over depth. In the HF band the depth probed is 3.98 m to 0.40 m in the range from 3 to 30 MHz, respectively.

It can be noticed from Figure 2.6 that as the frequency increases, the power in the second order spectra, relative to the first order, increases and becomes more distinct. Thus, phenomena that depend on second order effects, such as the waveheight directional spectrum, should be measured at higher frequencies.

While a radar transmitter may be capable of outputting energy across the full HF band, receivers must be designed more specifically. If the input bandwidth of a receiver is high then more external noise is present and there is a greater chance of unwanted signals being included. Using switchable prefilters is one way in which this problem may be mitigated.

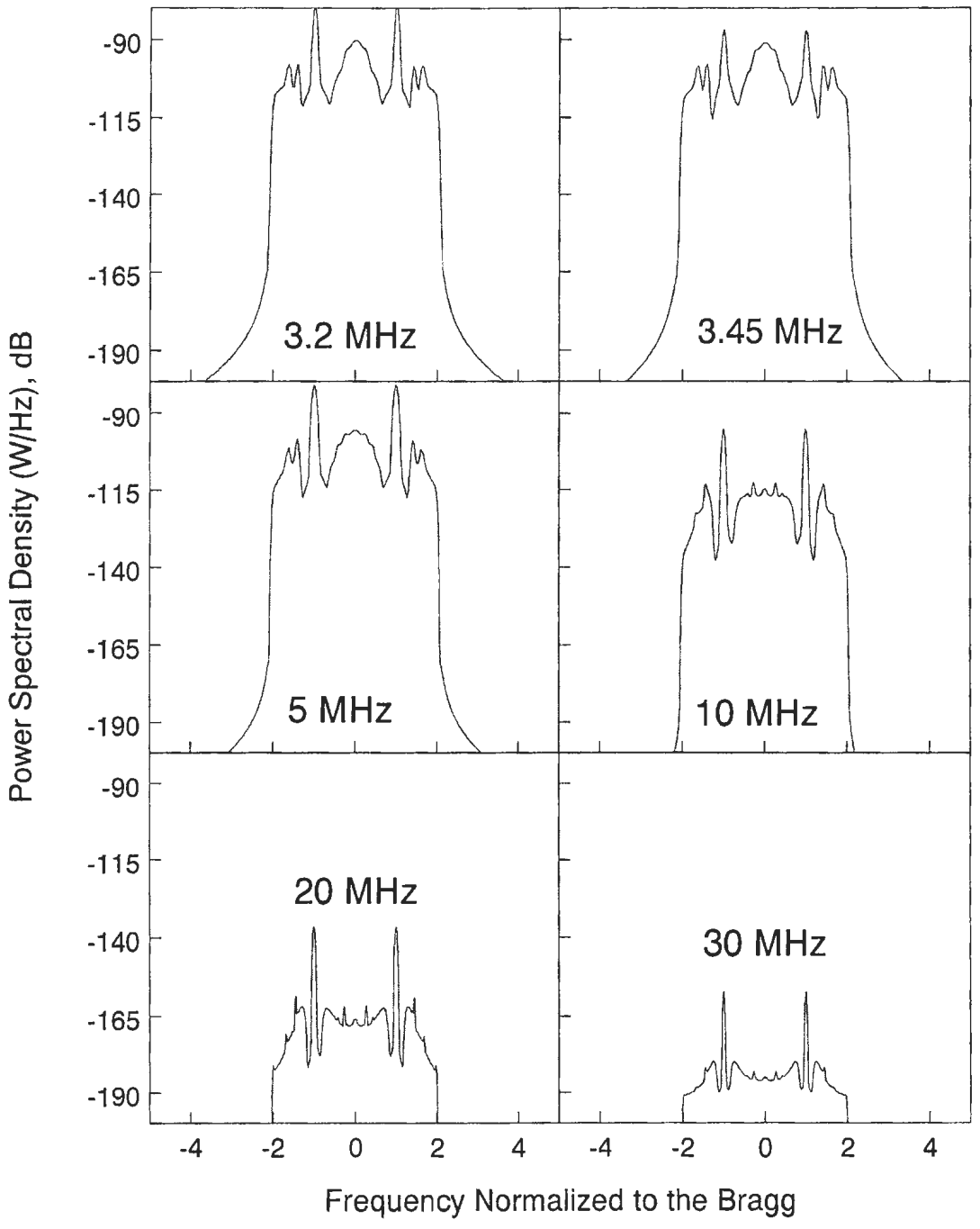

Figure 2.6: Simulated cross section spectra at several frequencies at a wind speed of 10 m/s and directed perpendicular to the radar look direction.

2.6 Extraction of Currents

The determination of current velocity is dependent on determining the locations of the Bragg peaks. In general, each of the two Bragg peaks is able to provide current information. One or both of the peaks will be used depending on their strength. If the wind is blowing nearly directly towards or away from the radar look direction the negative or positive Bragg peak, respectively, will be buried in the noise floor or barely rise above it. In these cases the remaining peak is used for finding the current. Typically, a peak should be at least 10 dB above the noise floor for it to be useful for current calculations [6].

When both peaks have a signal to noise ratio (SNR) greater than 10 dB, two options are available. The current can be found from each peak and then averaged to find the total current. The advantage of this approach is that the effect of random noise fluctuations, which affects each peak separately, will be diminished. The second method is to use only the peak that has the higher SNR. The advantage of using the single-sided spectrum is that only the highest quality data are used.

Regardless of how many peaks are used, the centroid definition is used to find the location of each peak. The following procedure can be used to find the centroid:

- Locate the approximate locations of the positive and negative first order Bragg peaks. The positive Bragg return should be the largest signal in the range $\omega_D > 0$ and the negative Bragg return should be the largest signal component in the range $\omega_D < 0$.

- For the negative Bragg peak, find the average value of the spectrum in the range $-1.8\omega_{B_n} < \omega_D < -1.2\omega_B$ and $-0.8\omega_{B_n} < \omega_D < -0.3\omega_{B_n}$ where ω_{B_n} is the approximate location of the negative Bragg peak. The average for the positive peak is conducted over the corresponding positive Doppler frequencies.

- Find the two first order nulls for each peak. Starting at the approximate location of each peak, the first order nulls are identified as the first set of local minima on each side of the Bragg peak whose values fall underneath the appropriate average.

- Integrate over the region between the two nulls. The point at which 50% of the area is covered is considered to be the location of the peak.

Once the frequency shift, or average frequency shift when both peaks are used, relative to the Bragg has been found, equation (1.5) can be used to find the radial current magnitude. A more elaborate description of the technique used will be given prior to discussion of the real data in Section 4.2.

Chapter 3

Two-Site Vector Currents and the Continuity Equation

The term vector current will be used to indicate a two-dimensional ocean surface current, with magnitude and direction in the horizontal plane being the two desired parameters. Given two spatially separated radar facilities that cover a common expanse of ocean, it is possible to produce a vector current. Radial currents may be derived from each set of radar data and both radial values can be combined to produce a vector. Of the various methods of determining the vector current from two radial projections from spatially separated radar sites, two will be considered in this chapter.

It is also possible to estimate vector currents using a single radar. If it is assumed that the spatial variability of the currents is of a larger scale than the size of a range cell, then multiple range cells can be combined. The multiple radial currents contributing to the true current are used to estimate the vector current.

Additionally, the continuity of flow equation may be used in a method having elements of both dual- and single-site approaches. Knowledge of vector currents must be known at a certain radar scan angle. Then, vector currents can be estimated at

adjacent locations as long as radial current data is present.

Since the continuity equation requires that vector currents be known within the region of dual-site overlap, it is important to employ a reliable method for finding what the vector currents are before applying the continuity equation. Sections 3.1 to 3.4 will be devoted to explaining the theory responsible for two methods of finding the vector currents, and the explanation of simulations; Sections 3.5 to 3.9 will focus on describing the issues associated with the continuity equation and then on presenting some simulations. The geometric relationship for determining vector currents that yields the better results will be used for the simulations involving the continuity technique and for analyzing the real data in Chapter 4.

3.1 Two-Site Vector Currents

A vector surface current consists of two components which can be expressed as: magnitude and direction, Cartesian components, or radial and tangential projections along a radar beam. Given two, non-parallel, one-dimensional current values it should be possible to construct a two-dimensional current. Although all representations of a vector are equivalent, the manner in which the current is actually calculated will affect the accuracy of the final measurement due to geometric constraints and the error associated with each of the radial values. The vector current will be found most accurately when the radial components are at right angles [2].

In Figure 3.1 the baseline connecting the radars is chosen to lie along the x-axis and the two radars are shown to be equally separated from the origin. The point P on the ocean surface being interrogated has the coordinates (x, y) and the distances to this point from each radar are r_1 and r_2. The measured radial components, V_1 and V_2, can be combined to yield the total current $\vec{V}$.

The radial velocities do not form an orthogonal reference frame and equation

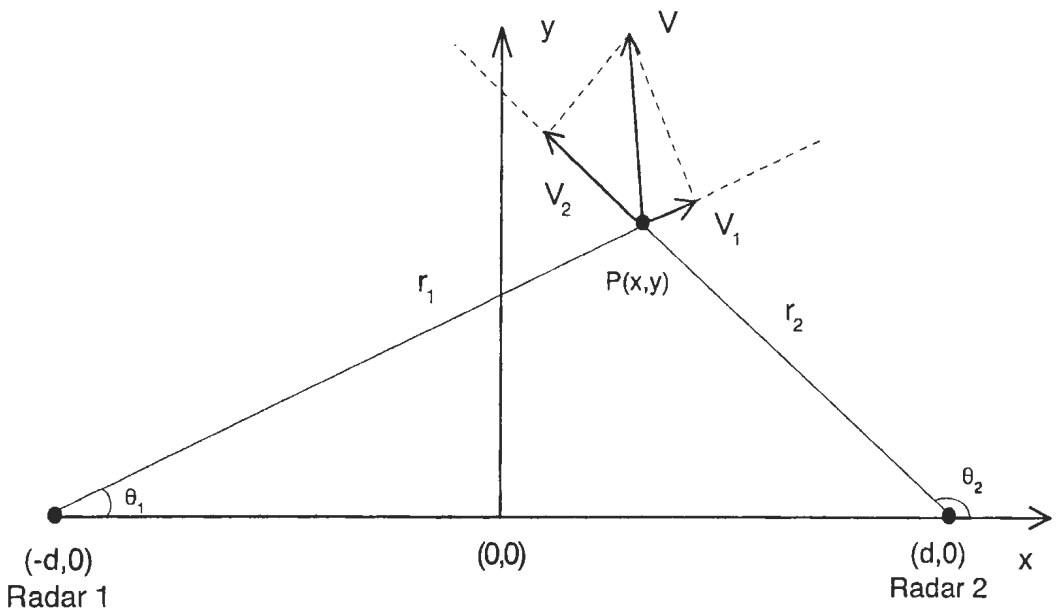

Figure 3.1: Geometry of a dual-radar system.

(3.1), derived from the geometry in Figure 3.1, can be used to determine the current in Cartesian coordinates. It can be seen that baseline instabilities will result for points close to the line joining the two sites since they would have small values of y. Results will also be compromised for distant points, when the radial components are almost parallel and the radial currents will be almost the same for both radars.

$$V_x = \frac{V_1 r_1 - V_2 r_2}{2d}$$
$$V_y = \frac{V_2 r_2 (x+d) - V_1 r_1 (x-d)}{2dy} \tag{3.1}$$

The method outlined above seems to indicate that any arbitrary location can be chosen on the ocean surface and the two radars can be steered to illuminate that spot. In reality, each radar will have a certain beamwidth and this beam can be steered over a certain azimuthal extent. For a pulsed radar, the range is broken up into different sections according to the length of the transmit pulse. Thus, the ocean is broken up into a series of range cells each of which cover a certain angular width and a fixed range resolution as noted in Section 1.4.3. The range cells for each radar are annular

sections whose centres are at fixed increments of range and azimuth from each radar. For the purposes of the research conducted, the overlap will be divided into the range cells of the reference radar. The vector current in that cell will be based on the radial value in the reference radar cell and an interpolation of the radial currents in four of the nearest surrounding cells of the secondary radar. Spatially resolving the overlap using the cells of the reference radar will be useful when considering the continuity equation beginning in Section 3.5.

The above method involves converting the radial current data into Cartesian coordinates. By working in the circular cylindrical system, another method can be used to find the radial and tangential components. Transformation to Cartesian or polar form can be performed after the vector is found. One of the radars must be chosen as the origin of the circular cylindrical system and its range cells will be used as the locations where vector currents will be deduced. With this choice of origin only the tangential component of the current needs to be found. With reference to Figure 3.2 the following equations can be written

$$\begin{aligned} V_r &= V_1 \\ V_t &= V_2 \cos\gamma \end{aligned} \tag{3.2}$$

or

$$\begin{aligned} V_r &= V_2 \\ V_t &= -V_1 \cos\gamma \end{aligned} \tag{3.3}$$

where the negative sign in (3.3) is included to maintain a right-handed coordinate system when the reference and secondary radar sites of Figure 3.2 are interchanged. In equation (3.2), V_r and V_t are the radial and tangential velocities, respectively, relative to the reference radar (Radar 1), and $\gamma = \theta_2 - 90° - \theta_1$. The angles θ_1 and θ_2 are the radar scan angles from each site to the desired region of ocean. If Radar 2

is chosen as the reference radar, then equation (3.3) applies and V_r and V_t are with respect to Radar 2.

The baseline instability problem remains but is reduced to being dependent on the look directions of each radar and expression in cylindrical coordinates facilitates the error analysis. The error bound on the radial component, Δv_r, is the Fast Fourier Transform (FFT) resolution error. Similarly, the error on the tangential component is limited by $\Delta v_r \cos\gamma$. Simulations mimicking the geometry of the Cape Race and Cape Bonavista systems have shown that the value of $\cos\gamma$ will vary from approximately 0.5 to 1.0. Thus, by using the higher value of 1.0, the error in the tangential current has the same distribution as the radial current error. Thus the tangential error can be approximated as $\Delta v_t = \Delta v_r$. Section 3.2 will discuss why noise and interference will not be a major source of error that needs to be considered.

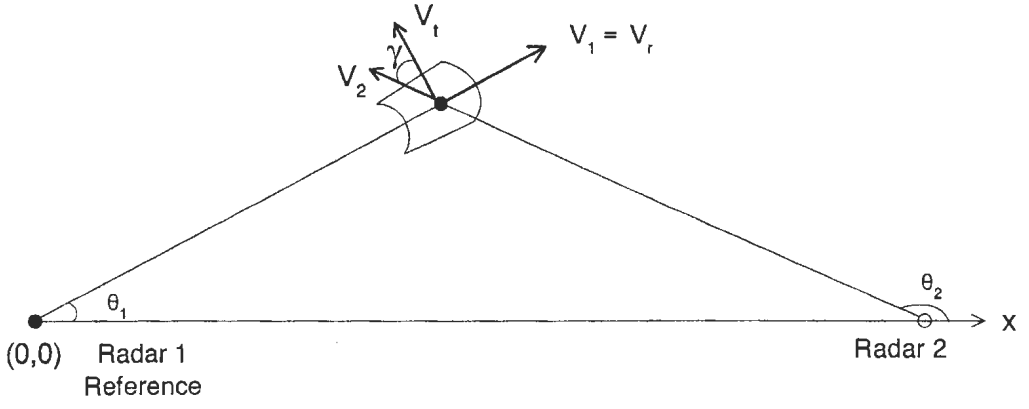

Figure 3.2: Calculation of vector currents in a cylindrical coordinate system.

While there are many other ways of finding the vector currents, only the two methods suggested by equations (3.1), (3.2) and (3.3) will be discussed here. Henceforth, use of equation (3.1) will be known as the Cartesian method, use of (3.2) and (3.3) will be referred to as the Cylindrical method.

3.2 Errors

At HF frequencies, a radar receiver is generally externally noise limited. Natural galactic and atmospheric noise and man-made signals will tend to degrade the signal to noise ratio (SNR) of the radar's measurements while the effects of internal noise will be minimal. However, data with insufficient SNR will be discarded so any significant degradations caused by external noise or interference will not affect the data set. When the SNR is sufficiently high, noise and interference should not affect the determination of currents. For the simulations conducted in this chapter it has been assumed that data with low SNR have been excluded; for the real data considered in Chapter 4 the low-SNR data have already been removed.

Two other sources of error may occur but are difficult to account for. When a ship moves at the same speed as the Bragg waves, the corresponding first order Bragg line will be broadened and the current calculation for that individual range cell will be distorted, but the surrounding cells will be unaffected. Any other problems with the radar facility will result in errors as well. These two types of errors are untraceable here since the author did not have access to individual Doppler spectra. Only the radial current values and the SNR were made available. Thus, such errors will not be quantified for inclusion within the error model.

Hence, assuming that there is no variability of currents within a range cell, each of the radial current values will have an error term which is wholly characterized by the resolution of the FFT. The FFT error is straightforward to quantify. First, the continuous time radar return is sampled at a certain rate, F_s, and this frequency is the full negative to positive width of the Doppler band. The frequency resolution, ΔF_s, resulting when an N-point FFT is performed on the sampled time series is

$$\Delta F_s = \pm \frac{0.5 F_s}{N} \tag{3.4}$$

The limits of the radial velocity error, Δv_r, can be found by replacing Δf with ΔF_s in (1.5). This error will have a uniform, random distribution and the values of Δv_r will lie within the limits imposed by (1.5) and (3.4).

It is clear that the FFT error in the radial components will affect the vector current calculations. When using the Cartesian method, the error for the x and y components of the velocity will vary with both range and azimuth and a uniform measure of the error cannot be specified. The Cylindrical method does have a consistent error term and the errors on the radial and tangential terms will be limited by the resolution of the FFT.

3.3 Dual-Site Simulation Setup

Simulations of the accuracy of the two methods are necessary so that a decision can be made regarding what method to apply to the real data. To ensure that simulations will illustrate what can be expected from the real data, all the parameters pertinent to the radar testing will be used here. The names and characteristics of the two radar facilities from which real data have been obtained are as follows:

Cape Race

Location: $46^\circ\, 39'\, 2''$ N, $53^\circ\, 5'\, 9''$ W

Range: $\rho \geq 65$ km

Azimuthal coverage: $35^\circ < \phi < 175^\circ$ clockwise from North

Range resolution: $\Delta\rho_s = 1500$ m

Beamwidth: $\Delta\phi_R = 3.338^\circ$

Frequency: 3.2 MHz

FFT resolution: 0.0019 Hz

Cape Bonavista

Location: $48° 41' 15''$ N $53° 5' 25''$ W

Range: $\rho \geq 65$ km

Azimuthal coverage: $47° < \phi < 130°$ clockwise from North

Range resolution: $\Delta\rho_s = 1500$ m

Beamwidth: $\Delta\phi_B = 2.867°$

Frequency: 3.45 MHz

FFT resolution: 0.0019 Hz

The subscripts of R and B on $\Delta\phi$ indicate values for Cape Race and Cape Bonavista, respectively. A diagram showing the locations and coverage areas of the radar facilities is given in Figure 3.3. Each radar will be taken in turn to be the reference, beginning with Cape Race. Maximum range will depend on the signal to noise ratio of the individual measurements. Since SNR changes constantly, no value for maximum range has been provided. Ranges exceeding 400 km have been achieved, but not consistently. The Cape Race system covers an expanse of approximately 186,000 km^2 while Cape Bonavista scans about 109,000 km^2 of the ocean surface. The stretch of ocean common to both radar sites is approximately 51,000 km^2. As noted in Section 2.6 the minimum acceptable SNR used here is 10 dB. For simulation purposes a maximum range of 399.5 km has been used which corresponds to 75 cells in range when averaging has been carried out across three consecutive cells in range. Averaging across three range cells in range is done to increase the length of each surface patch from 1500 m to 4500 m.

When Cape Race is used as the reference, the origin of the coordinate system is set as the location of the Cape Race radar. The $\hat{x}$-direction is taken as North and the $\hat{y}$-direction as East. To maintain a right-handed coordinate system the $\hat{z}$-direction must

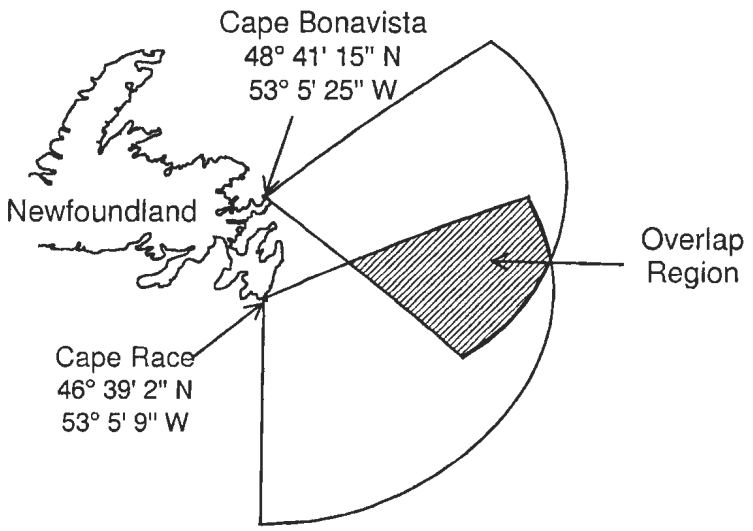

Figure 3.3: The Cape Race and Cape Bonavista radar systems located off the coast of Newfoundland, Canada.

be towards the centre of the earth. To convert to a cylindrical coordinate system, the origin remains fixed and the $\hat{\rho}$ component is the same as the radial value from Cape Race. To maintain the same right-handed system, it is necessary for the $\hat{\phi}$ component to correspond, roughly, to the direction of the radial current from Cape Bonavista. This situation is illustrated in Figure 3.4

Cape Bonavista is located 226.37 km North and 0.30 km West of Cape Race; both radar facilities are essentially on the x-axis. When Cape Bonavista is used as the reference, the location of that radar facility is set as the coordinate system origin. The x and y directions remain the same but now the $\hat{\rho}$-direction is aligned with the radial direction of Cape Bonavista and the positive tangential direction will be in the opposite direction to that specified by the radial direction of Cape Race as indicated by equation (3.3).

Since the two radar facilities have the same FFT resolutions but different operating frequencies, their current resolutions will be different. Using equation (1.5), Cape Race and Cape Bonavista have resolutions of ± 4.45 cm/s and ± 4.13 cm/s,

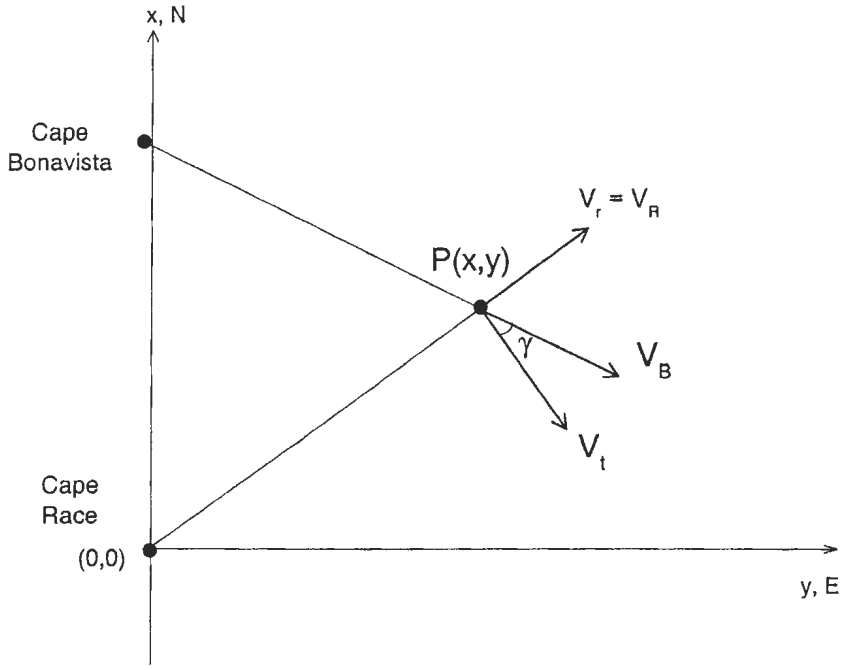

Figure 3.4: Coordinate system geometry when the Cape Race radar is used as the reference.

respectively.

3.3.1 Current Pattern for Testing Two-Site Techniques

Different methods of finding vector currents using dual-site data may display sensitivities to different current patterns. While all current patterns cannot be tested, the behaviour of the two methods can be reasonably predicted by using a constant current of various directions. Tests will be conducted for a current magnitude of 20 cm/s travelling in directions 0°, 30°, 60°, and 90° as measured from true North.

The radial component of the uniform currents will change with the radar scan angle and each range cell is considered separately. Therefore testing using a more realistic, spatially varying, current regime is unnecessary. However, a uniform current means that the radial component of the current at any given azimuth will be the same. Averaging across range, which is done to reduce the effect of the FFT error and

outlying values, will almost certainly produce a decrease in the error.

3.4 Dual-Site Simulation Results

Since each radar system has a different beamwidth and is scanned over a different angular extent, it is necessary to find the vector currents from the perspective of each radar. This information will be useful when assessing vector currents beyond the overlap.

The results have been analyzed by calculating the root mean square (RMS) error in magnitude and direction for each of the following range categories: $\rho < 200$ km, $200 < \rho < 250$ km, $250 < \rho < 300$ km, $300 < \rho < 350$ km and $\rho > 350$ km where ρ is the distance from the reference radar.

3.4.1 Cape Race as Reference

For all tests conducted at the specified current magnitudes and directions, the Cartesian method yielded excellent results. There were no observed instabilities at any of the angles; however the results did decline with range.

The results yielded from using the Cylindrical method are less consistent and the errors vary widely across range and azimuth. Except for the case when the current direction is due East, the error tends to increase with range. For this case the current direction is better estimated with the Cylindrical method, but the current magnitude is more closely predicted with the Cartesian relationship. In all cases the error increases with range. These trends in the error for the Cylindrical method are greater than the error predicted in Section 3.1. Examination of equations (3.2) and (3.3) reveals that V_t is required to be smaller than V_2. Any instances when V_t is larger than V_2 will result in an increased value of the error.

Figures 3.5 and 3.6 show the magnitude and direction errors for each two-site

method as a function of current direction. At all current directions the errors while using the Cartesian method are lower or comparable to those when using the Cylindrical method. Thus, the Cartesian method should be applied when finding the vector currents when Cape Race is used as the reference.

3.4.2 Cape Bonavista as Reference

Fortunately, the values of the vector current calculated using the Cartesian and Cylindrical methods when Cape Bonavista is the reference are very similar to the results when Cape Race is the reference. The Cartesian method still yields very good results and the accuracy of the values slightly decrease with range. The trends for the Cylindrical method remain the same as that for the Cape Race reference case. From Figures 3.5 and 3.6 it can be seen that in general the Cartesian method is better or comparable for all current directions. When the current direction is 60° from North the estimate of direction is better with the Cylindrical method although the calculuation of current magnitude is still better with the Cartesian method. For all other current directions the Cartesian method is superior and often by larger margins.

3.4.3 Summary

Regardless of whether Cape Race or Cape Bonavista is used as the reference, the Cartesian method is the better two-site relationship to compose the vector current. The minor differences found when each site is used as the reference may be attributed to the different beamwidths and azimuthal coverages as indicated in Section 3.3. These slight differences are insignificant but suggest that the two-site methods should be evaluated via simulations when applied to a different geometry.

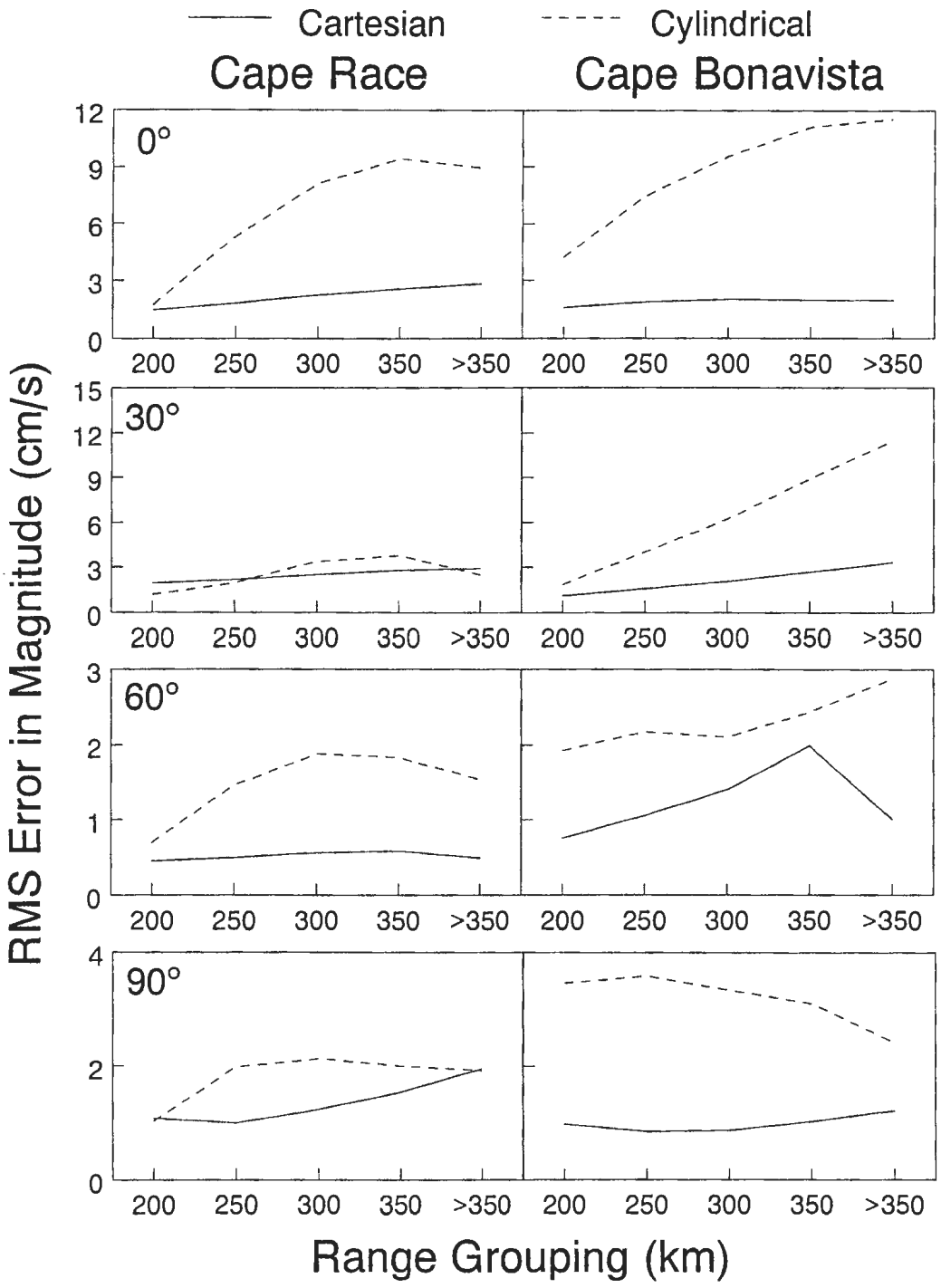

Figure 3.5: Comparison of the magnitude accuracies of the Cartesian and Cylindrical two-site methods when Cape Race and Cape Bonavista are each used as a reference. The current magnitude is 20 cm/s.

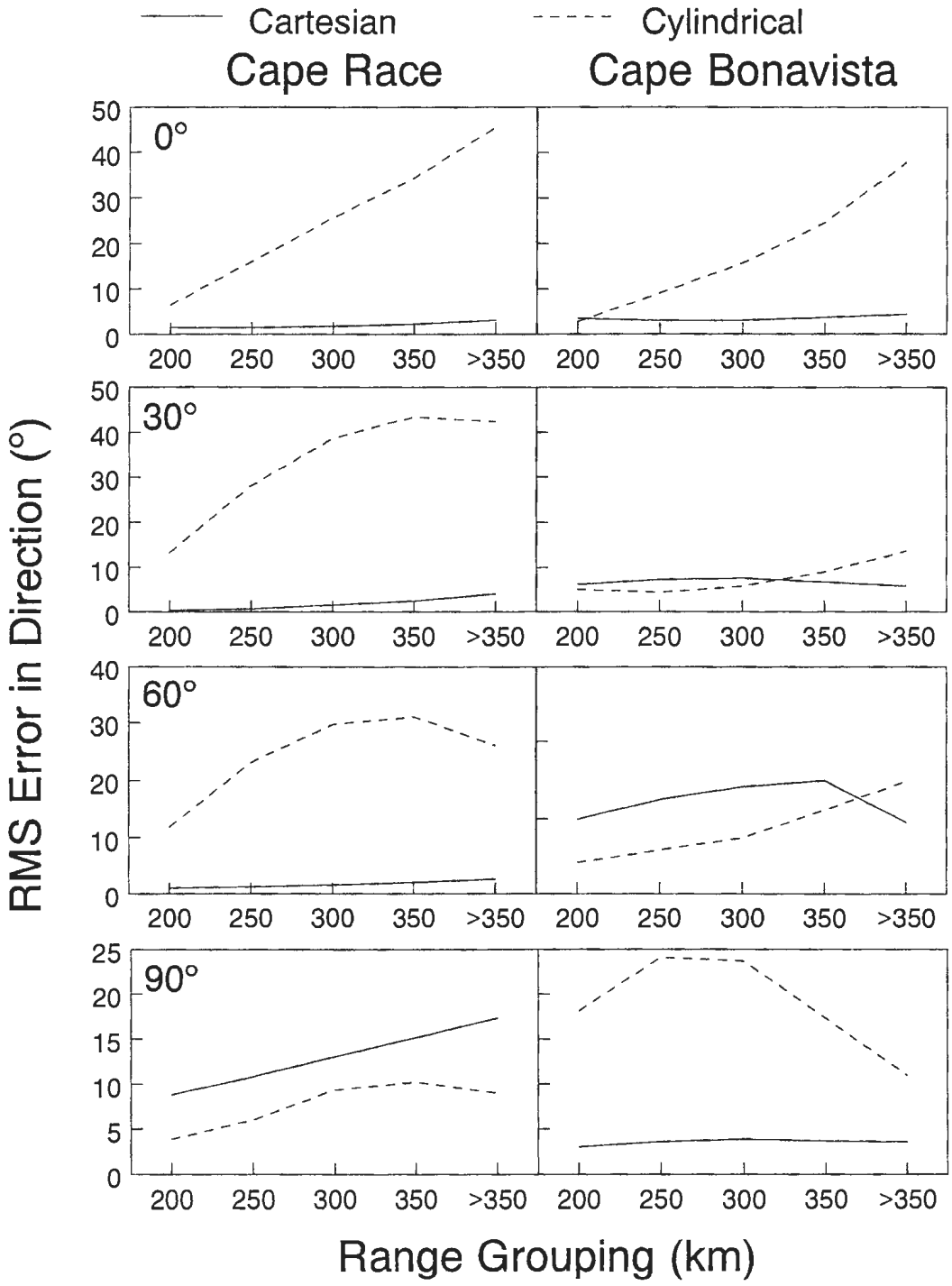

Figure 3.6: Comparison of the direction accuracies of the Cartesian and Cylindrical two-site methods when Cape Race and Cape Bonavista are each used as a reference. The current magnitude is 20 cm/s.

3.5 The Continuity Equation

It has been suggested that there are several ways to find the vector current when two radars interrogate the same region of ocean. However, the overlap region will be small relative to the individual coverage areas, and it is desired to expand the area over which vector information can be found.

One method that allows for the extension of knowledge of currents beyond the overlap involves the continuity of flow equation [35]. This special technique is functionally a combination of dual-site and single-site methods for finding the vector current. Vector current data within the overlap as well as radial values outside the overlap are used to estimate vector currents outside the overlap. In Section 3.1 it was stated that the overlap would be broken up into the range cells of the reference radar. This means the continuity technique only needs to be used to determine the tangential velocity to complete the current information. The basis for the continuity technique is the continuity equation as it is applied to hydrodynamics. Expressed in cylindrical coordinates the continuity equation is

$$\nabla \cdot \rho_w \vec{v} = \frac{1}{\rho}\frac{\partial}{\partial \rho}(\rho \rho_w v_\rho) + \frac{1}{\rho}\frac{\partial}{\phi}(\rho_w v_\phi) + \frac{\partial}{\partial z}(\rho_w v_z) = 0 \tag{3.5}$$

where $\vec{v}$ is the water velocity, v_ρ, v_ϕ, and v_z are the radial, tangential, and vertical velocity components, and ρ_w is the water density. The configuration of the radar deployment and the fact that range cells are best described in terms of radial and tangential components suggest that the circular cylindrical coordinate system be used. The original reseachers to use this technique [35] assumed that the vertical velocity gradient and horizontal density variations are negligible. Thus, the relation above reduces to one of conservation of volume in the horizontal plane,

$$\nabla \cdot \vec{v} = \frac{1}{\rho}\frac{\partial}{\partial \rho}(\rho v_\rho) + \frac{1}{\rho}\frac{\partial}{\phi} v_\phi = 0. \tag{3.6}$$

The elimination of dependence on horizontal density is reasonable [44]. In the original analysis, the vertical velocity gradient was omitted for convenience [35]. Vertical velocity is invisible to the radar since the radar can only measure the radial velocity. Equation (3.6) can be integrated quite easily to yield

$$v_\phi(\rho, \phi) = v_\phi(\rho, \phi_0) - \int_{\phi_0}^{\phi} \frac{\partial}{\partial \rho}[\rho v_\rho(\rho, \phi)] d\phi. \tag{3.7}$$

The derivative and integral can be calculated numerically. The expression $v_\phi(\phi_0, \rho)$ is the tangential velocity component as would be known at the edge of the overlap region. Hence, the above equation can be used to estimate the tangential velocity component starting at the edge of the common coverage area and working outwards. The partial derivative term in equation (3.7) is multiplied by range implying that any errors in calculation of the integral will be magnified as range increases. In terms of Figure 3.7, vector currents known at angle α_2 can be used to extrapolate tangential velocities in Radar 1 coverage. Similarly, vector currents known at angle α_1 can be used as the starting point for current vector estimation into the region covered by Radar 2. Thus, knowledge of currents in the overlap contributes to the solution for currents elsewhere. It should be noted that it is not necessary for vector currents to be known at all ranges at α_1 or α_2 to use the continuity equation. As equation (3.7) indicates, if the total velocity is known at a certain cell, then tangential values can be found for all other range cells at the same range. Lipa and Barrick [7] have used the continuity equation to estimate vector surface currents for a single radar system. By expressing the radial and tangential velocity components as a Fourier series over angle they were able to eliminate the need for knowledge of the tangential velocity at a certain azimuth and instead solved for an unknown Fourier coefficient. However,

no precise ground truthing was present for the data analyzed by Lipa and Barrick [7] or Frisch and Leise [35] and the systems involved were both short range, broad beam radars. As well, the results of [7] degraded strongly with distance and required special azimuthal scanning that limited the application of the algorithm. Also, as noted in Section 1.6, the author has found no work that evaluates the continuity technique for long-range, narrow-beam systems while taking into account the vertical velocity gradient.

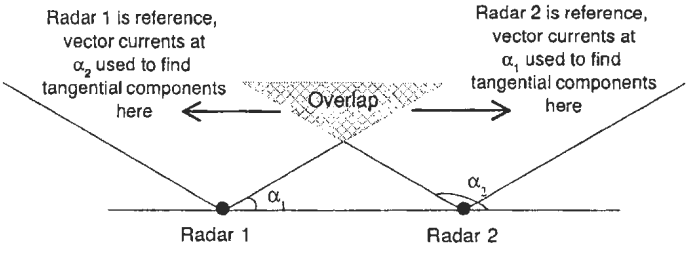

Figure 3.7: Geometry for using the continuity equation to estimate tangential velocity components.

The remainder of this chapter will be devoted to deriving a model that can describe the error due to exclusion of the vertical velocity gradient from the continuity technique and using this error in simulations of the technique.

3.6 Mid-latitude Circulation Model

Vertical motion on the surface of the ocean cannot be exactly predicted since it will depend on the unique flow pattern of a particular region. A mid-latitude circulation model is used to describe the flow. The aim of using the model is to mathematically express some of the important aspects of the flow for the purposes of including those results in the simulations. The mid-latitude circulation model is not intended to describe the water motion on the Grand Banks, which is the region from where the experimental data of Chapter 4 is gathered. The mathematical relationships and

description of the model presented in this section are taken from [10]. Some of the assumptions that apply to simplified mid-latitude circulation are:

1. The ocean basin is rectangular with sides parallel to the North-South and East-West axes (see Figure 3.8).
2. The ocean bottom is flat and the water is homogenous.
3. The forcing winds are directly parallel or anti-parallel to the East-West axis.
4. The lateral dimensions of the ocean are large.
5. Current magnitude is only a few centimeters per second.
6. Viscous effects are confined to the boundary layers.
7. Circulation is steady and governed by beta-plane dynamics (see below).
8. The ocean basin lies approximately between 15° and 45° latitude either North or South of the equator.

Beta-plane dynamics refer to the way the Coriolis parameter, f, is specified. The beta-plane expression for the Coriolis parameter is

$$f = 2\Omega \sin \varphi \tag{3.8}$$

where Ω is the angular rate of rotation of the earth, $\approx 8 \times 10^{-5} \mathrm{s}^{-1}$, and φ specifies location in degrees latitude. It is clear that the value of f is maximum at the poles and zero on the equator. If the angle φ is expressed in radians as

$$\varphi = \varphi_0 + x/\rho_e \tag{3.9}$$

where x is the distance beween φ_0 and φ, and ρ_e is the earth's radius, we have the beta-plane assumption. Since the earth's radius is approximately 6371 km and the

separation between degrees of latitude is $\approx$ 111.13 km, the x/ρ_e term in equation (3.9) is a small angle. Thus, using (3.8) in (3.9), performing a Taylor series expansion and ignoring terms above linear order we have

$$f = 2\Omega \sin\varphi_0 + 2\Omega \frac{x}{\rho_e} \cos\varphi_0. \tag{3.10}$$

Equation (3.10) can be simplified to

$$f = f_0 + \beta_0 x \tag{3.11}$$

where $f_0 = 2\Omega \sin\varphi_0$ is the average Coriolis parameter and $\beta_0 = 2\frac{\Omega}{\rho_e}\cos\varphi_0$. At mid-latitudes, normal values are

$$\begin{aligned} f_0 &= 8 \times 10^{-5} \cdot \mathrm{s}^{-1} \\ \beta_0 &= 2 \times 10^{-11} \mathrm{m}^{-1} \cdot \mathrm{s}^{-1}. \end{aligned} \tag{3.12}$$

The mid-latitude circulation model considers the ocean as three layers: the surface Ekman layer, the interior, and the bottom Ekman layer as shown in Figure 3.8. At the air-water and water-ocean floor boundaries, the vertical velocity is zero. At the bottom of the surface Ekman layer the vertical velocity is given by

$$v_z = \frac{1}{\rho_{0w} f_0} \left(\frac{\partial \tau^y}{\partial x} - \frac{\partial \tau^x}{\partial y} \right) \tag{3.13}$$

where ρ_{0w} is the average value of the water density for which 1028 kg·m^{-3} is an acceptable value, τ^y is the East-West wind stress, and τ^x is the North-South wind stress. The expression $(\partial\tau^y/\partial x - \partial\tau^x/\partial y)$ is the wind stress curl.

The depth of the surface layer, Δz, is given by the expression

$$\Delta z = \sqrt{\frac{2\nu}{f}} \tag{3.14}$$

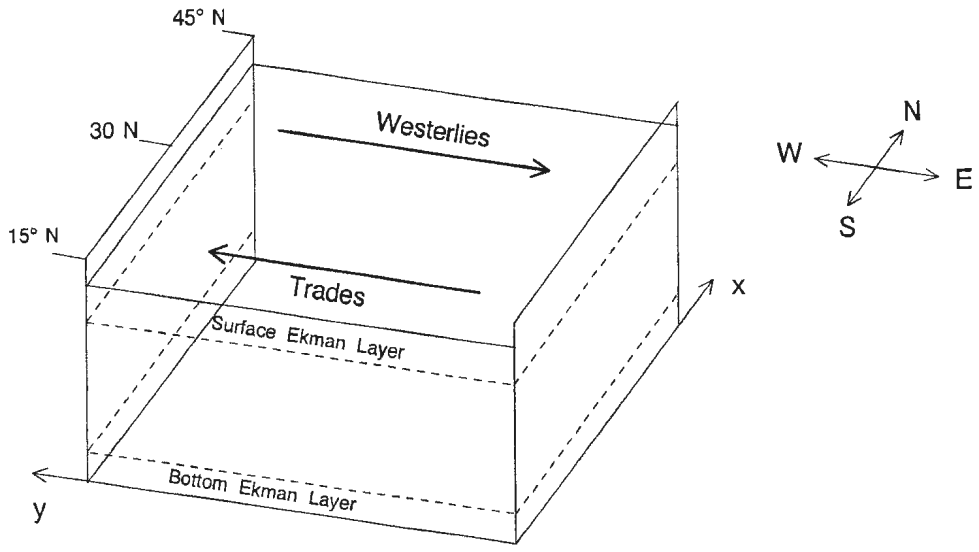

Figure 3.8: Model ocean basin used for mid-latitude circulation model.

where ν is the kinematic viscosity of the water.

Due to the beta-plane approximation of equation (3.11), the Coriolis parameter and the Ekman depth will vary with latitude. These variations are negligible over a radar's coverage area so we can let $f = f_0$ turning equation (3.14) to

$$\Delta z = \sqrt{\frac{2\nu}{f_0}} \tag{3.15}$$

It should be noted that this model only takes into account wind driven currents. Other current producing mechanisms are tides, geostrophy and waves [4]. It is known that winds and tides are generally the largest contributors to surface motion [1], [43].

3.7 Error Estimation

When applying the continuity equation, there are three types of errors: FFT resolution errors, errors caused by neglecting the vertical velocity gradient, and errors from applying the technique across several iterations. Since vector currents will be

constructed from two radial values, the tangential current known in the overlap is also affected along with the $\partial/\partial\rho$ term found in (3.7). The results of the simulations discussed in Section 3.4 indicated that the Cartesian method should be used for calculating the vector currents. However, since the error in finding the vector currents via the Cartesian method is not uniform over range and azimuth due to the nature of equation (3.1), the error predicted with the Cylindrical method will be applied as an upper limit on the error. The theoretical equivalence of tangential errors to radial errors for the Cylindrical method is discussed in Section 3.1. A description of the FFT errors has been provided in Section 3.2.

The second source of error comes from ignoring the vertical velocity gradient. Unlike the periodogram error there is no way to absolutely determine the true nature and magnitude of this uncertainty since it is dependent on the flow. The error can be approximated by making some assumptions regarding the nature of the current field and by using typical values for its spatial variability. There have been no previous attempts to characterize the error associated with omitting the vertical velocity gradient from the calculations. This error term will only be applied to simulations; real current flows are already three-dimensional.

Since successive estimates of the the tangential current are based on previous estimates, it can be expected that the errors will propagate and the quality of the extrapolations will decrease as distance from the original overlap increases.

3.7.1 Vertical Velocity Gradient

It has been stated that the mid-latitude circulation model is not intended to describe the vertical motion for any flow pattern. However, location specific information of the vertical velocity gradient would be useful for analyzing the result in Chapter 4 and for verifying if the mid-latitude circulation model is indeed valid.

First, the vertical velocity gradient error for the continuity equation based on the mid-latitude circulation model is determined. Then, a scaling analysis is used to find the same when applied to the Grand Banks of Newfoundland for the time of year in which the experiment took place.

Mid-Latitude Circulation

In Section 3.6 a model that can account for vertical motion near the surface of the ocean was developed. The measure of error that will be found for this motion is not exact and the analysis is done merely to suggest reasonable values for the error. It has been stated that at the water surface the vertical velocity is zero and that at the bottom of the surface Ekman layer the vertical velocity is given by (3.13). While no data for the wind stress curl could be found for the Grand Banks off the coast of Newfoundland, tests conducted off the California coast [45] showed that the wind stress curl fell within the range

$$\left(\frac{\partial \tau^y}{\partial x} - \frac{\partial \tau^x}{\partial y}\right) \in [-10^{-6}, 10^{-6}] \text{ kg/s}^2\cdot\text{m}^2. \tag{3.16}$$

For the purposes of this analysis it is assumed that the wind stress curl will vary uniformly within the limits imposed by (3.16). Substituting (3.16) into (3.13) shows that the vertical velocity at the bottom of the surface layer is

$$v_z \in [-1.22 \times 10^{-3}, 1.22 \times 10^{-3}] \text{ cm/s}. \tag{3.17}$$

The nominal viscosity of water [10] is $10^{-6}\text{m}^2/\text{s}$, however the eddy-intensified value of ν is

$$\nu = 10^{-2}\text{m}^2/\text{s}. \tag{3.18}$$

Due to contact with the wind at the ocean surface it is reasonable to use the higher value of viscosity. In estimating the vertical velocity gradient, it is important to realize that the radar is only capable of measuring spatial and temporal averages of the flow.

Using (3.12), (3.15), and (3.18) it is found that

$$\Delta z \approx 15\text{m}. \tag{3.19}$$

Using equations (3.17) and (3.19) and the knowledge that the vertical velocity is zero at the water surface we can make the approximation

$$\frac{\partial v_z}{\partial z} \simeq \frac{\Delta v_z}{\Delta z} \in [-8.133 \times 10^{-7}, 8.133 \times 10^{-7}]\ \text{s}^{-1}. \tag{3.20}$$

The implicit assumption, that the vertical velocity gradient is uniform, given in (3.20), is a reasonable one. It has been found [21] that the radar inherently measures a depth-averaged current, albeit for a depth shallower than the Ekman depth at HF frequencies. Although the vertical velocity in the boundary layer will vary non-linearly, the average value will not differ much when linear variation is assumed. For radar-deduced currents, only average transport over the surface layer is important.

There is no correlation between the horizontal and vertical gradients. Thus, the vertical gradient can be assumed to vary uniformly and randomly within the range $\pm 8.133 \times 10^{-7}\text{s}^{-1}$ for each range cell.

The error estimate that is required is not the value of the vertical velocity gradient as presented in (3.20), but rather the effect that omitting that term has on the calculation of the tangential velocity. Taking (3.5) and ignoring horizontal and vertical density variations, but retaining the vertical gradient we have

$$\nabla \cdot \vec{v} = \frac{1}{\rho}\frac{\partial}{\partial \rho}(\rho v_\rho) + \frac{1}{\rho}\frac{\partial}{\partial \phi} v_\phi + \frac{\partial}{\partial z} v_z = 0. \tag{3.21}$$

Directly integrating (3.21) to solve for the tangential velocity yields

$$v_\phi(\phi,\rho) = v_\phi(\phi_0,\rho) - \int_{\phi_0}^{\phi} \frac{\partial}{\partial\rho}[\rho v_\rho(\phi,\rho)]d\phi - \rho\int_{\phi_0}^{\phi}\frac{\partial}{\partial z}v_z d\phi. \tag{3.22}$$

The presence of the ρ multiplier on the final term of (3.22) indicates that the error induced by ignoring the vertical velocity gradient will increase with range. The errors in the integral of the radial component of the velocity will also increase with range, but this error can be predicted. It may be recalled that the continuity equation is solved across azimuth and vector velocities in one range cell are used to estimate the tangential component at an adjacent cell at the same range. Therefore, the final value of the error associated with using the continuity equation while ignoring vertical motion, Δv_{vert}, is

$$\Delta v_{\text{vert}} = \rho\Delta\phi\frac{\partial v_z}{\partial z}. \tag{3.23}$$

Equation (3.23) indicates the error which comes from ignoring the vertical velocity gradient in any single calculation. The total error over one or more iterations is considered in the next section.

The vertical motion of the water caused by waves is totally omitted from this analysis. Sinusoidal waves on the surface of the ocean have the effect of moving water molecules in circular orbits [11]. If we consider all the wave crests and troughs in a range cell over the duration of radar interrogation, the average vertical motion caused by wave action will be negligible.

Scaling Analysis

Vertical motion in the ocean is typically so small that its measurement eludes direct techniques. A scaling analysis, using information related to the real data in Chapter 4, can be used to predict the order of magnitude of the vertical flow structure.

It is well known that the ratio of vertical to horizontal length scale is approximately the same as the vertical to horizontal velocity scale. That is,

$$\frac{Z}{L} \approx \frac{v_z}{V_U} \tag{3.24}$$

where Z is the water depth, L is the horizontal scale, and V_U is the horizontal velocity.

By selecting appropriate values for Z, L, and V_U based on experimental data, the value of the vertical velocity gradient can be estimated by the ratio of v_z/Z. The values for each of the terms will be specified to the nearest order of magnitude. Section 3.3 indicates the coverage areas of the Cape Race and Cape Bonavista radar facilities. It is known that the radars will probe the Grand Banks of Newfoundland, which lie on the continental shelf which has a depth of 100 m. Hence, the vertical scale is $Z = 100$ m.

The radar beamwidth for each radar is roughly 3° which means that at a distance of 200 km, which is close to the start of overlap region, the width of a cell in azimuthal is about 10 km. Thus, it is possible to measure variations in the current on a scale of 10 km and $L = 10,000$ m.

From the experimental data used in Chapter 4 it is known that flow on the Grand Banks can achieve velocities of several tens of centimeters per second. However, the average velocities examined in the analysis were generally under 20 cm/s suggesting that a reasonable current scaling is $V_U = 0.1$ m/s.

Manipulating (3.24) and using estimated parameters yields

$$\frac{V_z}{Z} \approx \frac{\partial v_z}{\partial z} \approx 10^{-5}. \tag{3.25}$$

The value of the vertical velocity gradient derived from the mid-latitude circulation model, given in equation (3.20), was approximately 10^{-6}. The value from the scaling analysis is one order of magnitude higher suggesting that the vertical motion error is

likewise inflated. Fortunately, the experimental data was collected during the summer and fall seasons. At these times, the water is stratified; layers of the ocean are at certain temperatures and there is very little mixing between the layers. The density stratification resists vertical motion of the water which suggests the vertical velocity gradient is likely to be less than the 10^{-5} value calculated through the scaling analysis and closer to the 10^{-6} value generated via the mid-latitude circulation model. Thus, the value of the vertical velocity gradient given in equation (3.20) will be retained for use in the simulations [44].

3.7.2 Iteration Error

The nature of the algorithm is that past estimates of the tangential velocity are used to contribute to future extrapolations. Since each estimate is subject to the errors mentioned above, the overall error will naturally increase at locations distant from the overlap.

The error will be examined in stages and typical case values will be given. It should be noted that the radial current estimate will be most significantly impacted by the FFT resolution error. The tangential inaccuracy will depend on range, range cell length, number of range cells used for averaging, beamwidth, the radial current error and the error in neglecting the vertical gradient, Δv_{vert}. The average error will be considered using a beamwidth $\Delta\phi = 4°$, range $\rho = 200$ km, range cell length $\Delta\rho_s = 1.5$ km and $n = 3$ range cells for averaging. The radar frequency is 10 MHz with a sampling interval of 0.25 s and a 512 point FFT is used.

The first stage is at the edge of the overlap and the error on the tangential component is set as being the same as that in the radial current.

Radial Current Error

Given the above parameters, the maximum radial uncertainty will be ±5.86 cm/s and the tangential current error will be the same within the overlap. Since these errors are due to the resolution of the FFT, the error will be uniformly distributed between the maximum and minimum values. Treating the radial current error as a random variable with uniform distribution, the standard deviation of the error (see, for example [46]) can be found to be 3.38 cm/s. Since the radial error has zero mean, a reasonable measure of the error, Δv_r, will be the value at one standard deviation from the mean

$$\Delta v_r = \pm 3.38 \text{cm/s}. \tag{3.26}$$

Averaging across multiple range cells will tend to decrease this error even further, but the effect of averaging is not discussed here.

Integration Error

Use of the continuity equation in (3.7) requires an integral to be calculated. For the purposes of clarity, the integral is restated.

$$\int_{\phi_0}^{\phi} \frac{\partial}{\partial \rho}[\rho v_\rho(\rho, \phi)] d\phi \tag{3.27}$$

The integral of (3.27) must be calculated numerically and is taken as the average of the partial derivative covering both the cell where the full vector current is known and the adjacent cell where the estimate is to be made. The integral can be expanded numerically as

$$\int_{\phi_0}^{\phi}[\cdot] = \frac{1}{2}\left[\frac{(\rho + n\Delta\rho_s)v_{\rho_1} - (\rho - n\Delta\rho_s)v_{\rho_2}}{n\Delta\rho_s} + \frac{(\rho + n\Delta\rho_s)v_{\rho_3} - (\rho - n\Delta\rho_s)v_{\rho_4}}{n\Delta\rho_s}\right]\Delta\phi \tag{3.28}$$

where the terms v_{ρ_1} and v_{ρ_2} indicate the respective radial velocities above and below the cell where the tangential current is known, and v_{ρ_3} and v_{ρ_4} are the respective radial velocities above and below the cell where the tangential current is to be estimated. The average of the partial derivative across the two cells has been used.

Including errors on each of the radial current estimates, the integral can be expressed as

$$\int_{\phi_0}^{\phi}[\cdot] = \frac{1}{2}\left[\frac{(\rho + n\Delta\rho_s)(v_{\rho_1} \pm \Delta v_{\rho_1}) - (\rho - n\Delta\rho_s)(v_{\rho_2} \pm \Delta v_{\rho_2})}{n\Delta\rho_s} + \frac{(\rho + n\Delta\rho_s)(v_{\rho_3} \pm \Delta v_{\rho_3}) - (\rho - n\Delta\rho_s)(v_{\rho_4} \pm \Delta v_{\rho_4})}{n\Delta\rho_s}\right]\Delta\phi \qquad (3.29)$$

where the subscripts on the error terms, Δv_ρ, are named corresponding to the v_ρ terms. Each of the random error terms can be considered as a random variable making equation (3.29) a function of four random variables. Since the sum of the errors is involved, the error will no longer be uniform and will have a greater concentration of values near zero and fewer near the error bounds.

Note that the error from using the integral, like the vertical velocity gradient error, increases with range. The variance of a function of several random variables can be deduced from [46] and the resulting error will also be a random variable. It should be noted that the radial current errors, v_{ρ_1} to v_{ρ_4}, have zero mean and are uniformly distributed and independent. Using the parameters listed at the start of Section 3.7.2 including the radial error, Δv_r of equation 3.26 the variance of the error of equation (3.29) will be 115.10 $\mathrm{cm}^2/\mathrm{s}^2$ and the error within a single standard deviation will be

$$\Delta v_{\mathrm{int}} = \pm 10.73 \mathrm{cm/s}. \qquad (3.30)$$

Vertical Motion Error

The vertical motion error has been described by equations (3.20) and (3.23) and for the parameters listed above will lie within the limits ± 1.14 cm/s. The vertical motion error will be uniformly distributed since the values of the wind stress curl given in equation (3.16), upon which the vertical velocity gradient are based, are assumed to have a uniform distribution. The expected value of the error due to vertical motion is

$$\Delta v_{\text{vert}} = \pm 0.66 \text{cm/s}. \tag{3.31}$$

The unknown error in estimating the vertical motion is much smaller than the error introduced from calculation of the integral.

Error Propagation

Using the error terms of the previous sections, the propagation of errors can be calculated as the distance from the original overlap increases. Since each of the error terms are random variables, the variance of the total error will be sum of the variances of the individual terms. The edge of the overlap region will be considered as the first stage of the analysis. The values given below are for a single standardard deviation from the mean.

Edge of Overlap Typical Error (First Stage)

$v_r : \Delta v_r : \pm 3.38$ cm/s

$v_{t,1} : \Delta v_r : \pm 3.38$ cm/s

First Extension Cell Typical Error

$v_r : \Delta v_r : \pm 3.38$ cm/s

$v_{t,2} : \Delta v_{\text{int}} + \Delta v_{\text{vert}} + v_{t,1} : \pm 11.27$ cm/s

Second Extension Cell Typical Error

$v_r : \Delta v_r : \pm 3.38$ cm/s

$v_{t,3} : \Delta v_{\text{int}} + \Delta v_{\text{vert}} + v_{t,2} : \pm 15.57$ cm/s

Third Extension Cell Typical Error

$v_r : \Delta v_r : \pm 3.38$ cm/s

$v_{t,4} : \Delta v_{\text{int}} + \Delta v_{\text{vert}} + v_{t,3} : \pm 18.92$ cm/s

Fourth Extension Cell Typical Error

$v_r : \Delta v_r : \pm 3.38$ cm/s

$v_{t,5} : \Delta v_{\text{int}} + \Delta v_{\text{vert}} + v_{t,4} : \pm 21.76$ cm/s

Each iteration of the continuity technique leads to the estimation of vector currents at a range cell progressively removed from the overlap; the overlap is essentially being extended. The increase in error as the number of iterations increases is likely to be mitigated by averaging across range cells. Thus, the error may be lower than the typical values presented here.

As is clear from equation (3.22), the error in each new stage of using the technique is based on the error in the previous stages, the error from ignoring the vertical velocity gradient and the error from calculating the integral of the $\partial/\partial\rho$ term.

3.7.3 Error Presentation

The correlation coefficient, r, is one way to compare a set of experimental values with a set of more reliable values. Varying between -1 and 1, it quantifies how well the

two sets of data plotted against each other can be approximated by a line of unity slope passing through the origin. However, when the data do not cover a wide range of values, correlation will not be an accurate indication of the comparison. In such cases, the root mean square (RMS) definition of error is preferrable since it is not limited by the extent of the range of values and is more sensitive to any outliers that are present.

For the simulations that follow, the RMS error is what will be indicated. In Chapter 4 both the correlation coefficient and the RMS error will be used to analyze the results when applying the continuity equation to real data.

3.8 Continuity Simulation Setup

Simulations have been carried out under several conditions in order to check the sensitivity of the technique. All tests have been done at a radar operating frequency of 10 MHz and it is assumed that an FFT has been performed on the radar time series to obtain the Doppler spectrum. The sampling interval used in the time series is 0.25 s and 512 points have been used for the FFT. From equations (1.5) and (3.4), the radial error will be ± 5.86cm/s. As discussed in Section 3.1, the tangential component of the current calculated using the two-site method can be approximated as having the same error. Errors in the radial measurements will have the greatest adverse effect on low-magnitude currents and currents that are directed such that their radial or tangential components are small.

For each of the current patterns discussed in Section 3.8.2, the simulation will be carried out 1000 times. Instead of averaging across all test runs, the only data stored will be the radial and tangential values when the tangential current deviates the furthest from the true value. This scheme does not ensure that the worst radial currents will be stored and differs from the typical case error discussed in Section 3.7.2 since

an average error is not ensured at any point. The radial error will be constrained by the resolution of the FFT, whose value is given in Section 3.7.2. For these simulations, the worst case radial error will not differ from a typical case by more than a few centimeters per second.

3.8.1 Geometry

The geometry of the simulations is based about a single radar system. The radar has a beamwidth of 4° and azimuthal coverage of 120°, from 30° to 150°. Range cell length, $\Delta\rho_s$ is 1.5 km. The currents in three range cells, adjacent in range, are averaged and this average is assigned to the area covered by the three cells. It is assumed that vector currents are known at the range cells centered at 32°.

The radar blind zone extends to a distance of 66.5 km from shore and valid measurements are made up to 399.5 km in terms of the centres of the first and last range cells. Unlike with real data, there are no lapses in the coverage zone and the accuracy of the results will not decline at the limits of the radar's capabilities. Vector currents are assumed to be known at all ranges after the blind distance at an azimuth of 32°. Figure 3.9 illustrates the geometry for the system.

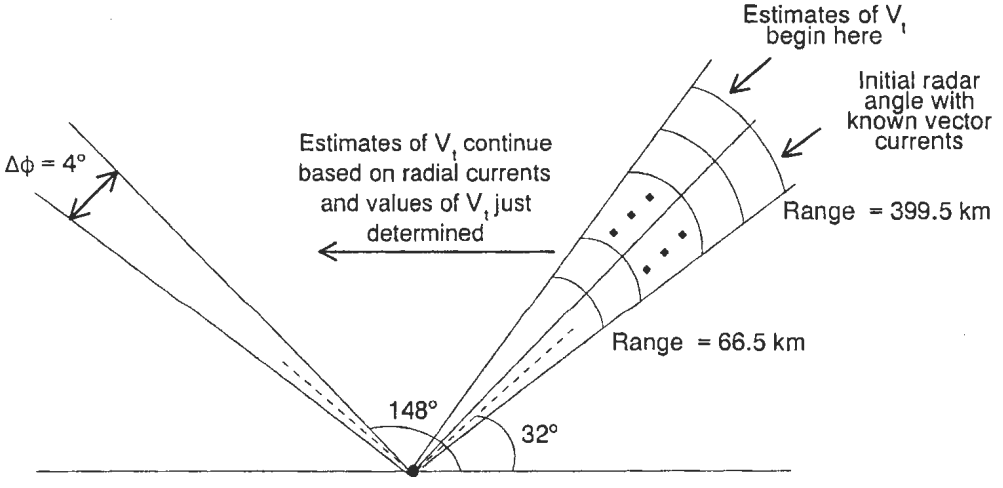

Figure 3.9: Setup for simulations testing the continuity technique.

3.8.2 Current Patterns

The results of using the continuity approach will depend on the nature of the current field chosen. Uniform currents, with magnitudes of 20, 50, and 80 cm/s at directions of 0°, 30°, 60°, and 90° with respect to the initial radar angle of 32°, will be used. The uniform currents have zero horizontal divergence and the errors regarding the omission of the vertical velocity gradient are included to emulate three dimensional flow.

The current is specified in terms of the start angle of the analysis since, for the single radar setup, the radial currents will be dependent on the angle between the start angle and the current direction and the current magnitude. Examples of a current map and an analysis of the results will be presented in later sections.

While uniform currents can be used to predict how the techniques will respond to specific situations, a variable current is good for examining how well the technique will work with real data. As with the estimation of error for neglecting the vertical velocity gradient, the analysis conducted to develop a current regime is approximate and is not intended to imitate the exact motion of specific current flows. Rather, the aim is to develop a current whose major parameters take on realistic values. The parameters of interest are horizontal and vertical current magnitudes and horizontal spatial variability. As well, the radial and tangential values of the current should have comparable magnitudes and the flow should be a function of range and azimuth.

The issue of vertical current magnitude has already been satisfied in Section 3.7.1 and proper horizontal current strength can be achieved by choosing a mathematical model for a flow field and then multiplying the equations in the model by a scalar to achieve the appropriate values. Experiments conducted in the Dead Sea [19] show that the divergence and curl of the current field were limited by $|f_0/2|$.

As with the uniform current, the variable current will have zero horizontal diver-

gence and the error associated with ignoring vertical motion is added separately. The total current was found by assigning the radial component of the velocity and then integrating (3.6) to determine the tangential velocity. The trigonometric functions of $\sin(\cdot)$ and $\cos(\cdot)$ are known to vary smoothly between predictable bounds. It was decided to make the radial current a product of two $\sin(\cdot)$ or $\cos(\cdot)$ functions with one term in the product solely responsible for variation with range and the other for variation with azimuth. Through trial and error a form of the radial component of the velocity field that conformed to the requirements of magnitude and spatial variability was determined to be

$$V_\rho = a\cos\left(\frac{\rho - b}{c}\right)\sin(d\phi) \tag{3.32}$$

where the values of a, b, c and d govern the magnitude and variability of the current. Parameter a is a scalar multiplier that limits the current magnitude. The values of c and d affect the frequency of variation of the range and azimuth dependent terms respectively. To accomodate the full extent of range values, b is used to shift the range-dependent current term. By direct integration of (3.6) and setting the integration constant to zero, the tangential velocity, V_t, is determined to be

$$V_t = \frac{a}{d}\left(\cos\frac{\rho - b}{c} - \frac{\rho}{c}\sin\frac{\rho - b}{c}\right)\cos(d\phi). \tag{3.33}$$

It has been found that choosing values for b, c and d as 150 km, 60 km and 2 respectively yields partial spatial derivatives of the order suggested by [19] in the radar coverage zone. Values of a used for the simulations are 0.2, 0.4, and 0.6. An example of the current pattern for when $a = 0.2$ is provided.

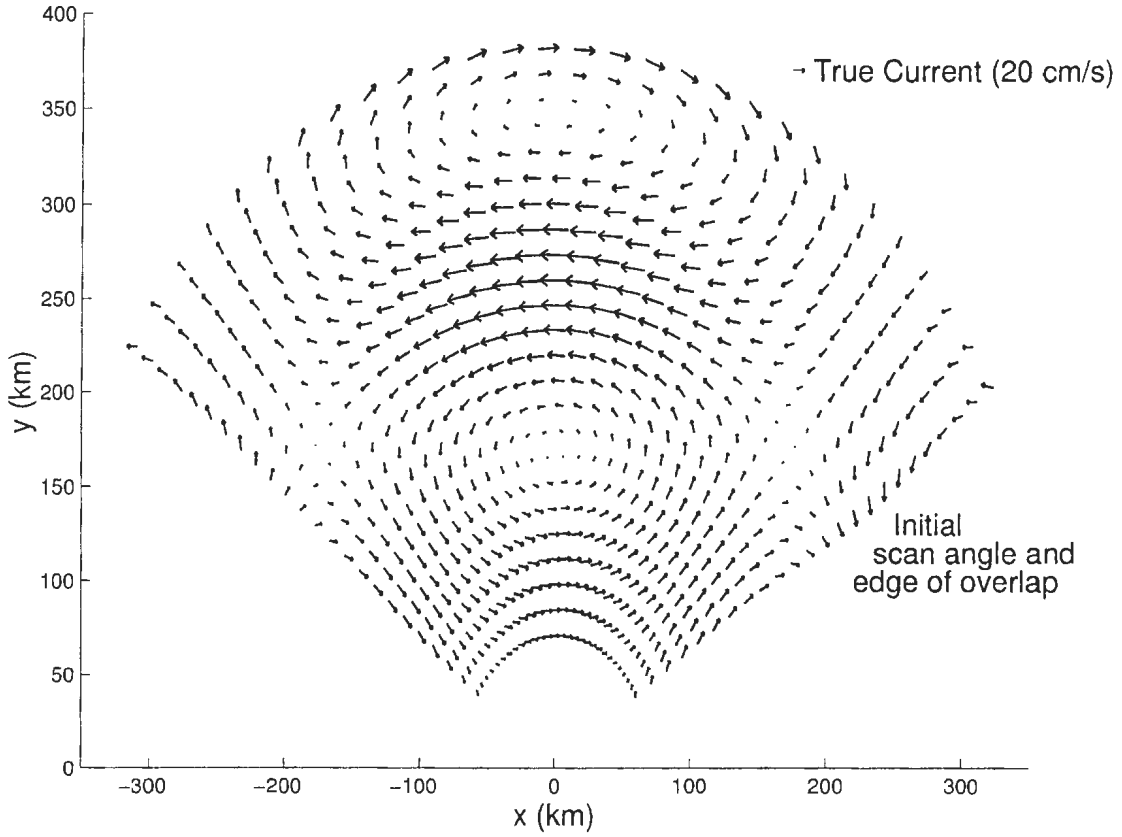

Figure 3.10: Current map for the flow pattern indicated by equations (3.32) and (3.33) with $a = 0.2$.

3.9 Continuity Technique Simulation Results

Simulations were carried out for all current magnitudes and directions. The results for all values of current magnitude will be examined in detail. Real data from the Grand Banks off the coast of Newfoundland are available to verify the continuity approach and will be discussed in Chapter 4.

3.9.1 Predictions

Based on knowledge of the technique, several predictions can be made regarding the quality of the results.

- Due to (3.22) current predictions at higher ranges will be less accurate.
- Tangential current estimates will worsen further from the overlap due to the compounding effect of using past estimates to obtain future values as discussed in Section 3.7.2.
- Current estimates will be better when the the current direction is more closely aligned with the radar look direction at the overlap since radial currents used in (3.22) will be bigger and less affected by FFT errors.
- Performance of the method will improve at higher current levels since larger currents will be relatively less sensitive to FFT errors.
- When the variable current is used it is expected that results will not be as good as for the case of uniform currents.

3.9.2 Results

To facilitate analysis of the results, the radar's range has been split up into 5 adjacent blocks each of which contains 15 of the averaged range cells. Figure 3.11 illustrates how the coverage area is partitioned to facilitate the analysis. The distances provided in the diagram are the ranges to the centres of the range cells to be included. The RMS error in magnitude and direction were calculated for each block. Other plots are provided that highlight the degradation in results with increasing range and increasing distance from the overlap edge.

Some of the trends that apply to all uniform current simulations are that the technique works best when operating with strong currents closer to the original overlap and at shorter ranges as predicted in Section 3.9.1. As the currents being used shift to directions less aligned with the initial radar scan angle, the errors in direction are lowest, but the errors in magnitude are greatest. This follows naturally from

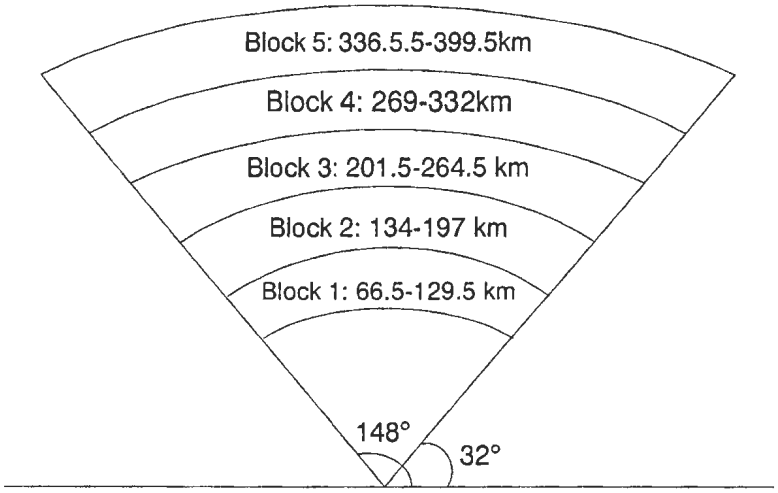

Figure 3.11: Simulation results are grouped and analyzed on the basis of range.

the tangential component representing a larger portion of the magnitude of the total current.

The results of the simulations will be judged based on the number of cells that the overlap can be extented. While using uniform currents, for a cell to be considered to be a valid extension the average of the worst case RMS error must be within

$$\Delta v_{RMS} < 30\%$$
$$\Delta \phi_{RMS} < 30^\circ \tag{3.34}$$

where Δv_{RMS} and $\Delta \phi_{RMS}$ are the RMS errors in magnitude and direction. When accepting extension cells using the variable current the average of the worst case error must conform to

$$\Delta v_{RMS} < 0.3a$$
$$\Delta \phi_{RMS} < 30^\circ \tag{3.35}$$

The first column in Tables 3.1 and 3.2 is the classification of the simulation based on the current direction with respect to the initial radar scan angle. The column

entitled "Comments" indicate up to what range, in terms of the blocks illustrated in Figure 3.11, the extrapolations are valid and state whether it was the magnitude or direction criteria of (3.34) or (3.35) that resulted in failure of the algorithm. Also, no further comparisons in more distant extension cells are made after the first point at which the criteria of (3.34) or (3.35) are violated. It is noted that failure of the technique always begins at remote ranges. At nearer distances, calculations of the vector current may still be valid. If the two site vector currents at the edge of the overlap had errors exceeding the limits imposed by (3.34) or (3.35) for a certain range block, that range block was excluded from the analysis.

Uniform Currents

The values in Table 3.1 show the effect that current magnitude and direction and distance to scattering patch have on the utility of the continuity technique. Use of the continuity equation is most reliable when the current magnitude is high and the vector current at the edge of the overlap has a strong radial component. The improvement in the estimates, for all current directions, as the current magnitude increases is apparent. However, on the open ocean the current strength and heading will be unknown and so the quality of the data at angles of 90° must be taken as the limit of the application of the technique.

A typical current map of worst case values is provided in Figure 3.12. Only every third cell in range is plotted to avoid cluttering the plot. The full range of radar coverage is not shown so as to highlight the region closest to the overlap. Figures 3.13 and 3.14 depict how the magnitude and direction of the current and the distance to the patch influence the quality of the estimates in the second extension cell. Figures 3.15 and 3.16 illustrate how the technique is affected by the magnitude and direction of the current and by the distance from the overlap for range cells in block 3. As

Table 3.1: Summary of results of using the continuity equation with uniform currents

Current Mag. (cm/s)	Current Dir. (°)	Cells of Extension	Comments
20	0	1	extension to fourth block, failure by dir.
	30	1	extension to fourth block, failure by mag.
	60	1	extension to first block, failure by mag.
	90	0	failure by mag.
50	0	4	final extension to fourth block, failure by mag.
	30	5	final extension to fourth block, failure by dir.
	60	2	final extension to third block, failure by mag.
	90	3	final extension to third block, failure by mag.
80	0	8	final extension to fourth block, failure by mag.
	30	11	final extension to fourth block, failure by dir.
	60	5	final extension to fourth block, failure by mag.
	90	3	final extension to fourth block, failure by mag.

usual, the angles identifying the subplots in each of these four figures refers to the current direction with respect to the initial scan angle. When strong currents are used for the simulations, the absolute error in magnitude may be high, but the percentage error is smaller than for the weaker currents. All four figures confirm the results of Table 3.1.

Variable Currents

The data in Table 3.2 summarizes the simulation results when the continuity equation is applied to variable currents. The data indicates that the algorithm works best when applied to strong currents, but this effect is not as pronounced as when uniform currents are used. Analysis of the RMS error reveals that, as expected, extrapolations will be more accurate if the vector currents at the edge of the overlap are more

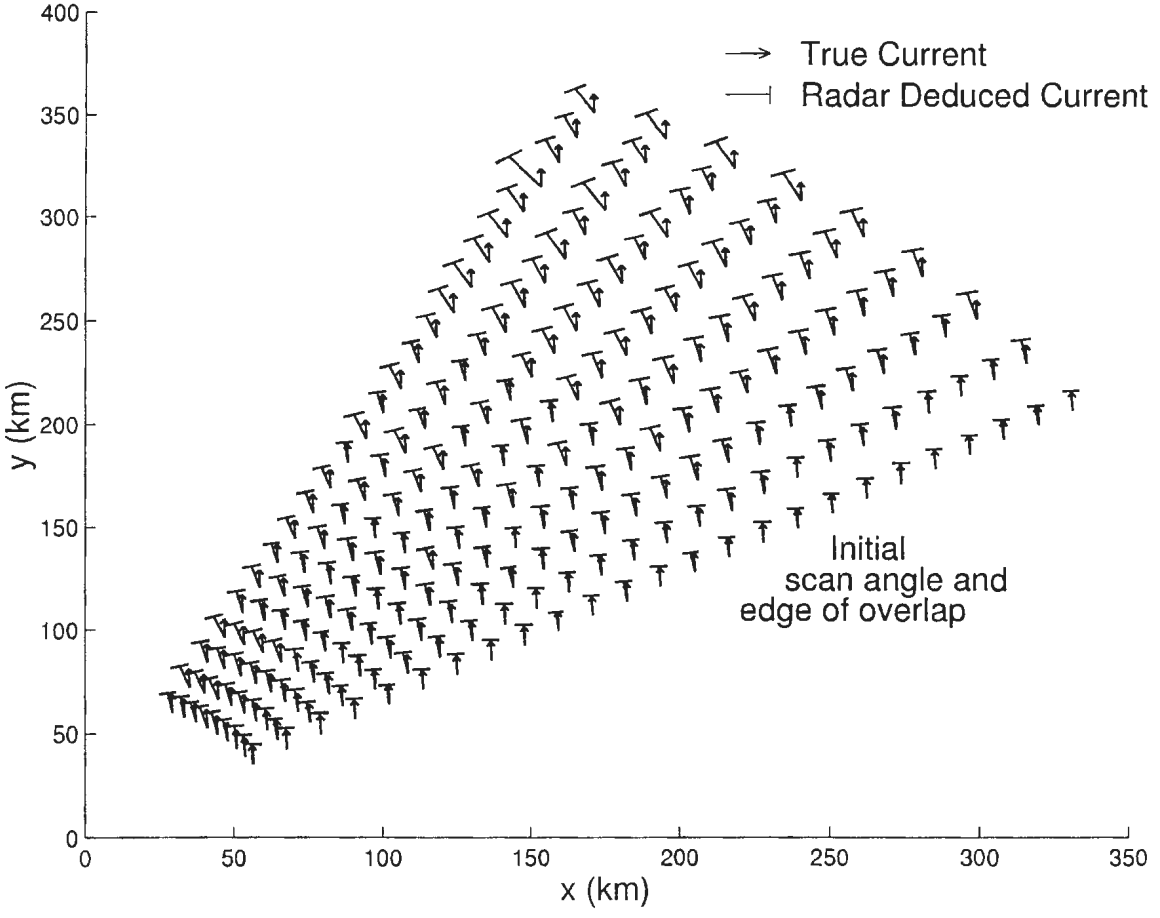

Figure 3.12: Current map of simulation of continuity when current has magnitude 50 cm/s and directed 60° from the initial radar look direction.

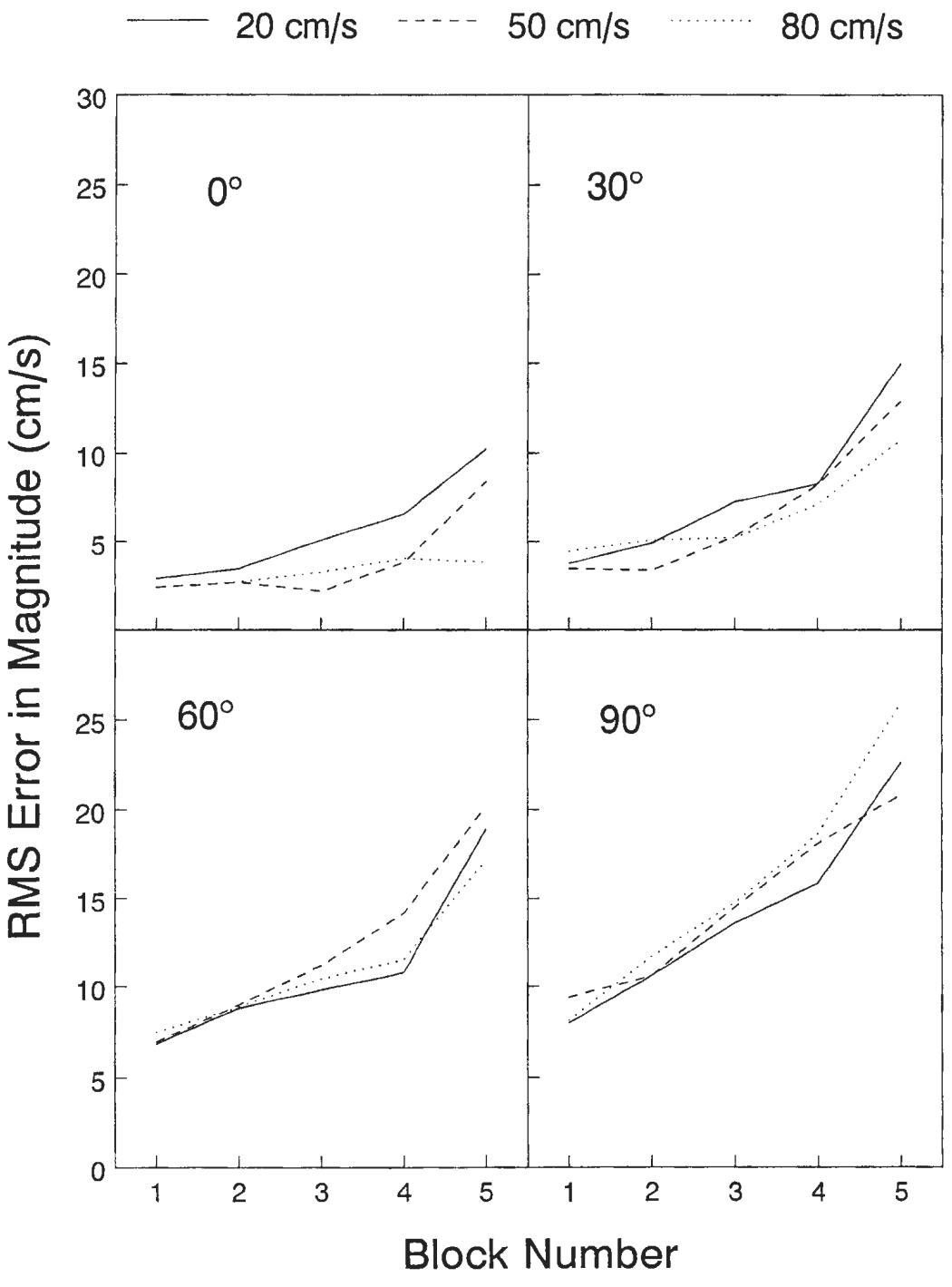

Figure 3.13: Error in current magnitude examined as current magnitude and direction and distance to the patch change for the second extension cell using uniform currents.

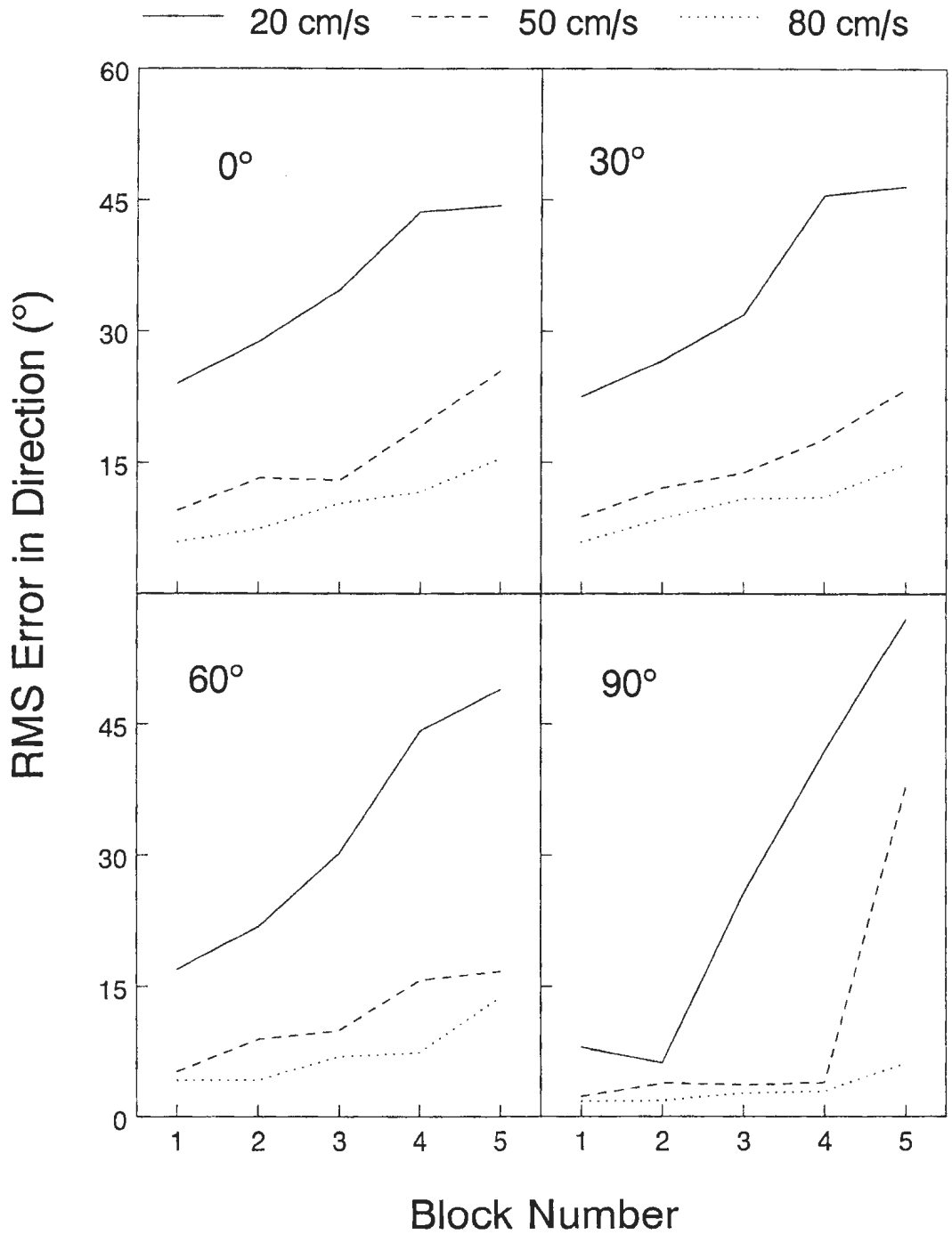

Figure 3.14: Error in current direction examined as current magnitude and direction and distance to the patch change for the second extension cell using uniform currents.

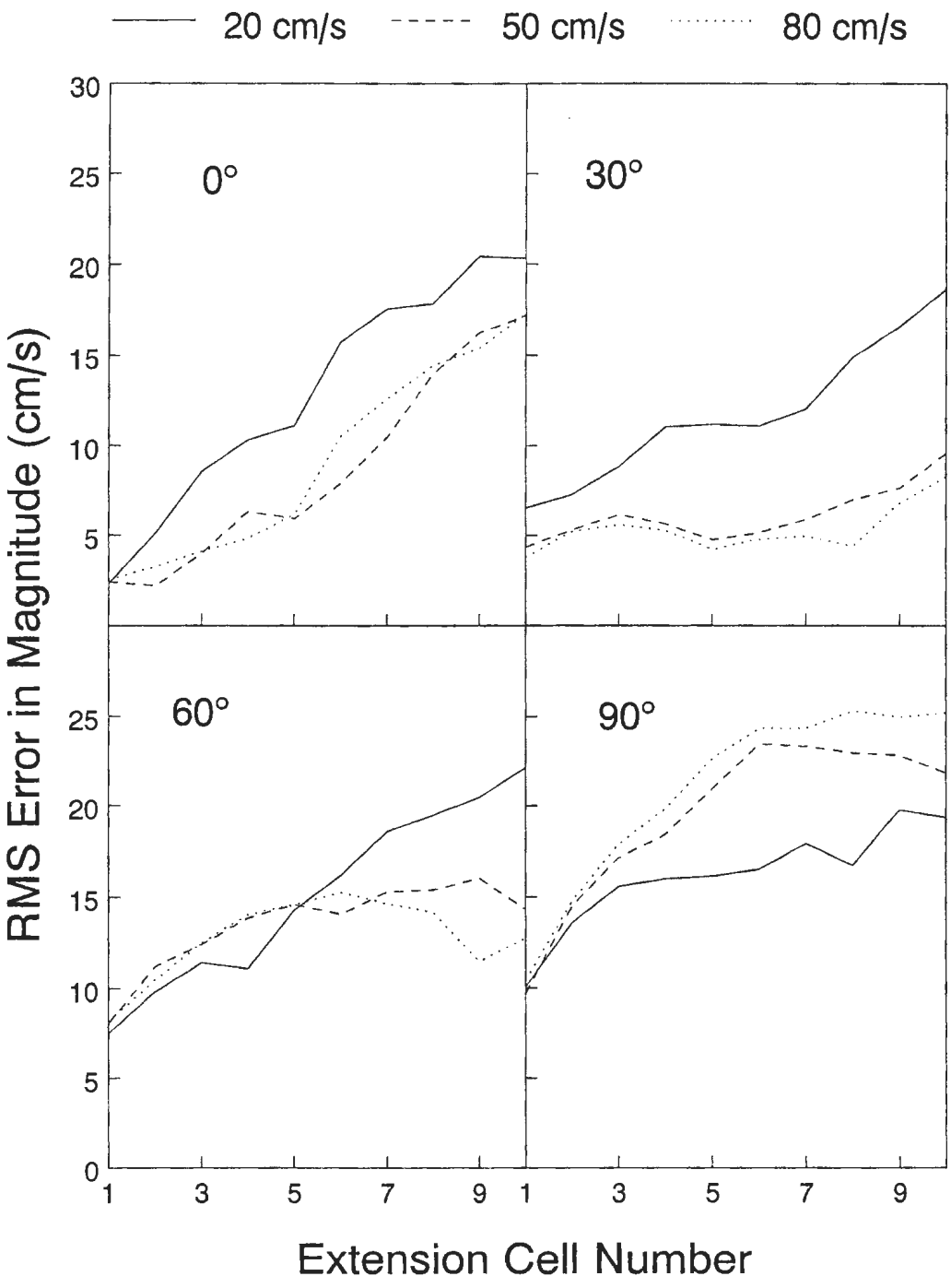

Figure 3.15: Error in current magnitude examined as current magnitude and direction and distance from the overlap change for the third range block using uniform currents.

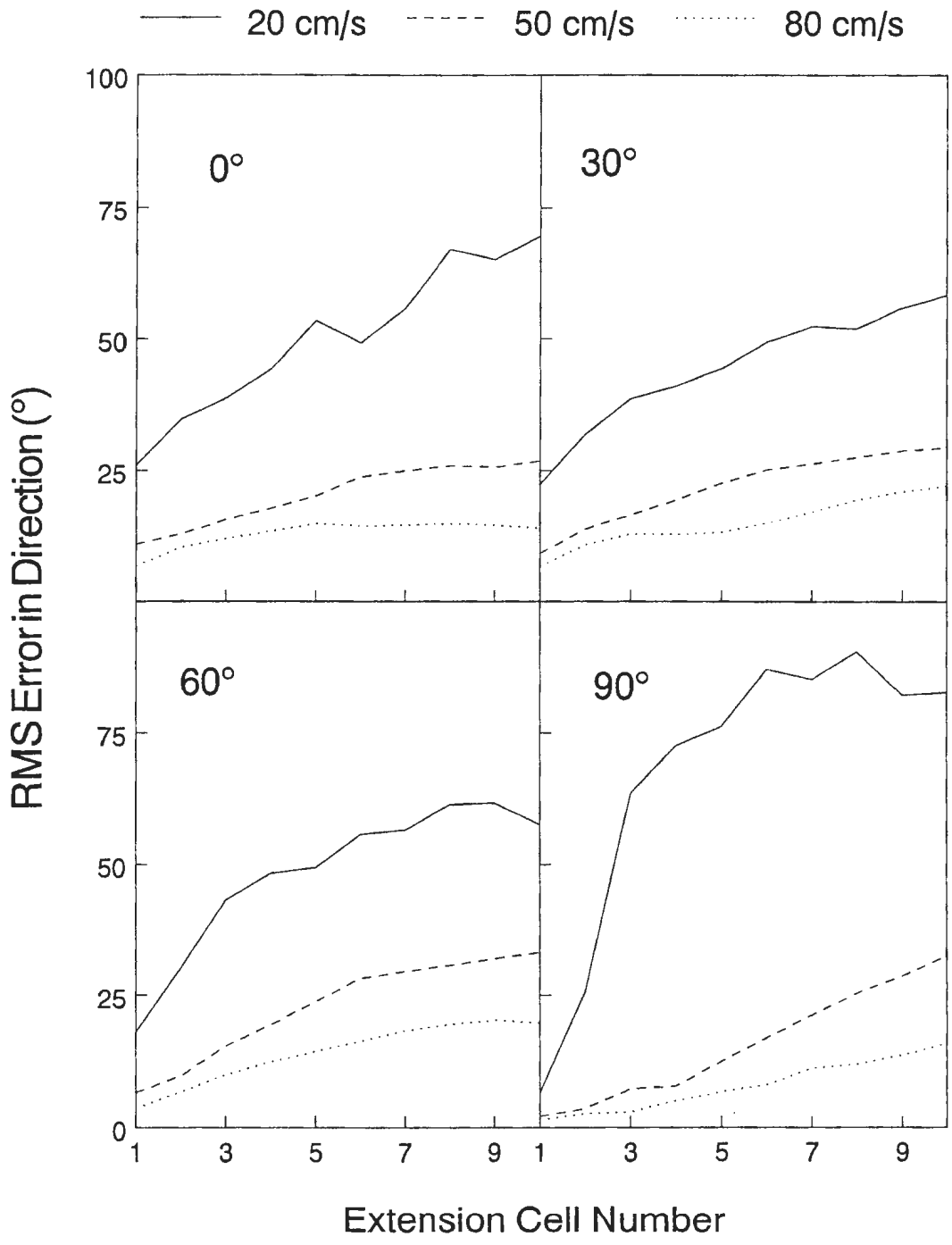

Figure 3.16: Error in current direction examined as current magnitude and direction and distance from the overlap change for the third range block using uniform currents.

accurate. This intuitive result was the reason the Cartesian and Cylindrical two-site methods were discussed in detail in Sections 3.1 to 3.4.

Table 3.2: Summary of results of using continuity equation with variable currents

Current Scaling	Cells of Extension	Comments
a = 0.2	1	extension to second block, failure by dir.
a = 0.4	3	extension to second block, failure by dir.
a = 0.6	3	extension to fourth block, failure by dir.

Figure 3.17 shows a truncated, typical worst case current map when the scaling factor is $a = 0.4$. Again, only the values for every third cell in range are plotted in the interests of space.

Figure 3.18 shows how the magnitude and direction of the current and the distance to the patch influence the quality of the estimates in the second extension cell. Figure 3.19 demonstrates how the technique is affected by the magnitude and direction of the current and by the distance from the overlap for range cells in block 3. The results using the technique may appear to improve as the distance from the overlap increases. However, the algorithm has no way to recover from inaccurate estimates and any improvement as the number of iterations increases is due to chance.

Conclusions

For uniform currents it is clear that performance of the continuity technique is best when the current has a large radial component at the angle where the vector currents are given and when the overall current strength is high. However, the continuity technique did show success for all uniform currents tested, except for currents of magnitude 20 cm/s directed perpendicular to the initial radar scan angle. The limited ability of the method using variable currents could be due to the current field chosen.

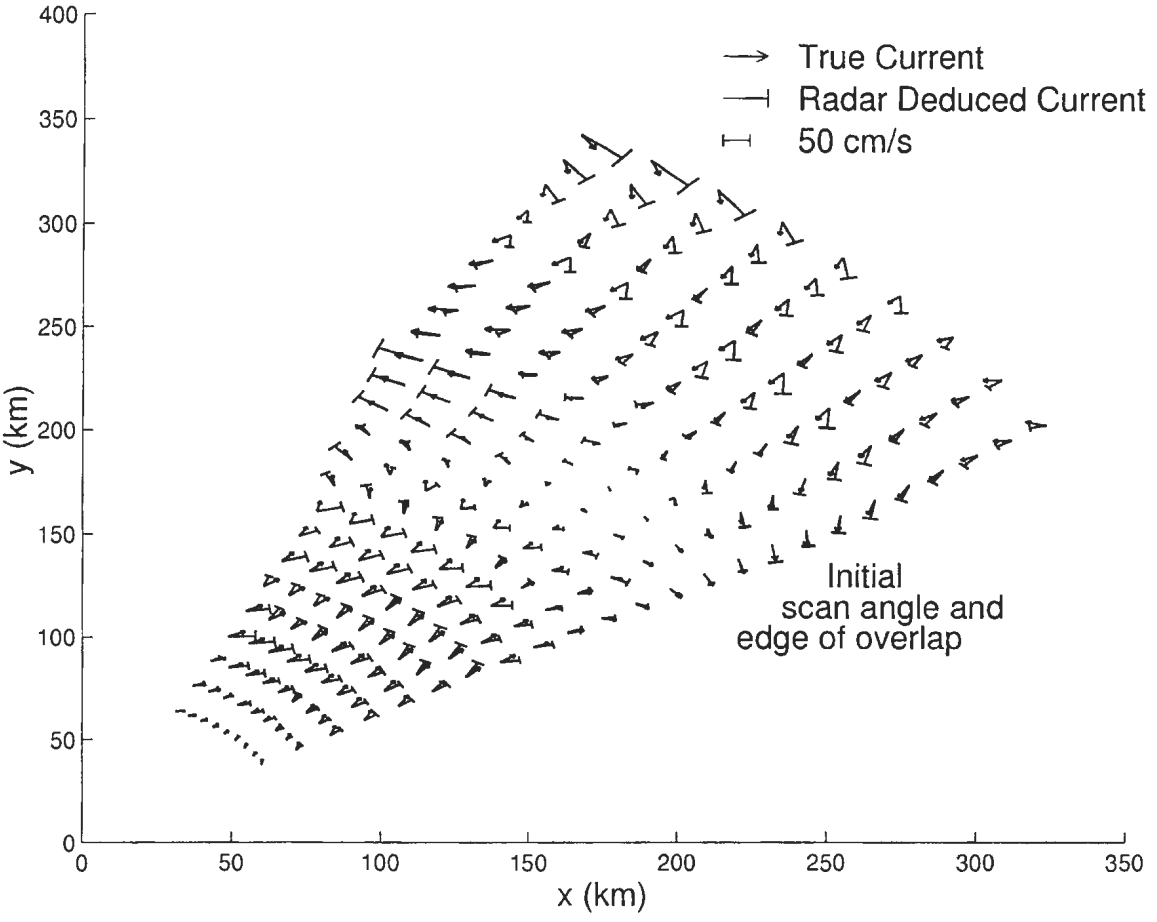

Figure 3.17: Current map of simulation of continuity with variable current pattern and $a = 0.4$.

Although the flow pattern was given realistic spatial variation, the specific form chosen may not have been conducive to the continuity approach.

When using uniform currents, all radial currents at a given azimuth will be the same except for the random error term. Thus, averaging across three range cells in range is almost guaranteed to reduce the radial errors and make the situation look slightly better than would be expected from real data. With nonuniform currents, the three cells averaged across range will have distinct values so the effect of averaging more closely models the case when real data are used.

In the following chapter radar data obtained during tests conducted in the summer and fall of 2002 will be used to ascertain the extent of the usefulness of the continuity

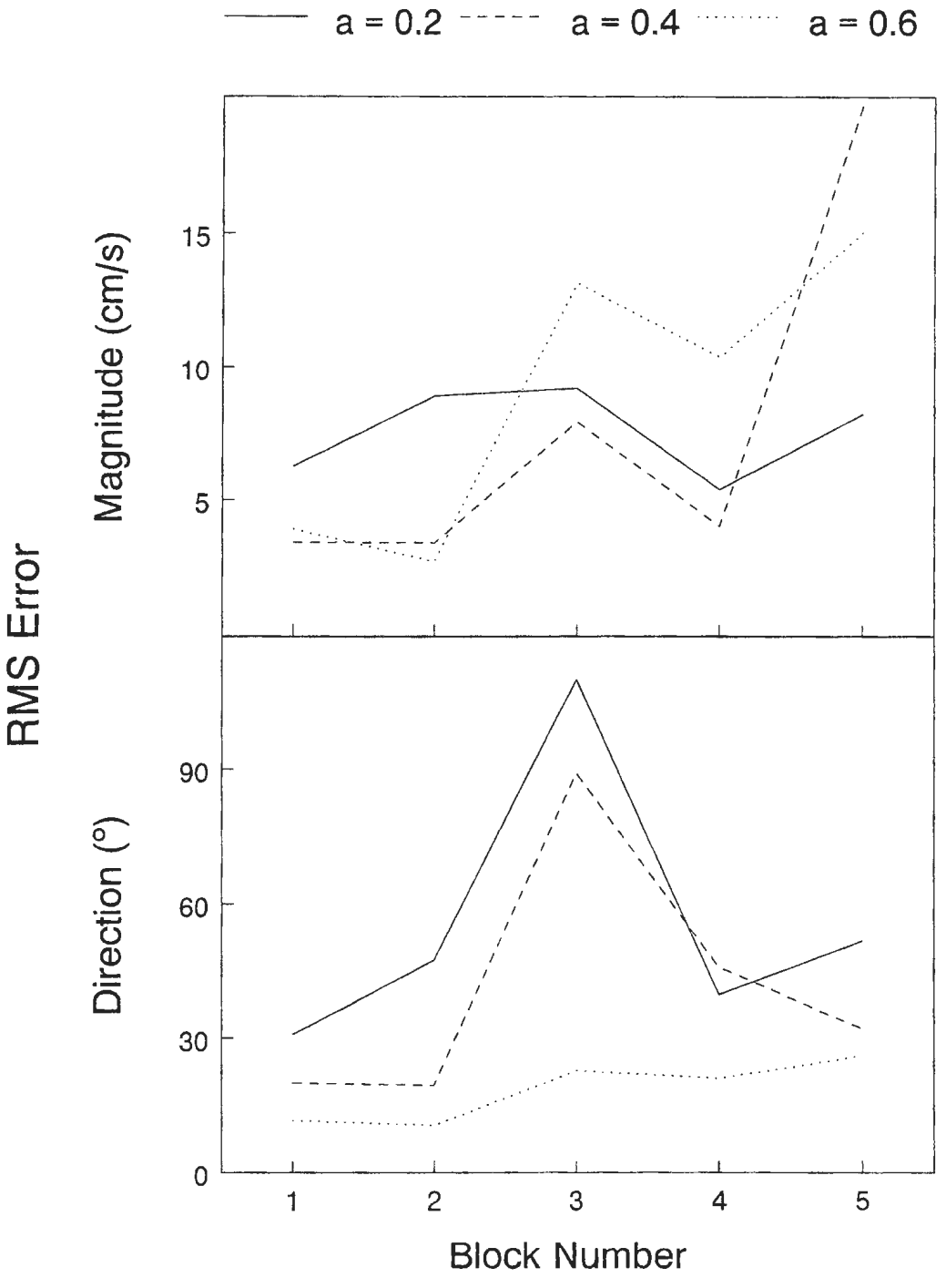

Figure 3.18: Error in current magnitude and direction examined as current scaling and distance to the patch change for the second extension cell for the variable current.

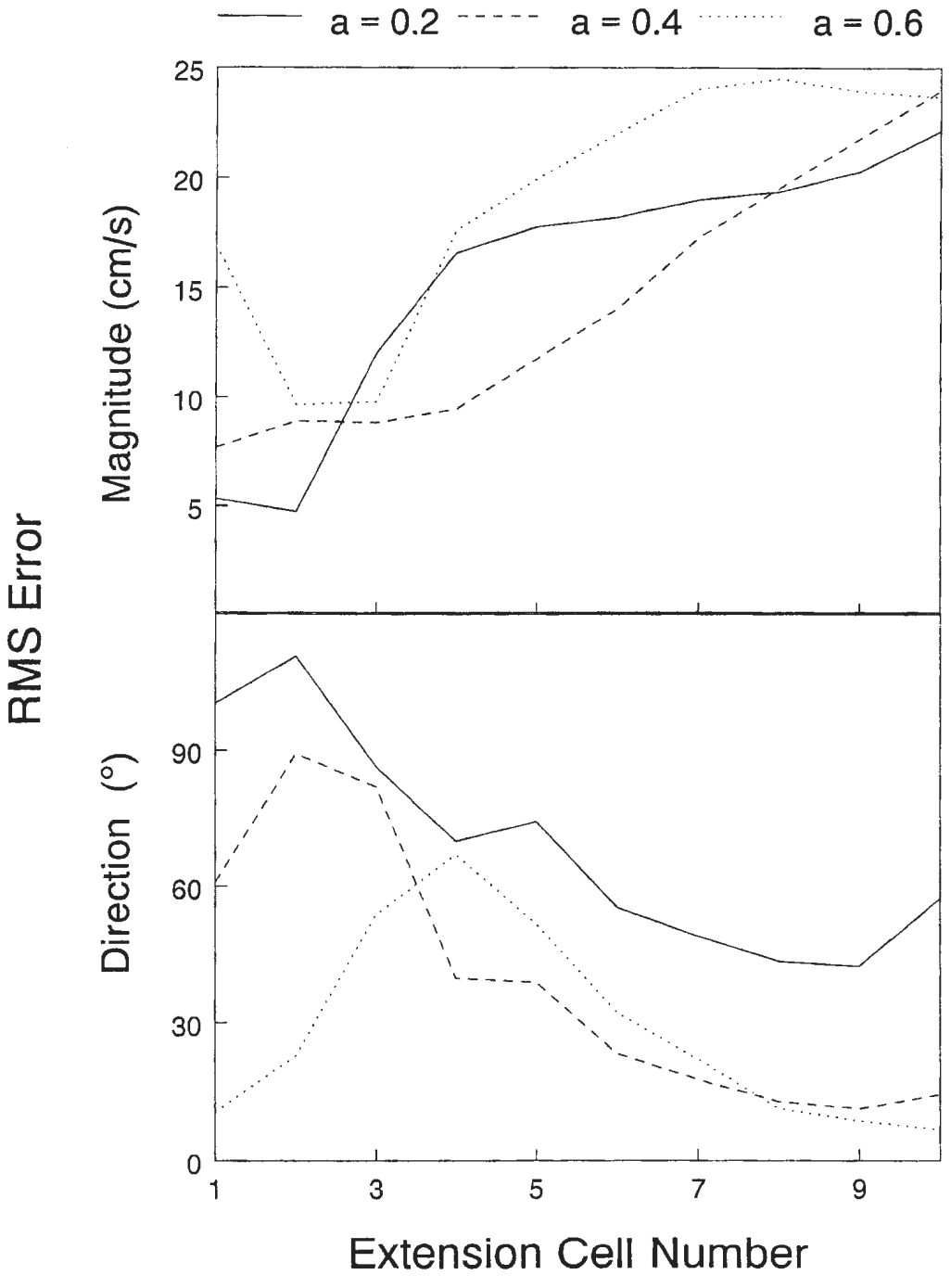

Figure 3.19: Error in current magnitude and direction examined as current scaling and distance from the overlap change for the third range block for the variable current.

technique. One of the challenges when working with real data is that there is no control over the current magnitude, direction or variability. For this reason, uniform currents of several magnitudes and directions as well as varying currents were chosen for the simulations. By analyzing the response of the continuity technique to several situations, its reaction to the real data will be more predictable.

Chapter 4

Experimental Data

4.1 Background

The use of HFSWR (high-frequency surface-wave radar) to measure surface currents is well established [3], [4], [19]. Two such systems are located at Cape Race and Cape Bonavista on the east coast of Newfoundland overlooking the Grand Banks. The radar facilities are operated by Northern Radar Inc. and are used for military target detection, iceberg tracking, and surface current measurement. New software has been designed and is now being used. To verify that the software yields correct values for the surface currents, tests were conducted in the fall and summer of 2002.

Radar data was collected on an almost hourly basis starting on July 30, 2002. To validate the radar data, drifters were deployed in the region of overlap between the two radars. C-CORE, a local company, was responsible for drifter deployment and data collection. The buoys used were Davis Drifters produced by Metocean of Dartmouth, Nova Scotia. Tracking was achieved via the ARGOS satellite system and an onboard GPS that transmitted position and time every half hour back to C-CORE via an LUT (local user terminal). The drifters are useful for measuring surface currents to a depth of 1 m. The Cape Race system operated at a frequency of 3.2

MHz and Cape Bonavista at 3.45 MHz. At these frequencies the radar measures an average current over a depth of approximately 4 m [21]. Thus, the radar and drifters sample nearly the same region of ocean.

There is a difference in the nature of radar and drifter measurements. Drifters follow the water motion; a current vector is derived by determining the float's position at some initial and final time and finding the average velocity over the elapsed time. This type of measurement is Lagrangian. Eulerian methods find the current at a fixed point at a given time. For the case of HF radar the fixed point is the average over the range cell and the specific time is the start time of the radar interrogation. In theory, the information that the radar and drifters yield are equivalent; in practice it has been found that differences exist that make each method better for different applications [47] and there will be inconsistencies when comparing radar and drifter-derived values. However, drifters have a proven ability to validate radar-derived currents (see, for example, [3] and [31]), but will not be used to confirm the results of the continuity technique. However, a typical plot to ground truth the radial currents deduced from each radar is given in Section 4.5.

The purpose of this chapter is not to verify the usefulness of radar to measure surface currents, but to determine the utility of the continuity equation to extrapolate for the solution of vector currents to beyond the overlap region.

The continuity equation will be used in comparing the extrapolated values to the radar vector currents as determined by the two-site Cartesian method. The algorithm will begin at an angle where vector currents are known and, instead of moving into a region of single site coverage, the solution will be carried further into the overlap so that comparisons can be made with the two-site vector currents.

4.2 Current Determination

The actual radial current values for each range cell as measured by the radar, rather than the Doppler spectra themselves, were made available by Northern Radar. The radial current, which is based on the frequency shift imposed by the water motion, can be found by detection of the Bragg peaks. The process that was followed to extract the current information from the backscattered radar return is explained by Hickey [6] and must be done for every range cell.

1. In order to isolate the frequency components of greatest strength, a 150 cm/s window was placed around the Bragg frequencies of $\pm f_B$. Since currents on the Grand Banks of Newfoundland are typically weak [48] the window, known as the signal window, will contain any Bragg peaks that are present. For the Cape Race and Cape Bonavista systems operating at 3.2 and 3.45 MHz the signal window will be ± 0.032 Hz and ± 0.0345 Hz, respectively.

2. The average power in the range $0.5 < |f_D| < 1.0$ Hz, where f_D is the the Doppler frequency in Hz, is calculated as the noise floor. Since there are potentially two Bragg peaks with different signal levels, there will be separate signal to noise ratios (SNR) for each side of the spectrum.

3. Current calculation is based on the side of the spectrum that has the stronger SNR provided that the SNR is above 10 dB. If the SNR for the stronger Bragg peak is below 10 dB, no current calculation is made.

4. The central peak frequency is found by weighting the frequency components in the signal window with the SNR values and doing a moment calculation. Each point included in the calculation was required to have a minimum SNR of 10 dB.

The precise determination of the currents will be limited by the resolution of the FFT. For both radar systems the FFT resolution is 0.0019 Hz. Using equations (1.5) and (3.4), and recognizing that $\Delta F_s = \pm\frac{0.0019}{2}$Hz, the current resolution is found to be $\pm$4.45 cm/s for Cape Race and $\pm$4.13 cm/s for Cape Bonavista.

In Chapter 3, it was shown that calculating the two-site vector currents using the Cartesian method of equation (3.1) gave reliable values regardless of range or azimuth. This equation will be applied to the radar data and will allow the continuity equation to be applied at any scan angle and range of either the Cape Race or Cape Bonavista facility.

4.3 Radar Data Selection

The verification tests yielded thousands of radar data files. In addition to the individual radial files for Cape Race and Cape Bonavista, a vector current file was provided whenever there were radial files from each site at approximately the same time. The vector currents were average values over an area of approximately 20 km $\times$ 20 km. In order to find the value of the vector current at a certain point, interpolation using four adjacent blocks is used. While these pre-calculated vector currents could not be used for verifying the continuity technique, the number of blocks in a file with valid vector values gave an indication of the quality of the individual radial current files from both radar sites up to distant ranges. The only radial current files that were selected for processing were those containing over 120 vector current blocks in the corresponding vector current file.

Once a file was selected for processing via the continuity technique, for a given range the edge of the overlap was considered to begin at at any scan angle for which two-site vector currents were available for three azimuthally adjacent cells. Although the technique can be tested against radar data whenever there are two azimuthally

adjacent cells, data will only be presented if there are a minimum of three such cells so that extrapolations can be carried out across two extension cells.

It can be expected, as discussed in Section 3.9, that the extrapolations will be more accurate when the current magnitude is higher and more closely aligned with the angle at which vector currents are known and when the current has less spatial variability. These situations are not singled out for inclusion in the data set. However, it is important to ensure that the data points being used are indeed valid measures of the vector current; FFT errors, the presence of targets at the Bragg speed, radar operation problems, and instabilities due to the geometry when calculating the vector current can all be potential contributors to errors in the recorded current values. To temper the effect of these factors, it has been required that azimuthally adjacent range cells have vector current magnitudes within 10 cm/s of each other and directios within 45° of each other. As well, radial currents used in the calculation of the partial derivative of equation (3.7) must each be within 10 cm/s of the radial value at the central cell. Water motion on the surface of the open-ocean is not likely to undergo large spatial variations within the resolutions discussed here. The value of 10 cm/s is used since it is just above twice the FFT radial error for each site and still allows for reasonable spatial variance.

Unfortunately, not all problems with the data can be avoided by the filtering of obviously corrupted data. Use of the FFT on the radar time series yields variability in the current values which is reduced by averaging. It can be expected that radial current radar data at adjacent ranges should have similar values but this is not always the case. When the fluctuations are beyond the standard FFT error, the continuity technique will not function properly. Figure 4.1 is a plot of the radial current values for one Cape Race data file at one scanning angle. Averaging across three range cells has been carried out and data with insufficient SNR have been discarded. The erratic

nature of the values cannot be attributed to specific causes and their exclusion of the data cannot be justified. Since the SNR for the questionable values of the radial current are quite high, it is unlikely that interference and noise are responsible for the error. Regardless of the source of the error, it cannot be neither predicted nor characterized. While such jumps may not occur in the actual overlap data, extreme radial values will affect the calculation of the partial derivative found in (3.7).

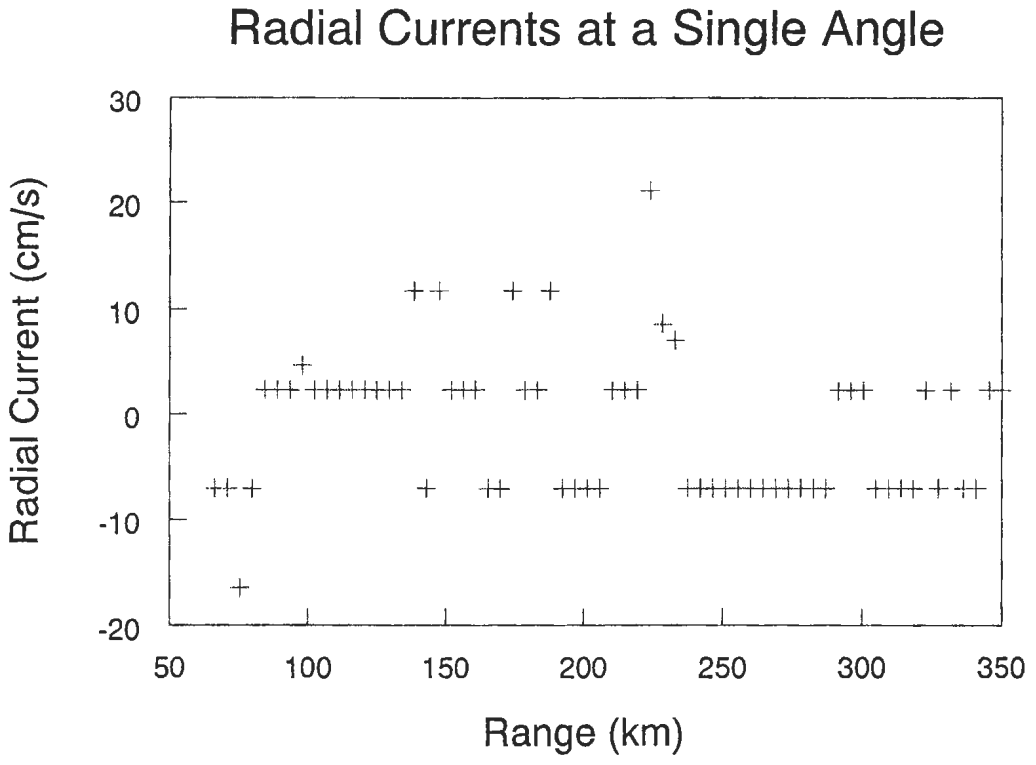

Figure 4.1: Radial current values from Cape Race on Sept. 17, 2002 at 1804 GMT.

4.4 Radar Data Filtering

Although the radar is a reliable tool for finding ocean surface currents, various operational problems necessitate the identification and removal of erroneous data. The length of the range cells for both radar sites is 1500 m and the nominal beamwidths are 3.338° and 2.867° for Cape Race and Cape Bonavista, respectively. From antenna

theory it is well known (see, for example [26]) that the beamwidth will be greater at the edges of the radar scan zone. Thus, current values at the edges may be less accurate and are not included for the analysis. Within the central portion of each radar scan zone, the data is sometimes intermittent due to poor signal to noise ratios, in which cases currents cannot be determined for all ranges and scan angles. Repair work and other research commitments were responsible for hours and days of absent data. Problems such as these sometimes resulted in missing data at all ranges for certain scan angles. In general, however, large quantities of data were available for analysis.

For this data set, there is no averaging performed across azimuth but up to nine adjacent range cells in range are averaged to find the radial current in each extended range cell of length 4500 m. The average and standard deviation of the nine radial values are found. A final average is calculated using those values that are within 1.5 standard deviations of the original average. The final average is retained only if at least three radial values are used. The averaging process is more complicated than that used for the simulation data to accomodate the large, unpredictable FFT errors discussed in 4.3 and to make the continuity approach more widely applicable by covering gaps in the data.

4.5 Radial Currents

For the purposes of comparison of radar and drifter data it is assumed that the radar current is what is known at the very centre of the range cell. To find the radar current at the exact location of the drifter, the radial currents in the four averaged range cells surrounding the drifter are used. Linear interpolation of the radar values are used to find the radar-derived current at the desired drifter point. If four valid radar values are not found surrounding the radar, no comparison is made.

Four drifters were deployed in the region of overlap for the Cape Race and Cape Bonavista radar sites. The drifters were tracked while in the overlap and until they left the single-site coverage area. Ground truthing for Cape Race using one of the drifters yielded a correlation of $r = 0.801$ on the basis of 24 comparisons. The RMS error between the drifter and radial values is 11.08 cm/s. A scatter plot of the Cape Race ground truthing is shown in Figure 4.2.

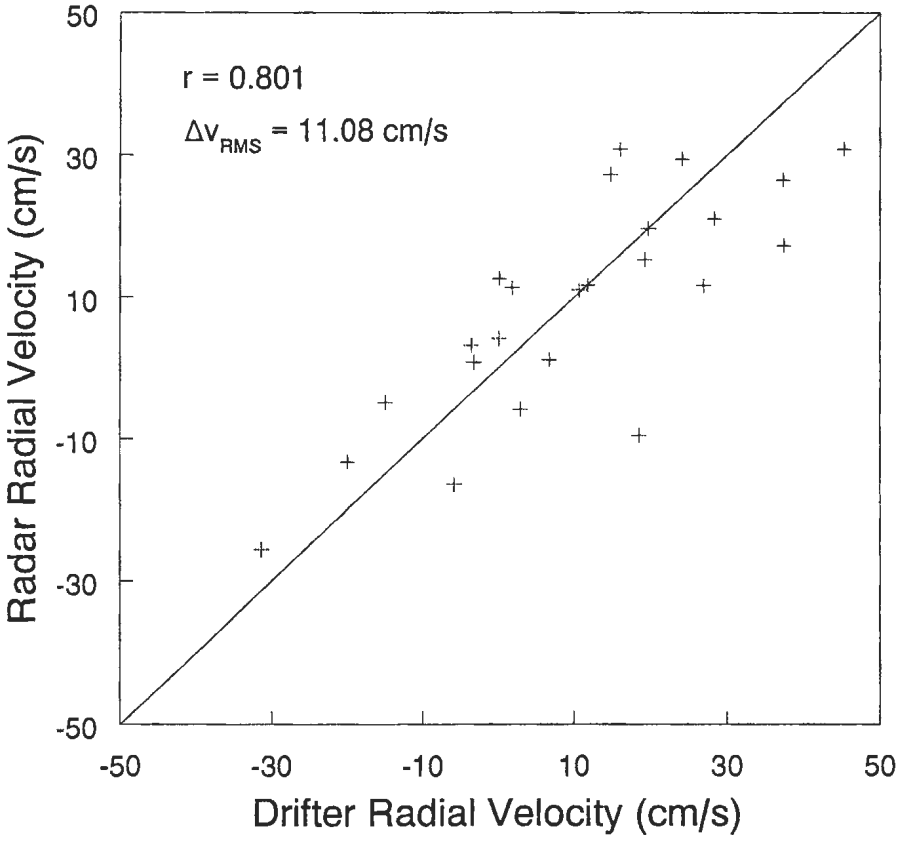

Figure 4.2: Comparison of radial current data as determined from the Cape Race radar and a single drifter.

Groundtruthing for the Cape Bonavista facility revealed a correlation of $r = 0.821$ based on 17 comparisons coming from multiple drifters. The RMS difference between the radar and drifter radial values is 8.47 cm/s. The scatter plot showing these results is given in Figure 4.3.

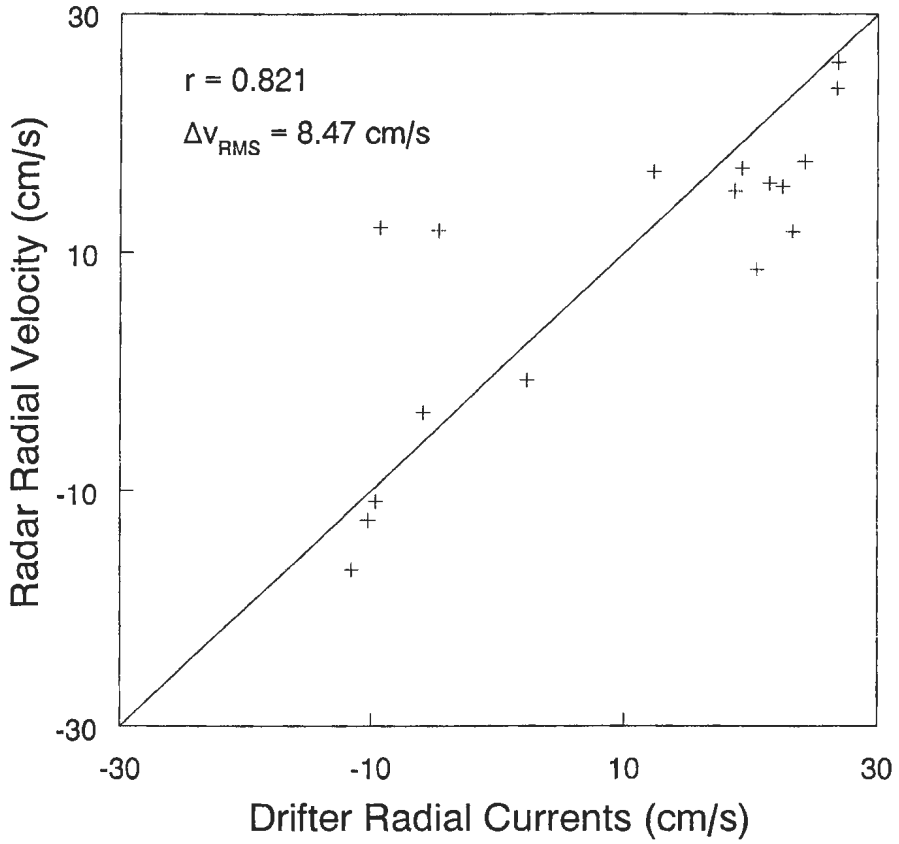

Figure 4.3: Comparison of radial current data as determined from the Cape Bonavista radar and drifters.

4.6 Radar-Radar Comparison - Continuity Technique

It has been shown in Section 4.5 that the correlation coefficient, r, for comparisons between radar and drifter values for each radar system is above 0.8 for the experiment being considered. Using the continuity technique, tangential current estimates can be made adjacent to the overlap provided that radial currents are known there and if the radial and tangential components of the current are known at the edge of the overlap. However, as can be seen from equation (3.7), the continuity equation can be solved starting anywhere vector currents are known provided radial current information is present in the region of extrapolation.

Thus, for the purposes of verifying the technique, the continuity equation will be solved within the overlap area itself and compared to the two-site Cartesian version of the vector current. By comparing the continuity technique with two-site radar data, the errors in comparing radar and drifter data are removed and the number of valid comparisons increases dramatically due to the volume of radar data available. However, no interpolating is necessary since radar cells will be tested against radar cells.

Section 3.7 states that the error due to the continuity approach will increase further away from the original cell where vector currents are known and that the effect of ignoring the vertical velocity gradient will increase with range. Calculation of the integral in equation (3.7) also results in a range dependent error as discussed in Section 3.7.2. Acknowledging these facts, the comparisons will be separated into different range categories and by number of extension cells from the overlap. The range groupings used are $200 < \rho < 250$ km, $250 < \rho < 300$ km, $300 < \rho < 350$ km and $\rho > 350$ km where ρ is the distance from the reference radar. For each range group, thirty data points will be found for extrapolations carried out for each of two cells beyond the overlap.

4.7 Discussion

Presentation of the results from examining real data will be broken up by range, number of cells from the edge of the overlap, and then in magnitude and direction.

As noted from the simulations discussed in Section 3.9, errors in the original overlap or early in the iteration process tend to propagate and increase as the extrapolations proceed.

The following pages contain scatter plots of the magnitude and direction of the current as calculated via continuity and plotted against the Cartesian two-site method.

The correlation coefficient, r, between the two data sets is provided along with the RMS error. Whenever there is a concentration of data points at similar current magnitudes and directions, the correlation coefficient will not be a good indicator of the quality of the technique.

4.7.1 Cape Race as Reference

The correlation coefficient, r, and the RMS error for the comparisons of vector currents, of magnitude v and heading ϕ, calculated using the Cartesian two-site method and the continuity equation are given in Tables 4.1 and 4.2, respectively.

Table 4.1: Correlation coefficients, r, for magnitude and direction when Cape Race is used as the reference

Range	1 Extension		2 Extensions	
(km)	r_{Mag}	r_{Dir}	r_{Mag}	r_{Dir}
200-250	0.382	0.768	0.242	0.788
250-300	0.342	0.915	0.034	0.799
300-350	0.466	0.959	0.081	0.855
>350	0.674	0.942	0.372	0.883

Table 4.2: RMS errors, Δv_{RMS} for magnitude, and $\Delta\phi_{\text{RMS}}$ for direction, when Cape Race is used as the reference

Range	1 Extension		2 Extensions	
(km)	Δv_{RMS} (cm/s)	$\Delta\phi_{\text{RMS}}$ (°)	Δv_{RMS}(cm/s)	$\Delta\phi_{\text{RMS}}$ (°)
200-250	4.27	24.12	7.73	56.36
250-300	6.51	37.55	10.06	61.36
300-350	7.04	32.10	11.82	59.78
>350	7.88	43.30	17.25	60.98

Examination of the scatter plots in Figures 4.4, 4.5, 4.6, and 4.7 shows that the magnitude values are not always distributed evenly, resulting in certain cases with poor correlation coefficients as seen in Table 4.1. For such data sets, low correlation is not indicative of the inaccuracy of the technique but reflects the relatively narrow distribution of the data. Analysis of the RMS error reveals that for all range categories the continuity technique is able to provide good estimates of current magnitude for the first extension cell and reasonable estimates for certain ranges for the second extension cell. The errors in current direction are moderate to fairly high even for the first extension cell and increase further for the second extension cell. The high correlation of direction values for both extension cells for is partially due to the broad distribution of data, not its accuracy, as is evidenced by the corresponding high RMS errors for the second extension cell.

As can be seen from the plots, in most cases there were a few outliers that had a large effect on the total error. The general increase in errors with range is due to the expected reduction in quality of the continuity equation with distance as discussed in Section 3.7.1. At very distant ranges, the increased error may be partially the result of the radar's reduced ability to make accurate measures of the surface current.

4.7.2 Cape Bonavista as Reference

The symbols for the correlation coefficient and RMS error are as for when Cape Race is used for the reference. Tables 4.3 and 4.4 show the correlation coefficients and RMS errors, respectively, for comparisons between the vector currents calculated using the Cartesian two-site method and the continuity equation.

Scatter plots for comparing the vector currents calculated using the Cartesian two-site method and the continuity technique are given in Figures 4.8, 4.9, 4.10, and 4.11. For the first extension cell it can be seen that the magnitude and values are

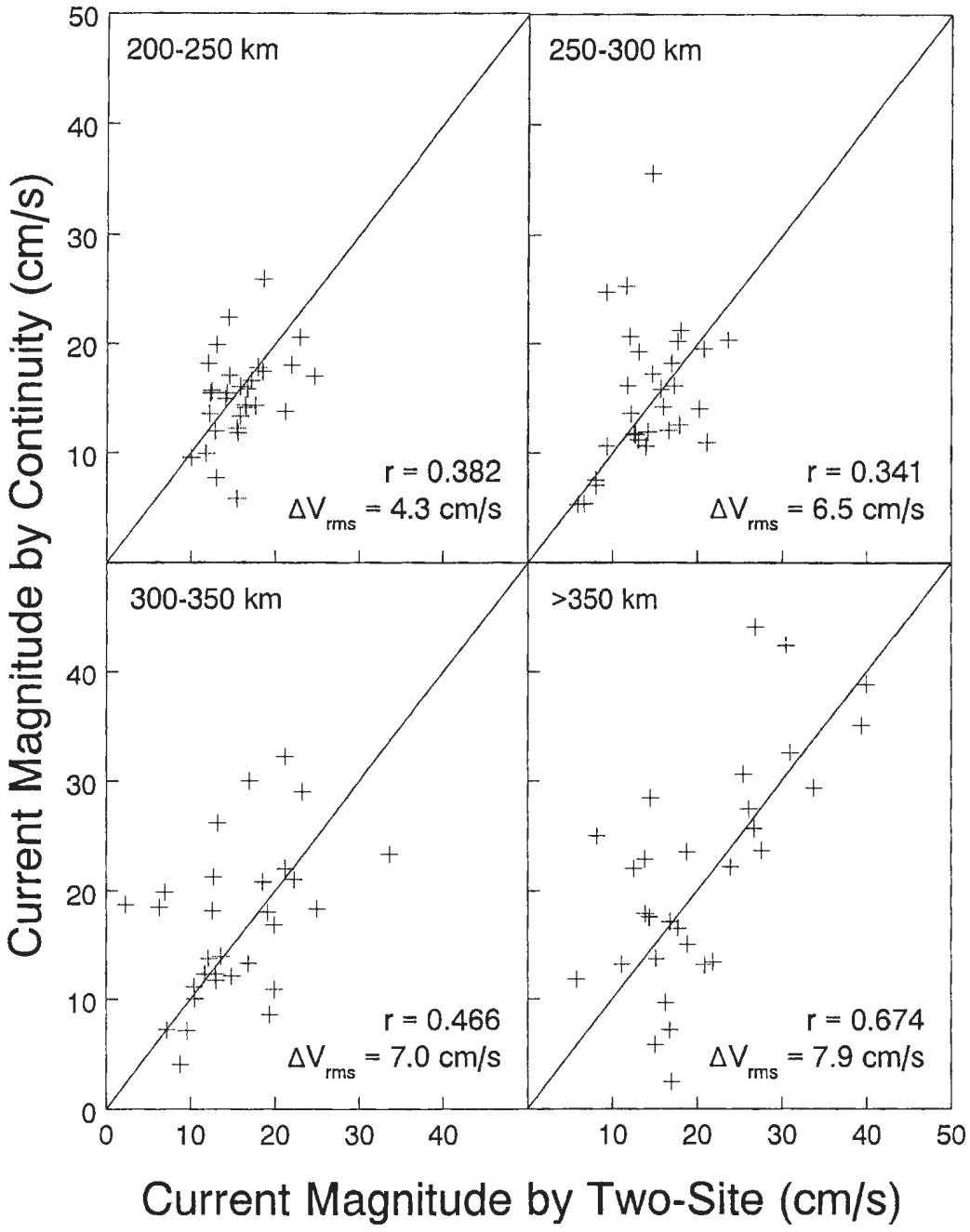

Figure 4.4: Scatter plots comparing current magnitudes as calculated by the Cartesian two-site method and the continuity equation for the first extension cell. Cape Race is the reference.

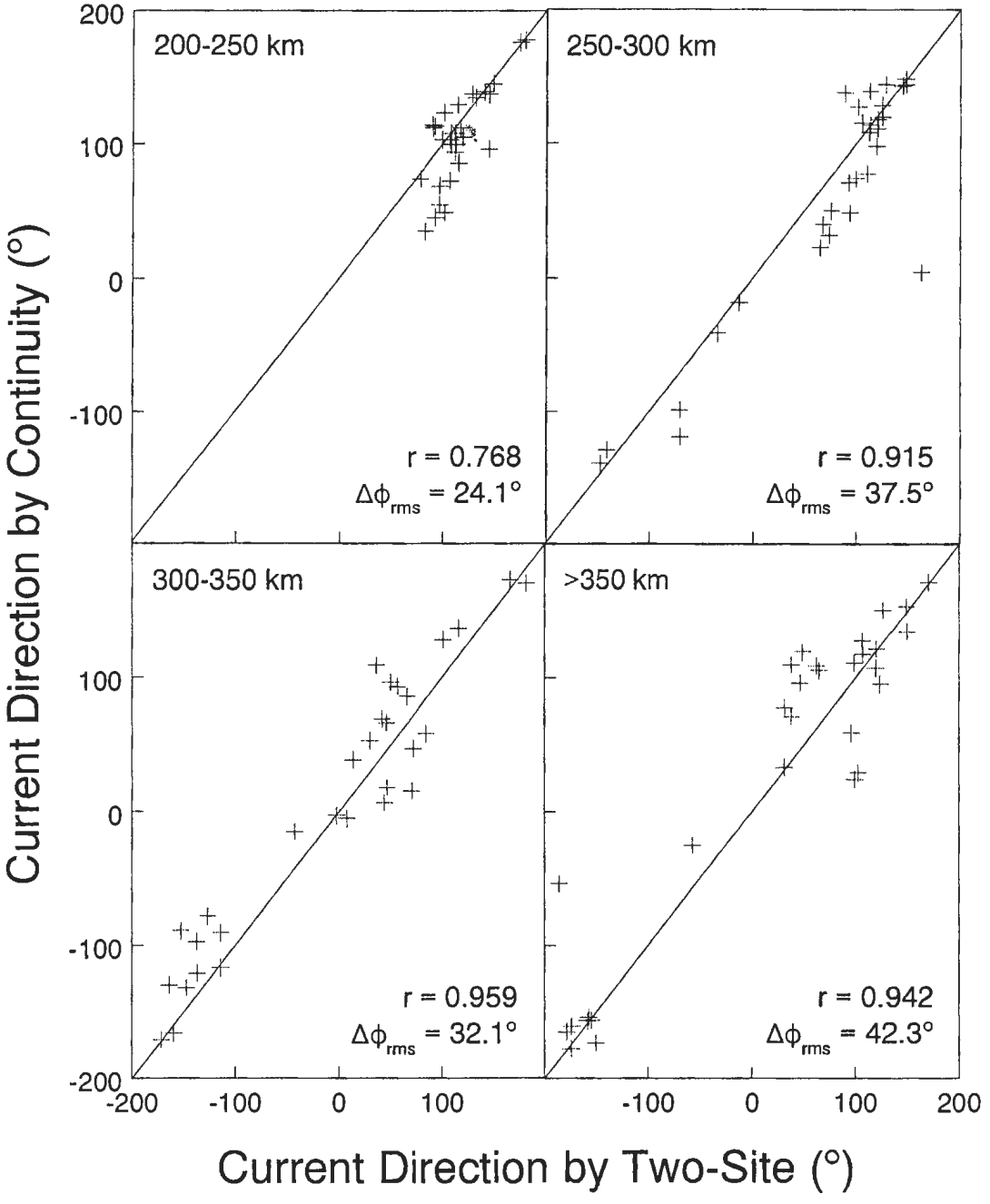

Figure 4.5: Scatter plots comparing current directions as calculated by the Cartesian two-site method and the continuity equation for the first extension cell. Cape Race is the reference.

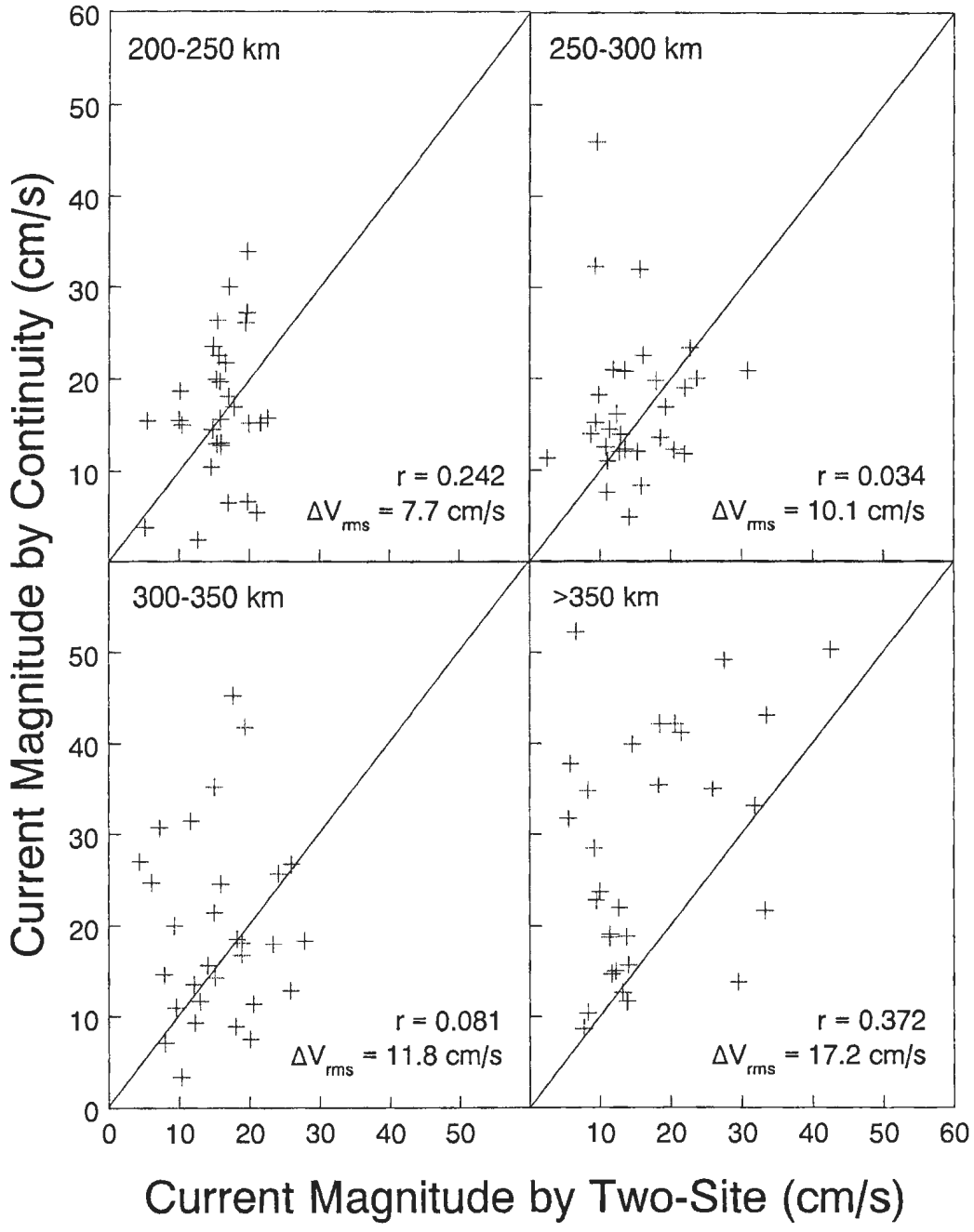

Figure 4.6: Scatter plots comparing current magnitudes as calculated by the Cartesian two-site method and the continuity equation for the second extension cell. Cape Race is the reference.

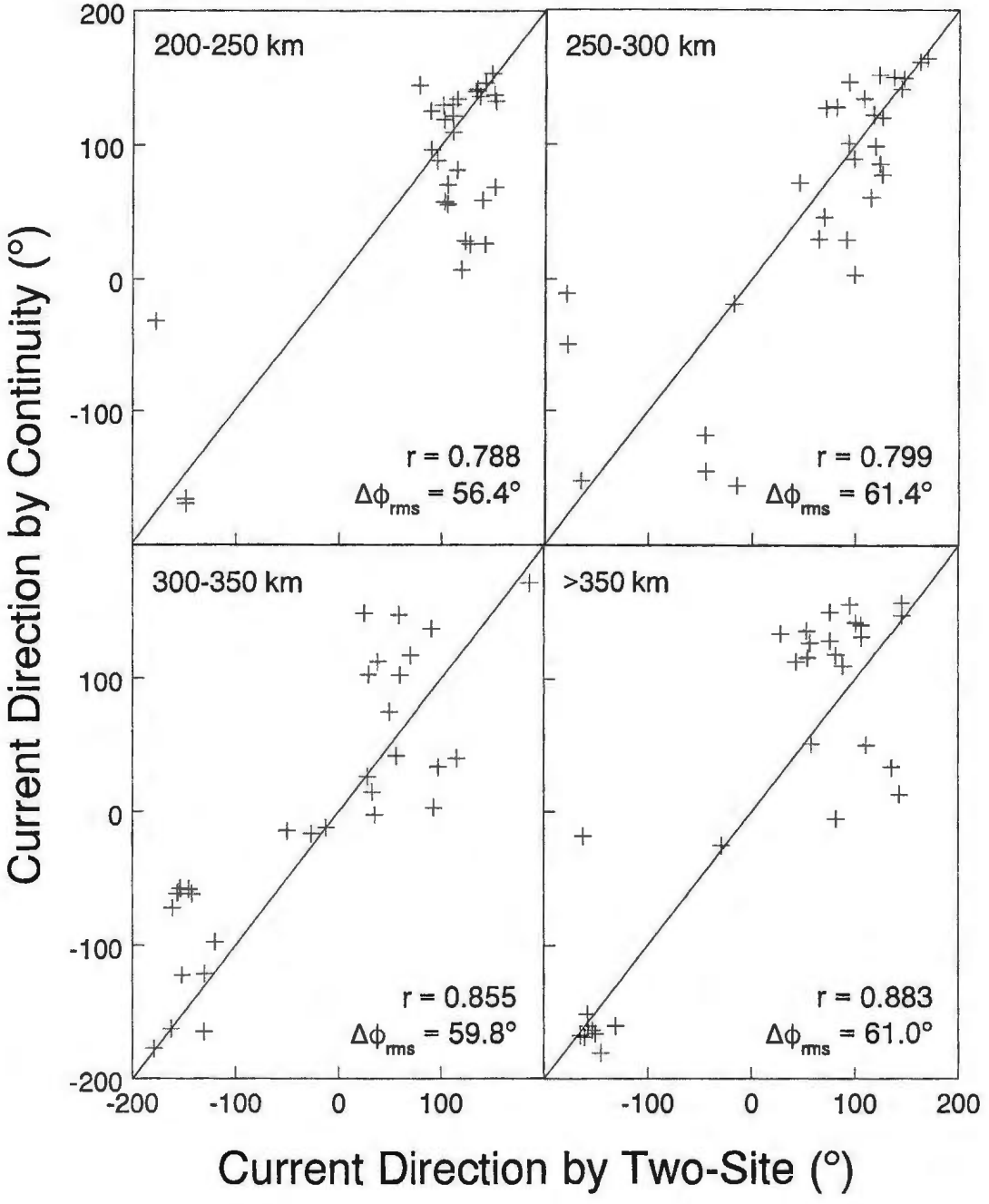

Figure 4.7: Scatter plots comparing current directions as calculated by the Cartesian two-site method and the continuity equation for the second extension cell. Cape Race is the reference.

Table 4.3: Correlation coefficients, r, for magnitude and direction when Cape Bonavista is used as the reference

Range	1 Extension		2 Extensions	
(km)	r_{Mag}	r_{Dir}	r_{Mag}	r_{Dir}
200-250	0.795	0.709	0.523	0.459
250-300	0.705	0.650	0.512	0.172
300-350	0.651	0.957	0.412	0.865
>350	0.614	0.887	0.544	0.785

Table 4.4: RMS errors, Δv_{RMS} for magnitude, and $\Delta\phi_{\text{RMS}}$ for direction, when Cape Bonavista is used as the reference

Range	1 Extension		2 Extensions	
(km)	Δv_{RMS} (cm/s)	$\Delta\phi_{\text{RMS}}$ (°)	Δv_{RMS}(cm/s)	$\Delta\phi_{\text{RMS}}$ (°)
200-250	5.40	26.20	10.36	37.92
250-300	3.53	26.44	5.59	49.04
300-350	9.15	27.23	14.09	52.52
>350	9.48	52.72	13.07	79.35

well approximated for ranges up to 350 km. Elimination of a select few outliers would improve the quality of the data. Beyond 350 km, there is much greater variability in the data values and the approximations are not as useful.

For the second extension cell there are more outliers present and the extrapolations, in general are not valid due to the high errors. One exception is the case for the range group $200 < \rho < 250$ km. The low errors could be due to a combination of a current pattern amenable to the continuity method, as discussed in Section 3.9.1, and low errors for the radar data.

Errors in direction are moderate even for the first extension cell and the error increases significantly for the second extension cell.

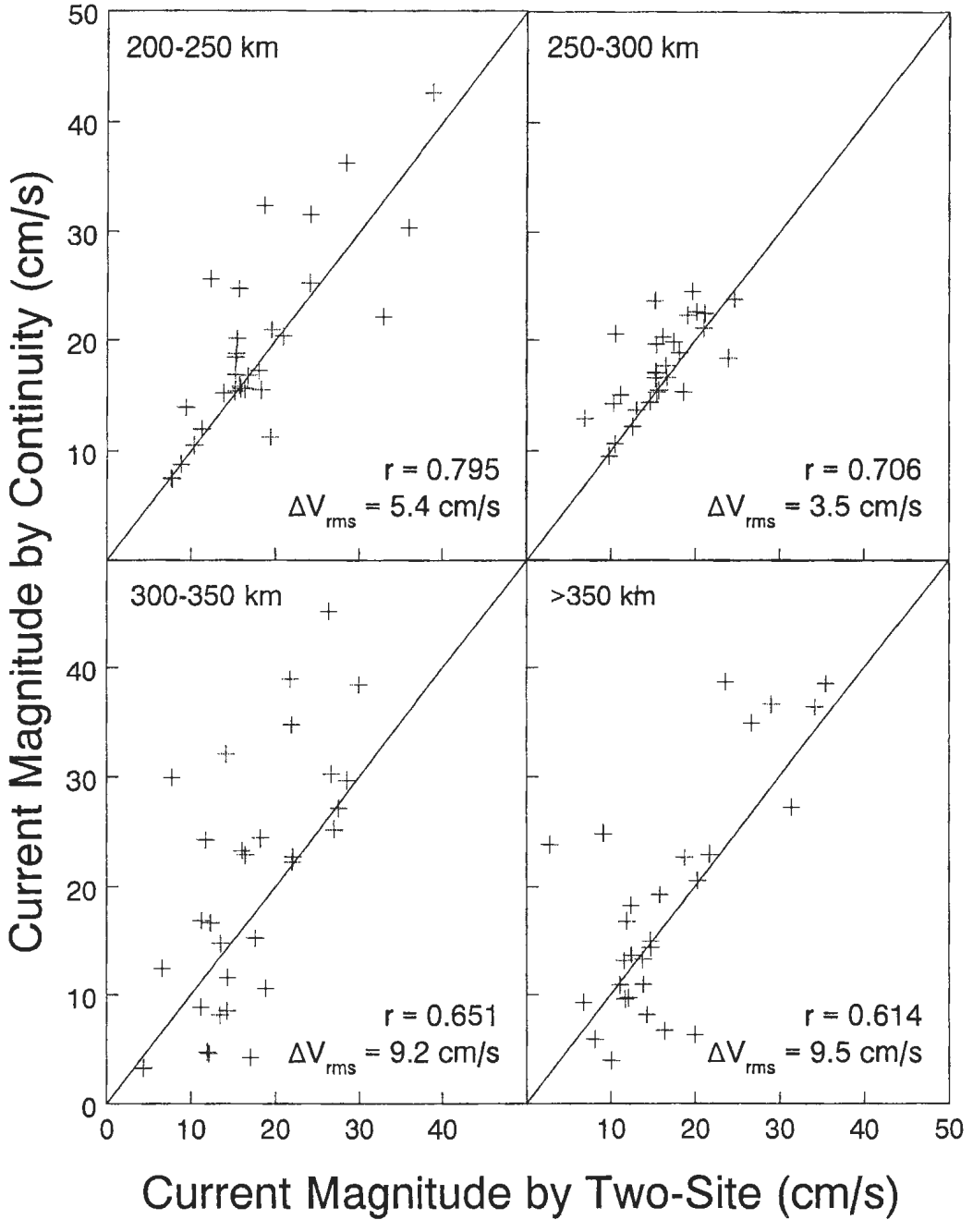

Figure 4.8: Scatter plots comparing current magnitudes as calculated by the Cartesian two-site method and the continuity equation for the first extension cell. Cape Bonavista is the reference.

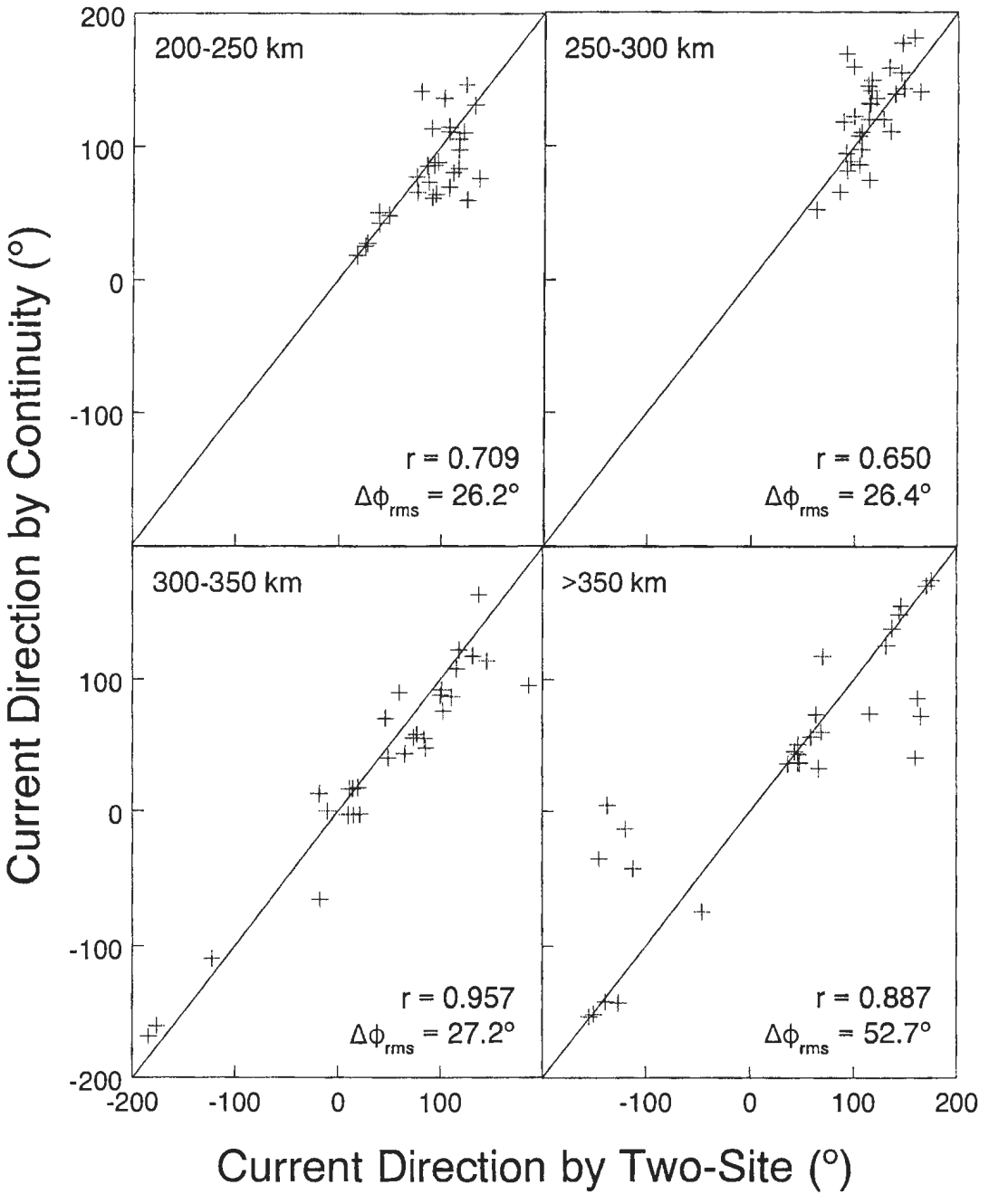

Figure 4.9: Scatter plots comparing current directions as calculated by the Cartesian two-site method and the continuity equation for the first extension cell. Cape Bonavista is the reference.

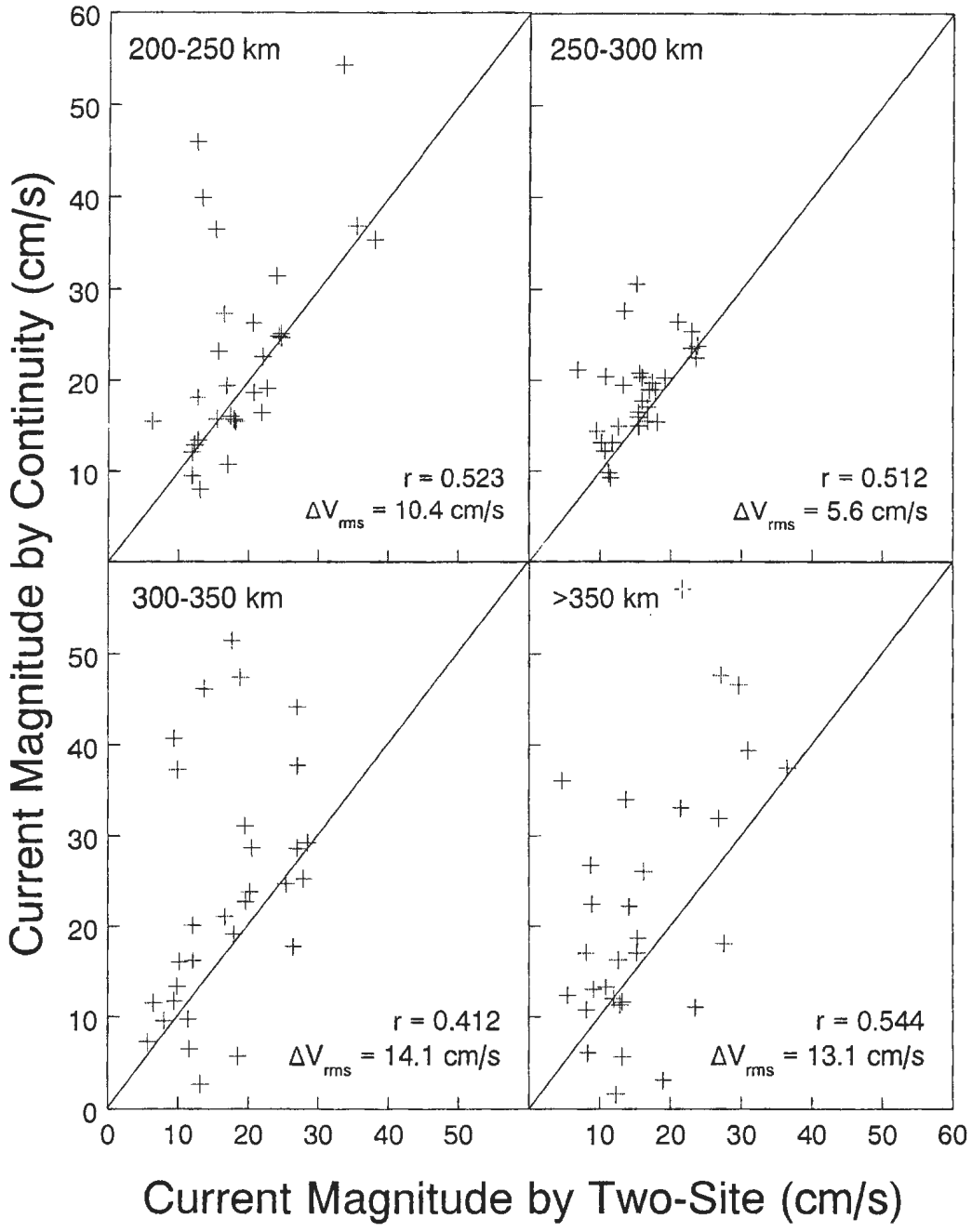

Figure 4.10: Scatter plots comparing current magnitudes as calculated by the Cartesian two-site method and the continuity equation for the second extension cell. Cape Bonavista is the reference.

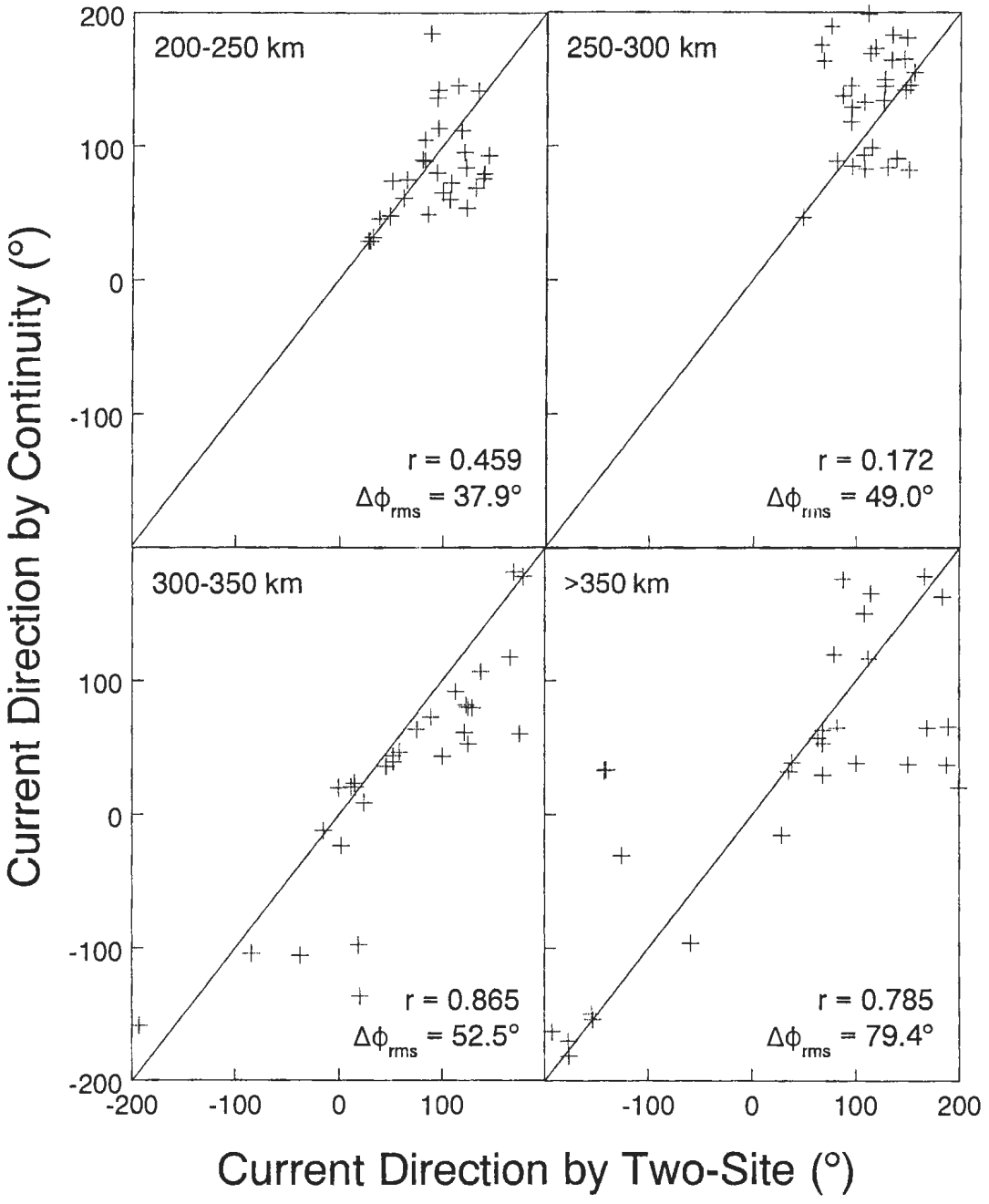

Figure 4.11: Scatter plots comparing current directions as calculated by the Cartesian two-site method and the continuity equation for the second extension cell. Cape Bonavista is the reference.

Chapter 5

Conclusions and Recommendations

5.1 Conclusions

5.1.1 Two-Site Currents

Although real data was not used to test the Cartesian and Cylindrical two-site algorithms for determining vector currents, realistic simulations were conducted. It was found that the Cartesian method was clearly the more consistent and reliable way to find the vector currents for all scan angles and current directions regardless of whether the Cape Race or Cape Bonavista site was used as the reference. However, the quality of the results varied slightly depending on the choice of reference. Thus, for the Cape Race/Cape Bonavista setup considered, the Cartesian method of equation (3.1) should be used to calculate the two site vector currents. The differences in performance due to reference location can be attributed to the different beamwidths and azimuthal coverages or the random FFT errors.

The differences in accuracy when each radar is used as the reference suggests that the Cartesian method may not be the best technique to use in all situations. It would be advisable to test, via simulations, the two-site methods each time radar placement, beamwidth and or azimuthal coverage change to verify which method is

more accurate.

5.1.2 Continuity Approach - Simulations

Simulations testing the utility of the continuity equation are presented in Sections 3.8 and 3.9. The results of the simulations indicate that there is a potential for using continuity to provide estimates of the total vector current. When dealing with uniform currents, there was a consistent improvement in the results as current magnitude increased and a degradation in performance as the current direction with respect to the initial radar scan angle increased. For all current magnitudes and directions, except for currents of magnitude 20 cm/s and directed perpendicular to the edge of the overlap, the continuity technique could be applied with some degree of success.

Analysis when non-uniform currents were used revealed that the accuracy of currents in the original overlap region were important for ensuring good quality extrapolations. Reasonable estimates of the vector current were obtained when the continuity technique was used with varying currents.

5.1.3 Continuity Approach - Real Data

The data presented in Chapter 4 indicates that the continuity equation yields good predictions for the magnitude and direction of the vector current for the first extension cell for all ranges when Cape Race is used as the reference. Direction errors are low to moderate for the first extension cell and are even higher in the second extension cell. As expected, due to the range dependent vertical velocity gradient and integration errors, the errors in magnitude and direction tend to increase with distance.

When Cape Bonavista is used as the reference, the same general results are found. Reasonable predictions are made for the first extension cell for ranges up to 350 km. Above 350 km, the error in direction is high. RMS errors in magnitude and direction

errors increase for the second extension cell, often to unusable levels.

5.2 Future Work

There are several questions that arose during the course of preparing this thesis which have not been explored extensively.

The radial currents used in this experiment have been calculated by performing an FFT on the radar time series to obtain the Doppler plot. The currents are found by locating the centroids of the Bragg peaks and this is limited by the resolution of the FFT. For the large wavelengths involved with surface-wave radar, the error due to the FFT can be quite large (see equations (1.5) and (3.4)). While the FFT is fast and computationally efficient, its precision is inversely dependent on the time length of the data segment which limits its usefulness for application to short data sets.

In recent years the time-varying Bragg components have been modeled [49] which allowed for high resolution parametric spectral techiques to be applied to the Bragg waves [50]. By constructing a Hankel matrix from the radar data it is found that all the characteristics relevant to the time-varying Bragg components are contained in the eigenvalues and eigenvectors of the Hankel matrix.

The result of using parametric spectral estimation is that the first order phenomena are enhanced which makes location of the centroids of the peaks easier. Hickey [32] reports that the major result is that the variance of radial values is reduced by a factor of three; the smooth transitions of currents across azimuth are more likely than the choppy FFT values as seen in Figure 4.1. The major drawback to using this high resolution technique is that the algorithm is very computationally intensive.

Based on measures of current variability in the Dead Sea [19] and a variety of current magnitudes, a non-uniform current was developed for testing the effectiveness of the continuity equation when applied to realistically varying currents. A more

realistic simulation could be carried out if a model of the flow on the Grand Banks is used and would provide valuable insight into performance expectations of the continuity equation when applied to real data. Places that historically display large net convergence or divergence will not be favorable to the use of continuity and so these locations can be avoided when analyzing real data.

Historical information on the variability of currents on the Grand Banks would be useful in determining the optimal number of range cells that should be averaged. Here, all work with simulations and real data used a range cell length, $\Delta\rho_s$, of 1500 m. However averaging was done across three range cells for simulations and nine cells for the real data. If more averaging is warranted, errors will be reduced and there would be fewer gaps in the real data. This would mean the continuity equation could be applied in more instances; less averaging would improve the spatial resolution.

No attempt has been made to compare the extrapolation of vector currents using continuity to that of model fitting. Such a comparison, based on the same data set, would be useful in determining if continuity does provide the expected advantage over a purely single site approach.

Simulations show that the two-site methods to construct vector currents do not depend heavily on range. However, currents found by the continuity technique degrade at large distances. It would be useful to know how much of the continuity range dependence is due to physical radar problems and how much is due to the technique itself. Drifter-derived radial currents compared with those of the radar at different range groupings can lend insight into this issue.

The application of the continuity technique can be modified so as to improve estimates of the tangential current for the second and higher extension cells. For the first extension, the extrapolation can be carried out as outlined in Chapter 3. Instead of extrapolating the current from the first extension cell into the second

extension cell, the algorithm can be started again from the overlap edge but this time using twice the beamwidth. The integral of equation (3.7) can be calculated as the average over the two adjacent range cells and the tangential current found will be the average over both cells. Since the tangential current in the first extension cell and the average over both cells are known, the current in the second cell can be found as well. Modification of the process can furnish estimates for any desired number of extension cells. The potential advantage of this approach is that, although the data in all previous extension cells is used in the future estimate, the iteration process is only carried out once each time and errors may be less likely to build up.

HF radar is a useful tool for the measurement of ocean surface currents and is capable of generating great volumes of data over a large spatial extent in real time. Although the techniques to measure vector currents using radar are well established there are many opportunities to expand this ability. Thus, HF radar-oceanography will remain an exciting research area and provide an important contribution in the context of ocean remote sensing.

Bibliography

[1] D. Hodgins, "Oceanographic information of the eastern Canadian offshore : adequacy for exploratory drilling," Data Report 82-3, Seaconsult Marine Research, St. John's, Newfoundland, 1984.

[2] T. C. L. Shay and H. Peters, "Very high-frequency radar mapping of surface currents," *IEEE Journal of Oceanic Engineering*, vol. 27, no. 2, pp. 155–168, 2002.

[3] D. Barrick, "Ocean surface currents mapped by radar," *Science*, vol. 198, pp. 139–144, 1977.

[4] P. B. M.M. Janopaul and J. Maistre, "Comparison of measurements of sea currents by HF radar and by conventional means," *IEEE Journal of Oceanic Engineering*, vol. 3, no. 4, pp. 409–422, 1982.

[5] G. Neuman, *Ocean Currents*. Amsterdam: Elsevier Publishing Company, 1968.

[6] K. Hickey, "Ocean surface current estimation using a long-range, single-station, high-frequency ground wave radar," Master's thesis, Memorial University of Newfoundland, St. John's, Newfoundland, 1999.

[7] B. Lipa and D. Barrick, "Least-squares methods for the extraction of surface currents from CODAR crossed-loop data: application at ARSLOE," *IEEE Journal of Oceanic Engineering*, vol. 8, no. 4, pp. 226–253, 1983.

[8] D. Crombie, "Doppler spectrum of sea echo at 13.56 Mc./s.," *Nature*, vol. 175, pp. 681–682, 1955.

[9] R. A. Serway, *Physics for Scientists and Engineers with Modern Physics.* Philadelphia, PA: Saunders College Publishing, 1992.

[10] B. Cushman-Roisin, *Introduction to Geophysical Fluid Dynamics.* Englewood Cliffs: Prentice-Hall, Inc., 1994.

[11] M. Earle and J. Bishop, *A Practical Guide to Ocean Wave Measurement and Analysis.* ENDECO Inc., Marion, MA, U.S.A., 1984.

[12] D. Barrick, "HF radio oceanography-a review," *Boundary-Layer Meteorology*, vol. 13, pp. 23–43, 1978.

[13] J. R. Wait, "Theory of ground wave backscatter from sea waves," *Journal of Geophysical Research*, vol. 71, pp. 4839–4842, 1966.

[14] D. Barrick and W. H. Peake, "A review of scattering from surfaces with different roughness scales," *Radio Science*, vol. 3, pp. 865–868, 1968.

[15] D. Barrick, "Remote sensing of sea state by radar," in *Remote Sensing of the Troposphere* (V. Derr, ed.), ch. 12, pp. 1–46, Washington, DC: U.S. Government Printing Office, 1972.

[16] K. Hasselmann, "Determination of ocean wave spectra from Doppler return from sea surface," *Nature Physical Science*, vol. 229, pp. 16–17, 1971.

[17] D. Crombie, "Resonant backscatter from the sea and its application to physical oceanography," in *Oceans '72 Conf. Rec.*, (IEEE Publ. No. 72CHO 660-1 OCC), pp. 173–179, 1972.

[18] D. Prandle and D. Ryder, "Measurement of surface currents in Liverpool Bay by high-frequency radar," *Nature*, vol. 315, pp. 128–131, 1985.

[19] F. S. H. Essen, K. W. Gurgel and Z. Sirkes, "Horizontal variability of surface currents in the Dead Sea," *Oceanologica Acta*, vol. 18, pp. 455–467, 1995.

[20] A. Frisch and B. Weber, "Applications of dual-Doppler HF radar measurements of ocean surface currents," *Remote Sensing of Environment*, vol. 12, pp. 273–282, 1982.

[21] R. Stewart and J. Joy, "HF radio measurements of surface currents," *Deep-Sea Research*, vol. 21, pp. 1039–1049, 1974.

[22] E. Gill, *The Scattering of High Frequency Electromagnetic Radiation from the Ocean Surface: An Analysis Based on a Bistatic Ground Wave Radar Configuration.* PhD thesis, Memorial University of Newfoundland, St. John's, Newfoundland, 1999.

[23] B. Dawe, "Radio wave propagation over earth: Field calculations and an implementation of the roughness effect," Master's thesis, Memorial University of Newfoundland, St. John's, Newfoundland, 1988.

[24] D. Trizna and A. Long, "Mapping of North Atlantic winds by HF radar backscatter interpretation," *IEEE Transactions on Antennas and Propagation*, vol. 21, pp. 680–685, 1973.

[25] E. Gill and J. Walsh, "Extraction of ocean wave parameters from HF backscatter received by a four-element array: Analysis and application," *IEEE Journal of Oceanic Engineering*, vol. 17, no. 4, pp. 376–386, 1992.

[26] C. Balanis, *Antenna Theory Analysis and Design.* New York: John Wiley and Sons, Inc., 2 ed., 1997.

[27] J. Ward, "Power spectra from ocean movements measured remotely by ionospheric radio backscatter," *Nature*, vol. 223, pp. 1325–1330, 1969.

[28] S. Rice, "Reflection of electromagnetic waves from a slightly rough surface," in *Theory of Electromagnetic Waves* (K. Kline, ed.), pp. 351–378, New York: Interscience, 1951.

[29] D. Barrick, "First-order theory and analysis of MF/HF/VHF scatter from the sea," *IEEE Transactions on Antennas and Propagation*, vol. 20, pp. 2–10, 1972.

[30] E. Gill and J. Walsh, "High-frequency bistatic cross sections of the ocean surface," *Radio Science*, vol. 36, no. 06, pp. 1459–1475, 2001.

[31] K. Hickey, E. Gill, J. Helbig, and J. Walsh, "Measurement of ocean surface currents using a long-range, high-frequency ground wave radar," *IEEE Journal of Oceanic Engineering*, vol. 19, no. 4, pp. 549–554, 1994.

[32] R. K. K.J. Hickey and J. Walsh, "Parametric estimation of ocean surface currents with HF radar," *IEEE Journal of Oceanic Engineering*, vol. 20, no. 2, pp. 139–144, 1995.

[33] B. Lipa and D. Barrick, "Analysis methods for narrow-beam high-frequency radar sea echo," Technical Report ERL 420-WPL 56, National Oceanic and Atmospheric Administration, U.S. Department of Commerce, 1982.

[34] D. Barrick and B. Lipa, "A compact transportable HF radar system for directional coastal wave field measurements," in *Ocean Wave Climate Symposium* (M. Earle and A. Malahoff, eds.), ch. 12, pp. 153–201, New York: Plenum Press, 1979.

[35] A. Frisch and J. Leise, "A note on using continuity to extend HF radar surface-current measurements," *Journal of Geophysical Research*, vol. 86, no. 11, pp. 11089–11090, 1981.

[36] D. Barrick, "The role of the gravity-wave dispersion relation in HF radar measurements of the sea surface," *IEEE Journal of Oceanic Engineering*, vol. 11, no. 2, pp. 286–292, 1986.

[37] H. E. K.W. Gurgle and S.P., "High-frequency radars: physical limitations and recent developments," *Coastal Engineering*, vol. 37, pp. 201–218, 1999.

[38] M. Tucker, *Waves in Ocean Engineering Measurement, Analysis, Interpretation.* New York: Ellis Horwood, 1991.

[39] W. Pierson and L. Moskowitz, "A proposed spectral form for fully developed seas based upon the similarity theory of S.A. Kitaigorodskii," *Journal of Geophysical Research*, vol. 69, no. 24, pp. 5181–5190, 1964.

[40] D. Barton, *Modern Radar System Analysis.* Norwood, MA: Artech House, Inc., 1988.

[41] International Telecommunications Union, Geneva, *Propagation in Ionized Media (ITU-R Recommendations, 1994 PI Series Volume)*, 1994.

[42] W. Pierson, "Wind generated gravity waves," *Advances in Geophysics*, vol. 2, pp. 93–178, 1955.

[43] D. Barrick, "Sea backscatter at HF: interpretation and utilization of the echo," *Proceedings of the IEEE*, vol. 62, no. 6, pp. 673–680, 1974.

[44] L. Zedel, Department of Physics and Physical Oceanography, Memorial University of Newfoundland, *Personal Correspondance*, 2003.

[45] C. Nelson, "Wind stress and wind stress curl over the California Current," Technical Report NMFS SSRF-714, National Oceanic and Atmospheric Administration, U.S. Department of Commerce, 1977.

[46] B. Lathi, *Modern Digital and Analog Communication Systems, Third Edition.* New York: Oxford University Press, 1998.

[47] V. Klemas, "Satellite, aircraft, and drogue studies of coastal currents and pollutants," *IEEE Transactions on Geoscience Electronics*, vol. 15, no. 2, pp. 97–108, 1977.

[48] C. A. B. Petrie, "Circulation on the Newfoundland continental shelf," *Atmosphere-Ocean*, vol. 21, no. 2, pp. 207–226, 1982.

[49] R. Khan, "Ocean-clutter model for high-frequency radar," *IEEE Journal of Oceanic Engineering*, vol. 16, pp. 181–188, 1991.

[50] K. A. C.L. Dimonte, "Tracking the frequencies of super-imposed time-varying signals," in *Proc. ICASSP 90*, (Albuquerque, NM), pp. 2536–2542, 1990.

Appendix A

Code for Plotting Radar Cross Sections of the Ocean

```
/*********************************************************************
  This file is used to calculate the second order cross section of the
  ocean surface. It differs from alternate.cpp by not using such a
  fine spacing around the sqrt(2) and 2^.75 singularities which means
  there are fewer overall frequency points to deal with.

  For the parameters specified in "file.txt", the noiseless, ideal
  cross section of the ocean is calculated based on an infinite time
  series. The routine "noise()" converts the frequency data to a finite
  time series and adds the effect of external noise. The FFT analysis
  can be conducted in Matlab to convert the cross sections back to the
  frequency domain.

  The final output that will be the noise and ocean clutter time
  signals written to file. The first column will have the real part
  of the noise+clutter, the second column will have the imaginary part
  of the noise+clutter. This file name is "time.xls" and it can be
  processed by matlab to plot the cross section.

  The input file, "file.txt" is a simple text file whose entries are
  separated by a single space. The input data fields are arranged as:
thDo - angle waves make wrt radar look direction (for spherical
attenuation data)
k0 - radio wave number
deltaPs - length of surface patch (m)
U - wind speed (m/s)
Vx,Vy - x and y components of total current vector (cm/s)
x,y - coordinates of surface patch (meters). x is North
```

```
F1 - spherical attenuation for spherical earth
Fa - external noise figure for frequency of interst

   Date: June/2002
  Author: Pradeep Bobby
**********************************************************************/
#include <iostream.h>
#include <fstream.h>
#include <stdlib.h>
#include <math.h>
#include "data.h"

int main(){
double k0; //k0 = radar wavenumber, thDo =  dominant wave direction
//wrt radar
//thDo is angle of wind wrt radar look, thDom is angle of wind wrt
//coordinate frame (i.e. radar baseline)
double thDo, thDom;
//deltaPs = surface patch width, Fa = external noise figure
int deltaPs, Fa;
//U = wind speed in m/s; Vx, Vy = components of current
//x,y = coordinates of surface patch
//F1 is spherical attenuation value for each radar
double U, Vx,Vy, x, y, F1;
double wB; //Bragg frequency (rad/s)
double freq[freqPoints]; //holds the Doppler frequencies
double* freqPnt = freq;
double theta1[thetaPoints]; //Angle for vector k1
double* theta1Pnt = theta1;
for(int r=0; r<thetaPoints; r++){
theta1[r] = -pi + r*thInc;
}

//For values of wD outside the sqrt(2) singularity, not all values
//of theta1 are valid
double beta1 = 0; //see Gill, 1999 pg. 141
int m1, m2;
//Array to hold the k1 values for a single wD and a pointer used to
//access the array
double k1[thetaPoints] = {0.};
double* k1Pnt = k1;

//Array to hold the k2 values for a single wD and a pointer used to
```

```
//access the array
double k2[thetaPoints] = {0.};
double* k2Pnt = k2;
double theta2[thetaPoints] = {0.};
double* th2Pnt = theta2;

//Array to hold the magnitude of the coupling coefficient
double gamma[thetaPoints] = {0.};
double* gammaPnt = gamma;

//Parameters used for the wave spectrum calculations
double S11[thetaPoints] = {0.}; //for k1
double S12[thetaPoints] = {0.}; //for k2

double* S11Pnt = S11;
double* S12Pnt = S12;

double output1[freqPoints] = {0.}; //holds cross section
double* outPnt1 = output1;

double outFirst1[freqPoints] = {0.}; //1st order cross section
double* firstOrd1 = outFirst1;

//large arrays used after the interpolate() function evens the
//frequency spacing
double finalFreq[numFinalFreq]; //frequency values
double finalOutput1[numFinalFreq]; //cross section values
double* fFreq = finalFreq;
double* fOutput1 = finalOutput1;

double Dop1; //Doppler shift

readData("file.txt", thDo, thDom, k0, deltaPs, U, Vx, Vy,
x, y, F1, Fa); //read data from file
wB = sqrt(2*g*k0);

initFreq(freqPnt, wB); //initialize the frequency array

ofstream outputFile;
outputFile.open("second.xls");

//Have one huge external loop that will cycle through all the values
//of frequency
```

```
for(int i=0; i<freqPoints; i++){
//This code calculates the value of beta1 which is a limiting value
//of theta1 for wD sqrt(2) singularity

if(fabs(freq[i]) > 1.05*wB || fabs(freq[i]) < .95*wB){
beta1 = 0; //see Gill pg. 141
if(fabs(freq[i]) > sqrt(2)*wB){
findBeta1(freq[i], wB, beta1);
}
findm1m2(freq[i], m1, m2, wB);
ystar(freq[i], k0, beta1, m1, m2, k1Pnt);
//find values for the second scattering vector, magnitude and angle
findK2(k1Pnt, k2Pnt, th2Pnt, k0, beta1);

//find the coupling coefficient
coupling(gammaPnt, k1Pnt, k2Pnt, th2Pnt, freq[i], m1, m2, k0);

//Calculate the wave spectrum
spectrum(k1Pnt, theta1Pnt, S11Pnt, beta1, m1, k0, thDom, U); //K1
spectrum(k2Pnt, th2Pnt, S12Pnt, beta1, m2, k0, thDom, U); //K2

//Finally, numerically calculate the integral
integral(S11Pnt, S12Pnt, k1Pnt, k2Pnt, beta1, gammaPnt, freq[i], m1,
m2, k0, output1[i]);
}

//This adds in the first order component
if(fabs(freq[i])<1.8*wB && fabs(freq[i])>0.45*wB){
      first(freq[i], k0, deltaPs, U, thDom, outFirst1[i]);
}
}

//Smooth out the ripples in the first order spectra and apply
//Hamming window to second order values - firstOrd is a pointer
//pointing to output11
smooth(firstOrd1);

//combines the smoothed first order and second order cross
//section results
for(i=1; i<freqPoints; i++){
output1[i] = outFirst1[i] + output1[i];
}
//Code to mitigate the fake singularities near zero Doppler
```

```
i=0;
while(fabs(freq[i]) < 0.6*wB){
if(output1[i+1] > 2*output1[i] || output1[i+1] < 0.5*output1[i]){
output1[i+1] = output1[i];
}
i++;
}

//Set up the frequency array
for(i=0; i<numFinalFreq; i++){
fFreq[i] = (-2 + 0.002*i) *wB;
}
interpolate(fOutput1, freqPnt, outPnt1, wB);

fFreq[0] = -fFreq[numFinalFreq-1];
fFreq = finalFreq;
fOutput1 = finalOutput1;
freqPnt = freq;

//Write the interpolated frequency values and non-logged cross
//section to file
for(i=0; i<numFinalFreq; i++){
outputFile << finalFreq[i] << '\t' << fOutput1[i] << /*'\t'
<< fOutput2[i] <<*/ '\n';
}
outputFile.close();

findDop(Vx, Vy, x, y, k0, Dop1);

ofstream DopFile;
DopFile.open("doppler.dat");
//Dop1 is theoretical Doppler shifts
DopFile << Dop1 << '\t' << wB << '\n';
DopFile.close();

//Now call the noise program, actually write the clutter and noise
//parts to file. This routine is also responsible for writing the
//Doppler shift in frequency
noise(k0, deltaPs, fFreq, fOutput1, sqrt(x*x +y*y), Dop1*2*pi, F1, Fa);
return 0;
}

/*********************************************************************
```

```
 The subroutine readData is used to read in the parameters of interest
  from a text file

  Inputs: fileName- name of the file that holds the input data
thDo - angle waves make wrt radar look direction (for spherical
 attenuation data)
thDom - angle waves make wrt radar baseline (used in cross section
equations)
k0 - radio wave number
deltaPs - length of surface patch (m)
U - wind speed (m/s)
Vx,Vy - x and y components of total current vector (cm/s)
x,y - coordinates of surface patch (meters). x is North
F1 - spherical attenuation for spherical earth
Fa - external noise figure for frequency of interst


  Modifies: k0, thetaDom, deltaPs
U
Vx, Vy
x, y
F,
Fa

  Pre: Input file in proper format

  Post: Proper values assigned to thetaDom, k0, deltaPs, U, Vx, Vy, x,
    y, d, F1, F2
*********************************************************************/
void readData(const char* fileName, double& thDo, double& thDom,
double& k0, int& deltaPs, double& U, double& Vx, double& Vy,
double& x, double& y, double& F, int& Fa){

ifstream dataFile; //File from which data is read

dataFile.open(fileName);
if(dataFile.is_open()){
dataFile >> thDo;
dataFile >> k0;
dataFile >> deltaPs;
dataFile >> U;
dataFile >> Vx;
dataFile >> Vy;
```

```
dataFile >> x;
dataFile >> y;
dataFile >> F;
dataFile >> Fa;
}
dataFile.close();
thDo = thDo*pi/180; //convert the wind dir. wrt radar look to rads
//Now find the overall wind direction
double ang = atan2(y,x); //this is radar look direction
thDom = ang + thDo;
}

/*********************************************************************
  The subroutine initFreq is used to initialize the frequency vectors

  Inputs: freq - pointer to array that holds values of Doppler
frequency
k0 - radar wavenumber

  Modifies: array pointed to by freq

  Pre: None
  Post: The proper values of frequency will be calculated
*********************************************************************/
void initFreq(double* freq, double wB){

//Code to set up frequency vector
for(int i=0; i<20; i++){
freq[i] = ((2-1.69)/(20) * (i) -2) *wB;
     freq[freqPoints -(i+1)] = -1*freq[i];
}

//Close spacing for 2^.75 singularity - 10 points
for(i=20; i<30; i++){
freq[i] = ((1.69-1.67)/(10) * (i-20) -1.69) *wB;
    freq[freqPoints -(i+1)] = -1*freq[i];
}

//Rough (actually it is pretty close) spacing from 2^.75 to 2^.5
//singularities - 20 points
for(i=30; i<50; i++){
freq[i] = ((1.67-1.42)/(20) * (i-30) -1.67) *wB;
    freq[freqPoints -(i+1)] = -1*freq[i];
```

```
}

//Close spacing for sqrt(2) singularity - 10 points
for(i=50; i<60; i++){
freq[i] = ((1.42-1.4)/(10) * (i-50) -1.42) *wB;
     freq[freqPoints -(i+1)] = -1*freq[i];
}

//Rough spacing from outside Bragg to sqrt(2) singularity - 20 points
for(i=60; i<80; i++){
freq[i] = ((1.4-1.1)/(20) * (i-60) -1.4) *wB;
     freq[freqPoints -(i+1)] = -1*freq[i];
}

//Close spacing for around Bragg - 40 points
for(i=80; i<120; i++){
freq[i] = ((1.1-0.9)/(40) * (i-80) -1.1) *wB;
     freq[freqPoints -(i+1)] = -1*freq[i];
}

//Normal spacing for inside Bragg - 20 points, .875 works best
for(i=120; i<=149; i++){
freq[i] = ((.9/30) * (i-120) -0.9) *wB;
     freq[freqPoints -(i+1)] = -1*freq[i];
}

}

/*************************************************************************
  The subroutine findBeta1 is used to determine the limits of the
  angle for the various frequency ranges
  When the |wDop| < sqrt(2) * wB, the limits are fully -pi to pi.
  Outside this range the integration is from -pi to -b1 and then from
  b1 to pi. The value of b1 will change for every Doppler freq.

  Inputs: wD - Doppler frequency
wB - Bragg freq
beta1

  Modifies: beta1

  Pre: None
  Post: beta1 is found
```

```
**********************************************************************/
void findBeta1(double wD, double wB, double& beta1){
beta1 = acos(2*wB*wB/pow(wD,2));
}

/**********************************************************************
  The subroutine findm1m2 is used to determine values of m1 and m2
  that specifies the Doppler region. Program written with the
  assumption that k1 < k2

  Inputs: wD - Doppler frequency
m1
m2
wB - Bragg frequency

  Modifies: m1 and m2

  Pre: k1 < k2
  Post: The correct values of m1 and m2 are found
**********************************************************************/
void findm1m2(double wD, int& m1, int& m2, double wB){
if(wD <= -wB){
m1 = 1;
m2 = 1;
}
else if(wD >= wB){
m1 = -1;
m2 = -1;
}
else if(wD>0 && wD<wB){
m1 = 1;
m2 = -1;
}
else if(wD<0 && wD>-wB){
m1 = -1;
m2 = 1;
}
}

/**********************************************************************
  The subroutine yStar solves the delta function constraint using the
  Newton-Raphson numerical integration technique
  Solution will be constrained to find values for which k1<k2
```

```
  Inputs: wD - Doppler shift
k0 - radio wavenumber
beta1 - see description of function findBeta1()
m1, m2 - Doppler range indicators
k1Pnt - pointer to array holding magnitude of k1

  Modifies: array pointed to by k1Pnt

  Pre: None
  Post: Magnitude of the first scattering vector will be calculated
*****************************************************************/
void ystar(double wD, double k0, double beta1, int m1, int m2,
double* k1Pnt){

double theta =-pi; //angle of K1, initialize to allow entry to loop
int j = 0;
double temp;
for(j=0; j<thetaPoints; j++){
theta = -pi + j*thInc;
if(fabs(theta) >= beta1){
temp = solveCubic(wD, k0, m1, m2, theta);
k1Pnt[j] = temp*temp;
}
else{
k1Pnt[j] = 0;
}
}
}

/*****************************************************************
  The subroutine solveCubic uses the Newton-Raphson technique to solve
  for the roots of the cubic equation which is the delta function
  constraint

  Inputs: freq single frequency value
k0 radar wave number
m1,m2 Doppler range indicators
th angle of K1

  Modifies: none

  Pre: None
```

```
  Post: The solution to the input cubic is and returned which
  represents the solution of the delta function constraint for a
  single frequency
*****************************************************************/
double solveCubic(double freq, double k0, int m1, int m2, double th){
double wB = sqrt(2*g*k0);
double tol = 0.0001; //error margin for solution
//starting point for Newton-Raphson
double Y0 = fabs(-m1/sqrt(g) *(freq + m2*wB));
double temp = Y0;
double Y1 = Y0+2*tol;
double G =0; //G(Ystar) = 0
double dG =0; //derivative of function G


//Solve using Newton Raphson Method
while (fabs(Y1-temp) > tol){
temp = Y0;
G = freq + m1*sqrt(g)*Y0 +m2*sqrt(g)*pow(pow(Y0,4) + 4*k0*k0 -
4*k0*pow(Y0,2) * cos(th), 0.25);
dG = m1*sqrt(g) + m2*sqrt(g)*(pow(Y0,3) -
2*k0*Y0*cos(th))/(pow(pow(Y0,4) + 4*k0*k0 - 4*k0*pow(Y0,2) * cos(th), .75));
Y1 = fabs(Y0 - G/dG);
Y0 = Y1;
}
return Y1;
}

/*****************************************************************
  The subroutine findK2 uses the triangle identity and other relations
  to find the value (magnitude and angle) of the second scattering
  vector

  Inputs: k1Pnt - pointer to array of k1 values (for a given wD)
k2Pnt - ptr to array of k2 values to be found (for a given wD)
th2Pnt - ptrto array of angles for k2 to be found (for a given wD)
k0 - radar wavenumber
pi
beta1 - see findBeta1()

  Modifies:

  Pre: None
```

```
  Post: The magnitude and angle of the K2 vector will be found and
writtento the appropriate matrices

*****************************************************************/
void findK2(double* k1Pnt, double* k2Pnt, double* th2Pnt, double k0,
double beta1){
//see page 141 of Gill 1999 for beta1 and beta2
double beta2;
double theta1 = -pi; //angle for k1 vector

for(int i=0; i<thetaPoints; i++){
if(k1Pnt[i] == 0){
k2Pnt[i] = 0;
th2Pnt[i] = 0;
}
else{
theta1 = -pi + i*thInc;
k2Pnt[i] = sqrt(pow(k1Pnt[i], 2) + pow(2*k0, 2) -
4*k1Pnt[i]*k0*cos(theta1));
beta2 = (pow(2*k0,2)+ pow(k2Pnt[i], 2)- pow(k1Pnt[i], 2))/
(4*k0* k2Pnt[i]);

if(beta2 > 1.){ //just make sure I don't get invalid values due to
beta2 = 1.; //taking the cosine of an argument greater than unity
}
else if(beta2 < -1.){
beta2 = -1.;
}
if(theta1 < -beta1){
th2Pnt[i] = acos(beta2);
}
else{
th2Pnt[i] = -acos(beta2);
}
}
}
}

/*****************************************************************
  The subroutine coupling calculates the symmetricized coupling
  coefficient (combination of the hydrodynamic and electromagnetic
  terms). Only the magnitude is returned.
```

```
  Inputs: numTheta- number of theta values used in range
realPnt - pointer to matrix of real component of coupling co-e
imagPnt - pointer to matrix of imag component of coupling co-e
k1Pnt - ptr to k1 values (subject to delta function constraint)
k2Pnt - ptr to k2 values (subject to delta function constraint)
theta2Pnt- pointer to matrix of angles for k2
k0 - radar wavenumber

  Modifies: array pointed to by gamma

  Pre: None
  Post: The magnitude of the coupling coefficient is found

*****************************************************************/
void coupling(double* gamma, double* k1Pnt, double* k2Pnt,
double* th2Pnt, double wD, int m1, int m2, double k0){
double th0 = -pi; //initial value for theta1 values

//break symmetricized gamma into three terms (see Gill 1999, pg 142).
//Total gamma = reA+imA + reB+imB + reC+imC

//A and B are the symmetricized EM term, C is the hydrodynamic term

//K = K1 + K2 (in the vector sense) see Gill 1999 pg. 135
double reA, imA;
double reB, imB;
double reC; //hydrodynamic term has only real part
//see Gill 1999 pp. 141,142 and logbook2 pg 69
double den1, den2, k1, k2, temp1, temp2, th1, th2, num2, imag, w1,
 w2, K;
for(int i=0; i<thetaPoints; i++){
k1 = k1Pnt[i];
k2 = k2Pnt[i];

if(k1 == 0){
gamma[i] = 0;
}
else{
th1 = th0 + i*thInc;
th2 = th2Pnt[i];
//angle of p2_hat vector is the same as theta_1 i.e. zero
//(not theta_K_1)
//first find the values for A
```

```
den1 = k0*k0 + k1*(k1-2*k0*cos(th1)); //good
num2 = k1*cos(th1) * (k2*k1*cos(th2-th1) - k2*k0*cos(th2));
//If the argument of the square root is negative...
if(den1-k0*k0 < 0){
den2 = sqrt(k0*k0 -den1);
imag = -den2; //sqrt(k1*(k1 - 2*k0));
reA = 0;
imA = .5*(imag +k0)*num2/(den1*den2);
}
else{
den2 = sqrt(den1 - k0*k0);
imag = den2;
reA = .5* k0* num2/(den1*den2);
imA = .5* imag* num2/(den1*den2);
}

//find values for term B
den1 = k0*k0 + k2*k2 - k2*2*k0*cos(th2);
num2 = k2*cos(th2) * (k1*k2*cos(th1-th2) - k1*k0*cos(th1));
if(den1 - k0*k0 < 0){
den2 = sqrt(-k2*k2 + k2*2*k0*cos(th2));
imag = -den2;
reB = 0;
imB = .5*(imag + k0)*num2/(den1*den2);
}
else{
den2 = sqrt(den1-k0*k0);
imag = den2;
reB = .5* k0* num2/(den1*den2);
imB = .5* imag* num2/(den1*den2);
}
//find values for term c
w1 = sqrt(g*k1)*m1;
w2 = sqrt(g*k2)*m2;
K = +2*k0; //K = +2*k0 see Gill pg 139, bottom of page
temp1 = k1*k2*(1-cos(th1-th2));
temp2 = (g*K + pow(wD, 2))/(g*K - pow(wD, 2));
reC = (k1+k2 + g/(w1*w2) * temp1 * temp2);

//Put it all together
temp1 = sqrt(pow(reA+reB+reC, 2) + pow(imA+imB, 2));
gamma[i] = temp1;
}
```

```
}
}

/*********************************************************************
  The subroutine spectrum computes the PM directional ocean spectra

  Inputs: kPnt - pointer to matrix of k values (subject to delta
   function constraint)
thPnt - pointer to array of angular values
SPnt - pointer to matrix holding wave spectrum
beta1 - see findBeta1()
m - indicator of which range the frequency falls in
k0 - radar wavenumber
thDom - dominant wave direction wrt radar baseline
U - wind speed, m/s

  Modifies: array pointed to by SPnt

  Pre: None
  Post: Proper values for the wave spectrum are entered matrix
  pointed to by SPnt

*********************************************************************/
void spectrum(double* kPnt, double* thPnt, double* SPnt, double beta1,
 int m, double k0, double thDom, double U){

//spreading factor, actually s=2 and 2s is used in the exponent
const double s = 4.;
double f, gTh; //Spectrum S(K) = f(k)*g(theta)

int i = 0;
double theta = pi; //Initialize just to enter loop
//Critical wave number. Actually a function of wind speed and gravity
double kc = g/(U*U);

for(i=0; i<thetaPoints; i++){
if(kPnt[i] == 0) {
SPnt[i] = 0;
}

else{
theta = thPnt[i];
f = 0.0081/(4*pow(kPnt[i],4)) *exp(-0.74*pow(kc/kPnt[i], 2));
```

```
gTh = pow(cos((theta - thDom + (1-m)*pi/2)/2), 4)*4/(3*pi);
SPnt[i] = f*gTh;
}
}
}

/*********************************************************************
  The subroutine integral puts all the pieces together and numerically
  calculates the integral that is representative of the second order
  cross section of the ocean surface. Since this routine is used to
  find currents, the integral will be calculated twice, once for each
  of the two radars with its unique look direction

  Inputs: S11Pnt - pointer to matrix holding wave spectrum for and K1
S12Pnt - pointer to matrix holding wave spectrum for and K2
k1Pnt - ptr to k1 values (subject to delta function constraint)
k2Pnt - ptr to k2 values (subject to delta function constraint)
beta1 - see findBeta1()
gammaPnt - pointer to matrix holding the mag. of coupling co-e
wD - current Doppler frequency value (rad/s)
m1,m2 - variables denoting the Doppler region
k0 - radar wavenumber
integ1 - value of the cross section for radar 1

  Modifies: integ1

  Pre: None
  Post: calculates the cross section for a single frequency value

*********************************************************************/
void integral(double* S11Pnt, double* S12Pnt, double* k1Pnt,
double* k2Pnt, double beta1, double* gammaPnt, double wD, int m1,
int m2, double k0, double& integ1){

double theta1 = pi;
double Y; //Y = sqrt(K1)
//den1Y and den2Y are for part of for the partial(Y)/partial(wD) term
double den1Y;
double den2Y;
double part; //full value of partial(Y)/partial(wD)
double integrand1[thetaPoints] = {0.}; //values of the integrand
double mult = pow(2,7)*pi*pi*k0*k0;
```

```
int i = 0;
integ1 = 0;
for(i=0; i<thetaPoints; i++){
if(k1Pnt[i] == 0){
integrand1[i] = 0;
}
else{
theta1 = -pi + i*thInc;
Y = sqrt(k1Pnt[i]);
den1Y = m1*m2*(pow(Y, 3) - 2*Y*k0*cos(theta1));
den2Y = pow(pow(Y,4) + 4*k0*k0 - 4*Y*Y*k0*cos(theta1),.75);
//This has singularities. See Lipa and Barrick 1982
part = 1/(sqrt(g)* fabs(1+ den1Y/den2Y));
integrand1[i] = S11Pnt[i]*S12Pnt[i]*pow(gammaPnt[i], 2)
*pow(Y, 3)*part;
}
}
integ1 = 0.5*thInc*(integrand1[0] + integrand1[thetaPoints-1]);
int k = 1;
while(k < thetaPoints-1){
integ1+= integrand1[k]*thInc;
k++;
}
k = 1;

integ1 = integ1*mult;
}


/*************************************************************************
  The subroutine first calculates the first order cross section of the
  ocean

  Inputs: wD - current value of Doppler frequency
k0 - radar wavenumber
deltaPs - length of scattering patch
U - wind speed (m/s)
thDom - dominant direction of the waves wrt radar baseline
integ - value of the cross section for that frequency value

  Modifies: integ

  Pre: None
```

```
  Post: calculates the 1st order cross section for a single freq. val.

**********************************************************************/
void first(double wD, double k0, double deltaPs, double U,
double thDom, double& integ){

int s = 4; //Spreading factor
double k11 = pow(wD,2)/g;
double mult = pow(2,4)*pi * k0*k0 * pow(k11,2.5) * deltaPs/sqrt(g);
int m = 1; //m is +ve for -ve Doppler shifts
double theta = 0; //see Gill pg. 130, theta = 0 for monostatic
double kc = g/(U*U); //critical wavenumber
double S11,f1, g1; //Wave spectrum S(mK) = f(K)*g(theta)

//Find the value of m
if(wD > 0) {m = -1;}

if(k11 == 0) {S11 = 0;}
else{
f1= 0.0081/(4*pow(k11,4)) * exp(-.74* pow((kc/k11),2));
g1 = pow(cos((theta-thDom + (1-m)*pi/2)/2),4) * 4/(3*pi);
S11 = f1*g1;
}

double arg = 0.5*deltaPs*(k11 - 2*k0);
//Try to get rid of some divide by zero errors
if(arg != 0){
     integ = mult*S11*pow(sin(arg)/arg,2);
}

}

/**********************************************************************
  The subroutine smooth uses peak detection and linear interpolation
  to smooth out the peaks produced by the first order sampling
  function

  Inputs: firstOrd - pointer to array holding raw values of first
order cross section

  Modifies: array pointed to by firstOrd

  Pre: None
```

```
  Post: smoothed values of the first order cross section are
  rewritten to the array pointed to firstOrd

**********************************************************************/
void smooth(double* firstOrd){
int count = -1;
int index[freqPoints] = {0};
//This is peak detection for the first order spectra
for(int i=1; i<freqPoints-2; i++){
    if(firstOrd[i-1] < firstOrd[i] && firstOrd[i] > firstOrd[i+1]){
        count = count + 1;
        index[count] = i;
    }
}
i = 0;
int diff,hi,lo;
//Do some linear interpolation using the peaks in the first order
//spectra
while(index[i+1] != 0){
hi = index[i+1];
lo = index[i];
diff = hi - lo;
for(int j=1; j<diff; j++){
firstOrd[lo+j] = firstOrd[lo]+ double(j)/double(diff)*(firstOrd[hi]
 - firstOrd[lo]);
}
i++;
}
}

/**********************************************************************
  The subroutine interpolate uses linear interpolation to find values
  of the total cross section evenly spaced over the frequency range
  [-2*wB,2*wB].
  Motivation for doing this is given above. An even frequency spacing
  is useful for when calculating the FFT

  Inputs: fOutput - pointer to array of evenly spaced values of the
   total cross section
fFreq - pointer to array of 4001 evenly spaced frequency points
output - original value of the total cross section
wB - Bragg frequencye cross section for that frequency value
```

```
  Modifies: fFreq, fOutput

  Pre: None
  Post: puts evenly spaced frequency values in fFreq and interpolates the array
to fill fOutput

*****************************************************************/
void interpolate(double* fOutput, const double* freq,
const double* output, const double wB){

int ind0 = 0;
fOutput[0] = output[0];
int ind1 = 0; //arbitrarily set;
//number of points in fFreq between freq[i] and freq[i+1],exclusively
int diff = 0;
int j = 0;
//double temp;
double tempFreq[numFinalFreq];
//Set up the frequency array
for(int i=0; i<numFinalFreq; i++){
tempFreq[i] = (-2 + 0.002*i) *wB;
}
//This is a generic linear interpolation algorithm
for(i=0; i<freqPoints-1; i++){
while(tempFreq[ind1] <= freq[i+1] &&ind1<numFinalFreq){
ind1++;
}
fOutput[ind1] = output[i+1];
fOutput[ind0] = output[i];
diff = ind1 -ind0 -1;
for(j = 1; j<=diff; j++){
fOutput[ind0+j] = output[i] + double(j)/double(diff+1) *
(output[i+1] - output[i]);
}
ind0 = ind1;
}
}

/*****************************************************************
  The subroutine noise creates a 'realistic' version of the total
  cross section.
  The word 'realistic' indicates that the cross section will be based
  on a finite time series and that noise will be added.
```

```
  Inputs: k0 - radar wavenumber
deltaPs - lenght of surface patch
fFreq - pointer to array of 4001 evenly spaced frequency points
fOutput - pointer to array of evenly spaced values of the total
cross section
rho - distance from radar to patch
wDop1 - current induced Doppler shift due to radar, in rad/s
F - spherical earth attenuation for radar
Fa - external noise figure at frequency of interest

  Modifies: fFreq, fOutput

  Pre: None
  Post: Creates a noisy version of the total cross section based on a finite
time series

*****************************************************************/
void noise(double k0, int deltaPs, double* fFreq, double* fOutput,
double rho, double wDop1, double F, int Fa){

/* Stages to follow:
1. Find the power spectral density P_c(w). It is a function of the
cross section, patch area and distance, antenna gains, and attenuation
functions etc
2. Somehow find the NSD (noise spectral density)
3. Find the time series of the clutter and noise PSDs
(This is the hard part)
4. Add the results of 2. and 3. to find the total time series
(noise + clutter); write to file
5. Do an FFT on the total time series to find the noisy spectra
- done in Matlab
*/
//Before starting the stages initialize the variables needed
double c = 3e8; //speed of light in air
double lambda0 = 2*pi/k0; //wavelength of the radar wave
double tau0 = 2*deltaPs/c; //"on" length of a pulse
//total length of a pulse, try to keep 4% duty cycle
double Tl = 25*tau0;
//duty cycle for the Tx; Gill 1999 suggests 4% duty cycle
double d = tau0/Tl;
//total peak transmitter power - arbitrary, Cape Race is 16kW?
double Pt = 16e3;
```

```
//gain of the transmitting antenna - arbitrary, Cape Race is 1.585?
double Gt = 1.585;
double Gr = 65.76; //gain of the Rx antenna - see Gill,1999 pg. 197,
//The beamwidth of the radar is 4 degrees or 4*pi/180 radians
double beamWidth = 4*pi/180.;
double Ts = .25;       //Sampling interval
const int lenTime = 4096;

//area of the patch, in cylindrical A = rho*d_rho*d_phi
double A1 = deltaPs*rho*beamWidth;

//clutter power spectral density for the patch
double Pc1[numFinalFreq] = {0.};

double reCt1 = 0.; //real part of the clutter time signal
double imCt1 = 0.; //imag part of the clutter time signal
double reNt1 = 0.; //real part of the noise time signal
double imNt1 = 0.; //imag part of the noise time signal

double P_N = 0; //noise PSD what's the difference?
double Sn = 0; //PSD of the noise

//Step 1: Find the PSD of the clutter
for(int i=0; i<numFinalFreq; i++){
Pc1[i] = fOutput[i]*pow(lambda0,2) *d*Pt*Gt*Gr* pow(fabs(F),4)
 *A1/(pow(4*pi,3)*pow(rho,4));
}

//Step 2: Find the PSD of the noise -> Note the PSD for the noise
//will be the same for each radar since it does not depend on the
//distance or angle, just the noise figure and temp.

//Assume sampling at pulse centres
//We can assume S_n(w') is flat (Gill, pg. 176); the BW for the
//system is 2*pi/tau0 see Barton and (Gill, 1999 pg.176)
//w is for Doppler frequencies and w' has to do with radar bandwidth
//Assume a matched filter system -> Bn = 1/tau0 i.e. noise bandwidth
// = 1/(pulse width)

//Sn = k*T_0/(2*pi)*10^(F_am/10) F_am = 22, 36, 42dB for
//freq = 25, 10, 5.75MHz respectively
Sn = 1.38e-23*290/(2*pi)*pow(10,Fa/10);
```

```
//Now calculate summation Gill, 1999 equation 4.61 ->case for finite
//# pulses similar to infinite # pulses
for(i=int(ceil(-.5/d)); i<=-1; i++){
    P_N = P_N + sin(i*pi*d)/(i*pi*d);
}
P_N = P_N + 1;
for(i=1; i<=int(floor(.5/d)); i++){
P_N = P_N + sin(i*pi*d)/(i*pi*d);
}
P_N = P_N*Sn*d;  //include multipliers taken outside integral


//Step 3: Find the time series for the clutter and the noise
int p = int(floor(numFinalFreq-2)/2);
double t; //actual values of time
//real and imag. parts of the complex exponential
double reC, imC, cRoot;
//and the (real) value of the squre root for clutter time series
double reN, imN, nRoot;

//Frequency net as suggested by Pierson - use every second frequency
//value For some reason this produces an even flatter noise signal
//than looking at every frequency value - only .5dB difference
//between maxima and minima for 8192 time points

ofstream timeFile;
timeFile.open("time.xls");
double delF = fFreq[3] - fFreq[1];

double ran;
for(int D=0; D<lenTime; D++){
t = D*Ts;
reCt1 = 0.;
imCt1 = 0.;
reNt1 = 0.;
imNt1 = 0.;

for(int E=0; E<=p; E++){

ran = rand()/RAND_MAX*2*pi;
reC = cos((fFreq[2*E+1]+wDop1)*t + ran);
imC = sin((fFreq[2*E+1]+wDop1)*t + ran);
```

```
ran = rand()/RAND_MAX*2*pi;
reN = cos((fFreq[2*E+1]+wDop1) *t + ran);
imN = sin((fFreq[2*E+1]+wDop1)*t + ran);

cRoot = sqrt(Pc1[2*E+1]*delF);
nRoot = sqrt(P_N*delF);
reCt1 = reCt1 + reC*cRoot;
imCt1 = imCt1 + imC*cRoot;
reNt1 = reNt1 + reN*nRoot;
imNt1 = imNt1 + imN*nRoot;

}
//Step 4: Combine clutter and time signals and write them to a file
timeFile << reCt1 +reNt1 << '\t' << imCt1 +imNt1 << '\n';

}

//Step 5 - not done here. Take the timeFile ("time.xls") and process
//it in Matlab
timeFile.close();

}
/*********************************************************************
  The routine findDop() just finds the Doppler shift for the given
  radar configuration.

  Inputs: Vx,Vy - current velocity
x,y - location of range cell wrt radar site
k0 - radar wavenumber
Dop - value of the Doppler shift (Hz)

  Modifies: Dop

  Pre: none
  Post: The value of the Doppler shift is found and stored in Dop

*********************************************************************/
void findDop(double Vx, double Vy, double x, double y, double k0,
double & Dop){

double V1; //radial velocity as seen by radar
double ang; //radar look direction
```

```
ang = atan2(y,x);
V1 = Vx*cos(ang) + Vy*sin(ang);
Dop = V1/sqrt(g/(2*k0)); //This is in Hz
}
```